E-ISSN: 2147-1959

MIRT

Molecular Imaging and Radionuclide Therapy

February 2026 Volume 35 Issue 1 www.tsnm.org

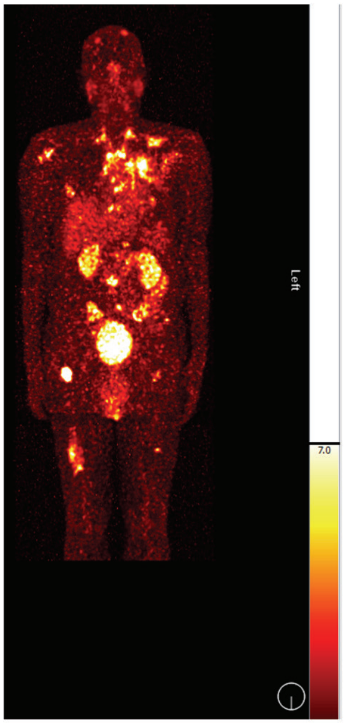

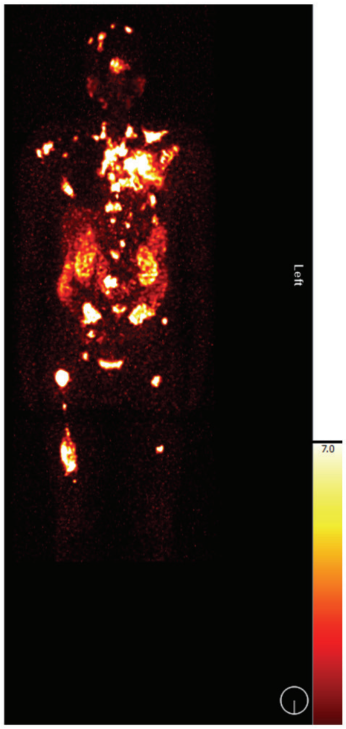

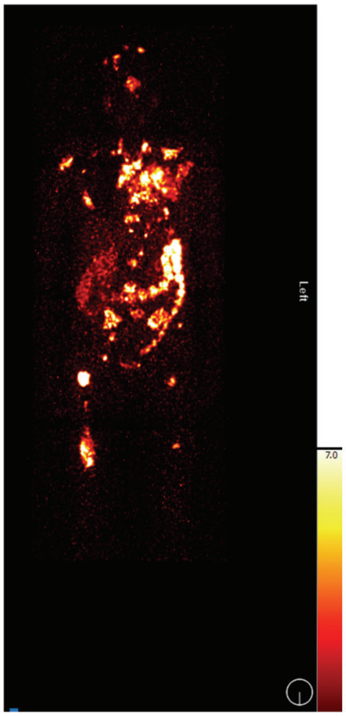

"Official Journal of the Turkish Society of Nuclear Medicine"

galenos yayınevi

MIRT

Molecular Imaging and Radionuclide Therapy

- **The Ownership: Turkish Society of Nuclear Medicine (TSNM)**
  Turkish Society of Nuclear Medicine
  Address: Aziziye Mah. Pilot Sk. 10/12,
  Çankaya/Ankara, Türkiye
  e-mail: dernekmerkezi@tsnm.org ·
  Tel: +90 312 441 00 45

- **Publishing Manager**
  Prof. Elif Özdemir, MD.
  Ankara Yıldırım Beyazıt University Faculty of Medicine, Department of Nuclear Medicine; Ankara Bilkent City Hospital, Clinic of Nuclear Medicine, Ankara, Türkiye
  E-mail: ozdemire80@gmail.com
  ORCID ID: 0000-0002-9142-8752

- **Editor in Chief**
  Prof. Murat Fani Bozkurt, MD, FEBNM
  FEBNM Hacettepe University, Medical School, Department of Nuclear Medicine, Ankara, Türkiye
  E-mail: fanibozkurt@gmail.com
  ORCID ID: 0000-0003-2016-2624

- **Associate Editors**
  Prof. Nalan Selçuk, MD.
  Yeditepe University, Medical School, Department of Nuclear Medicine, İstanbul, Türkiye
  E-mail: nalanselcuk@yeditepe.edu.tr
  ORCID ID: 0000-0002-3738-6491

  Prof. Çiğdem Soydal, MD.
  FEBNM, Ankara University Medical School, Department of Nuclear Medicine, Ankara, Türkiye
  Email: csoydal@yahoo.com; csoydal@ankara.edu.tr
  ORCID ID: 0000-0002-6199-8551

- **Statistics Editors**
  Prof. Gül Ergör, MD.
  Dokuz Eylül University, Medical School, Department of Public Health, İzmir, Türkiye
  E-mail:gulergor@deu.edu.tr

  Prof. Sadettin Kılıçkap, MD.
  Hacettepe University, Medical School, Department of Preventive Oncology, Ankara, Türkiye
  E-mail: skilickap@yahoo.com

- **English Language Editor**
  Galenos Publishing House

Scientific Advisory Board

Ayşegül Akgün
Ege University, Medical School, Department of Nuclear Medicine, İzmir, Türkiye
Esma Akın
The George Washington University, Medical School, Department of Diagnostic Radiology, Wahington DC, USA
Akram Al-Ibraheem
King Hussein Cancer Center (KHCC), Department of Nuclear Medicine, Amman, Jordan
Claudine Als
Hopitaux Robert Schuman Zitha Klinik, Médecine Nucléaire, Luxembourg
Corinna Altini
Nuclear Medicine Unit, AOU Policlinic of Bari – University of Bari "Aldo Moro", Bari, Italy
Vera Artiko
Clinical Center of Serbia, Center for Nuclear Medicine, Belgrade, Serbia
Nuri Arslan
University of Health Sciences Türkiye, Gülhane Medical School, Gülhane Training and Research Hospital, Clinic of Nuclear Medicine, Ankara, Türkiye
Lütfiye Özlem Atay
Gazi University Faculty of Medicine, Department of Nuclear Medicine, Ankara, Türkiye
Marika Bajc
Lund University Hospital, Clinic of Clinical Physiology, Lund, Sweden
Lorenzo Biassoni
Great Ormond Street Hospital for Children NHS Foundation Trust, Department of Radiology, London, United Kingdom
Hans Jürgen Biersack
University of Bonn, Department of Nuclear Medicine, Clinic of Radiology, Bonn, Germany
M. Donald Blaufox
Albert Einstein College of Medicine, Department of Radiology, Division of Nuclear Medicine, New York, USA.
Patrick Bourguet
Centre Eugène Marquis Department of Nuclear Medicine, Clinic of Radiology, Rennes, France
Murat Fani Bozkurt
FEBNM Hacettepe University, Medical School, Department of Nuclear Medicine, Ankara, Türkiye
A. Cahid Civelek
NIH Clinical Center, Division of Nuclear Medicine, Bethesta, USA
Arturo Chiti
Humanitas University, Department of Biomedical Sciences; Humanitas Clinical and Research Center, Clinic of Nuclear Medicine, Milan, Italy
Josep Martin Comin
Hospital Universitari de Bellvitge, Department of Nuclear Medicine, Barcelona, Spain
Alberto Cuocolo
University of Naples Federico II, Department of Advanced Biomedical Sciences, Napoli, Italy
Tevfik Fikret Çermik
University of Health Sciences Türkiye, İstanbul Training and Research Hospital, Clinic of Nuclear Medicine, İstanbul, Türkiye
Angelika Bischof Delaloye
University Hospital of Lausanne, Department of Radiology, Lausanne, Switzerland
Mustafa Demir
İstanbul University, Cerrahpaşa Medical School, Department of Nuclear Medicine, İstanbul, Türkiye
Hakan Demir
Kocaeli University Medical School, Department of Nuclear Medicine, Kocaeli, Türkiye
Peter Josef Ell
University College Hospital, Institute of Nuclear Medicine, London, United Kingdom
Tanju Yusuf Erdil
Marmara University, Pendik Training and Research Hospital, Clinic of Nuclear Medicine, İstanbul, Türkiye
Türkan Ertay
Dokuz Eylül University, Medical School, Department of Nuclear Medicine, İzmir, Türkiye
Jure Fettich
University Medical Centre Ljubljana, Department for Nuclear Medicine, Ljubljana, Slovenia

MIRT

Molecular Imaging and Radionuclide Therapy

Christiane Franzius
Klinikum Bremen Mitte Center, Center for Modern Diagnostics, Bremen, Germany
Lars Friberg
University of Copenhagen Bispebjerg Hospital, Department of Nuclear Medicine, Copenhagen, Denmark
Jørgen Frøkiær
Aarhus University Hospital, Clinic of Nuclear Medicine and PET, Aarhus, Denmark
Maria Lyra Georgosopoulou
University of Athens, 1st Department of Radiology, Aretaieion Hospital, Radiation Physics Unit, Athens, Greece
Gevorg Gevorgyan
The National Academy of Sciences of Armenia, H. Buniatian Institute of Biochemistry, Yerevan, Armenia
Seza Güleç
Florida International University Herbert Wertheim College of Medicine, Departments of Surgery and Nuclear Medicine, Miami, USA
Liselotte Højgaard
University of Copenhagen, Department of Clinical Physiology, Nuclear Medicine and PET, Rigshospitalet, Copenhagen, Denmark
Ora Israel
Tel Aviv University Sackler Medical School, Assaf Harofeh Medical Center, Clinic of Otolaryngology-Head and Neck Surgery, Haifa, Israel
Csaba Juhasz
Wayne State University Medical School, Children's Hospital of Michigan, PET Center and Translational Imaging Laboratory, Detroit, USA
Gamze Çapa Kaya
Dokuz Eylül University, Medical School, Department of Nuclear Medicine, İzmir, Türkiye
Metin Kır
Ankara University, Medical School, Department of Nuclear Medicine, Ankara, Türkiye
Irena Dimitrova Kostadinova
Alexandrovska University Hospital, Clinic of Nuclear Medicine, Sofia, Bulgaria
Lale Kostakoğlu
The Mount Sinai Hospital, Clinic of Nuclear Medicine, New York, USA
Rakesh Kumar
All India Institute of Medical Sciences, Department of Nuclear Medicine, New Delhi, India
Georgios S. Limouris
Athens University, Medical School, Department of Nuclear Medicine, Athens, Greece
Luigi Mansi
Second University of Naples, Medical School, Department of Nuclear Medicine, Naples, Italy
Yusuf Menda
University of Iowa Health Care, Carver College of Medicine, Department of Radiology, Iowa City, USA
Vladimir Obradović
University of Belgrade, Faculty of Organizational Sciences, Department of Human Development Theory, Business Administration, Organizational Studies, Belgrade, Serbia
Zehra Özcan
Ege University Faculty of Medicine, Department of Nuclear Medicine, İzmir, Türkiye
Yekta Özer
Hacettepe University, Faculty of Pharmacy, Department of Radiopharmaceutical, Ankara, Türkiye
Francesca Pons
Hospital Clinic, Clinic of Nuclear Medicine, Barcelona, Spain
Monica Rossleigh
Sydney Children's Hospital, Clinic of Nuclear Medicine, Sydney, Australia
Dragana Sobic Saranovic
University of Belgrade, Medical School, Departments of Radiology, Oncology and Cardiology, Belgrade, Serbia
Mike Sathekge
University of Pretoria, Steve Biko Academic Hospital, Department of Nuclear Medicine, Pretoria, South Africa
Kerim Sönmezoğlu
İstanbul University, Cerrahpaşa Medical School, Department of Nuclear Medicine, İstanbul, Türkiye
Zsolt Szabo
The Johns Hopkins Hospital, Divisions of Radiology and Radiological Science, Baltimore, USA
Istvan Szilvasi
Semmelweis University, Medical School, Department of Nuclear Medicine, Budapest, Hungary
Berna Okudan Tekin
Ankara Numune Trainig and Research Hospital, Clinic of Nuclear Medicine, Ankara, Türkiye
Mathew L. Thakur
Thomas Jefferson University, Department of Radiology, Pennsylvania, USA
Bülent Turgut
Cumhuriyet University, Medical School, Department of Nuclear Medicine, Sivas, Türkiye
Turgut Turoğlu
Marmara University, Medical School, Department of Nuclear Medicine, İstanbul, Türkiye
Gülin Uçmak
University of Health Sciences Türkiye, Ankara Oncology Training and Research Hospital, Clinic of Nuclear Medicine, Ankara,Türkiye
Doğangün Yüksel
Pamukkale University, Medical School, Department of Nuclear Medicine, Denizli, Türkiye

Turkish Society of Nuclear Medicine
Cinnah Caddesi Pilot Sokak No: 10/12 Çankaya 06650 Ankara, Türkiye **Phone:** +90 312 441 00 45 **Fax:** +90 312 441 12 95 **Web:** www.tsnm.org **E-mail:** dernekmerkezi@tsnm.org
"Formerly Turkish Journal of Nuclear Medicine"

Reviewing the articles' conformity to the publishing standards of the Journal, typesetting, reviewing and editing the manuscripts and abstracts in English, creating links to source data, and publishing process are realized by Galenos.

Publisher Contact
Address: Molla Gürani Mah. Kaçamak Sk. No: 21/1 34093 İstanbul, Türkiye
Phone: +90 (530) 177 30 97 / +90 (539) 307 32 03
E-mail: info@galenos.com.tr/yayin@galenos.com.tr
Web: www.galenos.com.tr
Publisher Certificate Number: 14521

Online Publication Date: February 2026
ISSN: 2146-1414 **E-ISSN:** 2147-1959

International scientific journal published quarterly.

MIRT

Molecular Imaging and Radionuclide Therapy

Please refer to the journal's webpage **(https://mirt.tsnmjournals.org/)** for "Aims and Scope", "Instructions to Authors" and "Ethical Policy".

The editorial and publication process of Molecular Imaging and Radionuclide Therapy are shaped in accordance with the guidelines of ICMJE, WAME, CSE, COPE, EASE, and NISO. The journal is in conformity with the Principles of Transparency and Best Practice in Scholarly Publishing.

Molecular Imaging and Radionuclide Therapy is indexed in **Pubmed, Pubmed Central (PMC), Emerging Sources Citation Index (ESCI), TUBITAK-ULAKBIM, Scopus, Gale/Cengage Learning, EBSCO databases, ProQuest Health** & **Medical Complete, CINAHL, Embase, J-Gate, IdealOnline, Türkiye Atıf Dizini-Turkiye Citation Index, Turk Medline, Hinari, GOALI, ARDI, OARE, AGORA** and **CNKI**.

The journal is published electronically.

Owner: Turkish Society of Nuclear Medicine

Responsible Manager: Murat Fani Bozkurt

MIRT

Molecular Imaging and Radionuclide Therapy

CONTENTS

Original Articles

Interesting Images

TURKISH SOCIETY OF NUCLEAR MEDICINE
1975

MIRT
Molecular Imaging and Radionuclide Therapy

CONTENTS

Case Reports

Original Article

Mol Imaging Radionucl Ther 2026;35(1):1-9 ***DOI:****10.4274/mirt.galenos.2025.90692*

Effects of High-dose Radioactive Iodine Therapy on Hormonal Profiles and Sperm Quality in Thyroidectomy Patients

Tiroidektomi Hastalarında Yüksek Doz Radyoaktif İyot Tedavisinin Hormonal Profiller ve Sperm Kalitesi Üzerine Etkileri

Mehrosadat Alavi[1,2], Raziyeh Hojjat[3], Ali Taghinezhad[4], Manzarbanoo Shojaeifard[5]

[1]*Ionizing and Non-Ionizing Radiation Protection Research Center (INIRPRC), School of Paramedical Sciences, Shiraz University of Medical Sciences, Shiraz, Iran*
[2]*Department of Nuclear Medicine, Shiraz University of Medical Sciences, Fasa, Iran*
[3]*Student Research Committee, Fasa University of Medical Sciences, Fasa, Iran*
[4]*Department of English Language, Fasa University of Medical Sciences, Fasa, Iran*
[5]*Department of Physiology, Fasa University of Medical Sciences, Fasa, Iran*

Abstract

Objectives: This study investigates the effects of high-dose radioactive iodine therapy on gonadotropin and sex hormone levels, and on sperm parameters in male patients with differentiated thyroid carcinoma following thyroidectomy.

Methods: Twenty-five male patients (aged 20-60 years) with differentiated thyroid carcinoma underwent thyroidectomy and iodine therapy. The therapeutic dose was 150 mCi of oral sodium iodide solution. Levels of gonadotropins, sex hormones, and anti-Müllerian hormone (AMH) were measured before and two weeks after radioiodine therapy (RT). Semen analysis included liquefaction, odor, color, viscosity, agglutination, and aggregation. The main parameters evaluated were semen volume, pH, sperm count, percentages of motile and progressively motile sperm, round cells, and sperm morphology. Sperm motility, including progressive, non-progressive, and immotile types, and DNA fragmentation were analyzed according to World Health Organization guidelines.

Results: The Wilcoxon signed-rank test was used with a significance level of $p \leq 0.05$. Follicle-stimulating hormone levels in patients' sera were significantly higher than pre-RIT measurements ($p=0.002$), whereas luteinizing hormone, dihydrotestosterone, dehydroepiandrosterone sulfate, testosterone, and AMH levels were not significantly different from pre-RT measurements. Total sperm count, volume, motility, and rapid progressive motility increased significantly compared to pre-radioiodine ablation measurements, while other parameters remained unchanged.

Conclusion: Male patients who received 150 mCi of radioactive iodine showed no impairment in fertility. Long-term follow-up studies with larger sample sizes are crucial to investigate the physiological roles of gonadal hormones, sperm DNA fragmentation, and AMH in the testes after RIT.

Keywords: Radioiodine therapy, sperm DNA fragmentation, thyroid

---

Address for Correspondence: Manzarbanoo Shojaeifard, Department of Physiology, Fasa University of Medical Sciences, Fasa, Iran
E-mail: shojaeim@sums.ac.ir **ORCID ID:** orcid.org/0000-0001-7118-4298

Received: 31.03.2025 **Accepted:** 28.09.2025 **Publication Date:** 03.02.2026

Cite this article as: Alavi M, Hojjat R, Taghinezhad A, Shojaeifard M. Effects of high-dose radioactive iodine therapy on hormonal profiles and sperm quality in thyroidectomy patients. Mol Imaging Radionucl Ther. 2026;35(1):1-9.

Öz

Amaç: Bu çalışma, diferansiye tiroid karsinomlu erkek hastalarda tiroidektomi sonrası yüksek doz radyoaktif iyot tedavisinin gonadotropin, seks hormonu seviyeleri ve sperm parametrelerini nasıl etkilediğini araştırmaktadır.

Yöntem: Diferansiye tiroid karsinomlu yirmi beş erkek hastaya (20-60 yaş arası) tiroidektomi ve iyot tedavisi uygulandı. Terapötik doz 150 mCi sodyum iyodür oral solüsyonuydu. Gonadotropin, seks hormonu ve anti-Müllerian hormon (AMH) seviyeleri, radyoiyot tedavisinden (RT) önce ve iki hafta sonra ölçüldü. Semen analizi sıvılaşma, koku, renk, viskozite, aglütinasyon ve agregasyonu içeriyordu. Değerlendirilen başlıca parametreler semen hacmi, pH, sperm sayısı, hareketli ve progresif hareketli sperm yüzdeleri, yuvarlak hücreler ve morfolojiydi. Progresif, non-progresif ve immotil tipler dahil olmak üzere sperm motilitesi ve DNA parçalanması, Dünya Sağlık Örgütü kılavuzlarına göre analiz edildi.

Bulgular: Wilcoxon işaretli sıralamalar testi, p≤0,05 anlamlılık eşiği ile kullanıldı. Hastaların serumlarındaki folikül uyarıcı hormon seviyeleri, RIT öncesi ölçümlere göre anlamlı derecede yüksek bulundu (p=0,002), ancak luteinize edici hormon, dihidrotestosteron, dehidroepiandrosteron sülfat, testosteron ve AMH seviyelerinde anlamlı bir fark görülmedi. Toplam sperm sayısı, hacmi, motilitesi ve hızlı progresif motilite, radyoiyot ablasyonu öncesi ölçümlere kıyasla anlamlı şekilde artarken, diğer parametreler değişmeden kaldı.

Sonuç: Yüz elli mCi radyoaktif iyot alan erkek hastalarda infertilitede herhangi bir bozulma görülmedi. RIT sonrası gonadal hormonların, sperm DNA parçalanmasının ve testislerdeki AMH'nin fizyolojik rollerini araştırmak için daha geniş bir örneklem büyüklüğüyle uzun süreli takip çok önemlidir.

Anahtar kelimeler: Radyoaktif iyot tedavisi, sperm DNA parçalanması, tiroid

Introduction

Recently, thyroid cancer has become a common malignancy of the endocrine system, with a threefold higher incidence in females than in males (1). Papillary thyroid carcinoma (PTC) is the most prevalent subtype of differentiated thyroid carcinoma (DTC), accounting for 80% of thyroid cancers. Follicular thyroid carcinoma accounts for a smaller proportion of DTCs (2). PTC usually presents as a thyroid nodule. Treatment for PTC includes surgery (involving the complete removal of the thyroid gland) and radioactive iodine (RAI) therapy (often given after surgery). It is routinely recommended when DTC exceeds 4 cm, demonstrates extrathyroidal or extranodal extension, or presents with distant metastasis (3).

RAI therapy aims to obliterate residual thyroid tissue and any lingering cancer cells remaining after surgery. Additionally, RAI therapy may be employed in cases where DTC has metastasized to distant sites, and thyroid hormone replacement is required after surgery because cessation of endogenous thyroid hormone production necessitates lifelong replacement therapy. These hormones play a crucial role in regulating metabolic processes, growth, and development. Consequently, individuals undergoing thyroidectomy are mandated to receive thyroid hormone replacement therapy lifelong, with careful follow-up to monitor for recurrence (4).

RAI can cause direct damage to gonadal tissues, especially affecting the testes in males and the ovaries in females. This damage may lead to reduced hormone production, impaired spermatogenesis, and dysfunction of oocytes (5). RAI-induced sexual dysfunction in men most commonly presents as erectile dysfunction (ED), which is characterized by the inability to achieve or maintain an erection sufficient for sexual activity. Studies report a significant increase in ED rates after RAI therapy, with up to 50% of men affected. This treatment adversely affects the patient's quality of life (6). In male patients with DTC, testosterone (T) levels are lower, sperm quality is poorer, and follicle-stimulating hormone (FSH) and luteinizing hormone (LH) levels are higher (7,8). Additionally, other studies have found that transient male infertility is dose-dependent (9,10). As a result, permanent infertility is linked to receiving high or cumulative doses of RAI administered because of metastasis.

RAI therapy using iodine-131 (I-131) effectively destroys thyroid cancer cells by emitting beta particles. This process can be detected through gamma radiation scanning (11).

The primary gap identified is the lack of detailed information regarding the impact of RAI therapy on male fertility following DTC treatment. There is a need for comprehensive findings from relevant studies, a deeper exploration of the effects on reproductive hormones, and insights into personalized approaches to managing DTC. The objective of this study is to assess hormonal alterations and sperm DNA fragmentation following administration of high-dose RAI in individuals with thyroid cancer.

Materials and Methods

In this study, we identified 25 male patients (20-60 years) who were referred to the clinic for DTC, underwent thyroidectomy, and were selected for iodine therapy. This study excluded patients referred for problems related to environmental pollution, varicocele, excessive heat exposure, infections, non-thyroid cancers, and dietary and lifestyle factors. Those with benign thyroid disease were also excluded. Organic disorders of the reproductive organs, including varicocele, abnormal testicular position, testicular torsion, and a history of severe genital trauma, were excluded. A limitation of this study is that the sample size is small due to time and cost constraints.

The goal of RAI therapy is to destroy both remaining thyroid cells and cancer cells after surgery. Based on thyroid radionuclide results, the therapeutic dose was 150 mCi of oral sodium iodide solution. The RAI dose is typically selected based on an assessment of tumor recurrence risk and other factors (12), as there is no definitive agreement on the optimal dose (13).

Consequently, 10-mL blood samples were collected from all patients undergoing thyroidectomy to assess the levels of gonadotropins and sex hormones. Serum concentrations of FSH, LH, dihydrotestosterone (DHT), dehydroepiandrosterone (DHEA), T, and anti-Müllerian hormone (AMH) were measured using immunoassay techniques, specifically by ELISA (enzyme-linked immunosorbent assay) or chemiluminescence (CL), both before and at two weeks after radioiodine therapy. Semen samples were collected from patients twice—once before iodine treatment and again two weeks after treatment—to evaluate semen parameters and sperm DNA fragmentation. We asked the patients to abstain from sexual intercourse for 3-5 days prior to semen collection. Each participant was asked to complete a comprehensive health questionnaire covering age, weight, height, reproductive characteristics, pregnancies and outcomes, medical history, intoxications, and medication use. Additionally, all patients provided their signed informed consent before undergoing surgery and iodine treatment.

Semen analysis was conducted in accordance with the additional guidelines outlined by Björndahl et al. (14) the observational evaluation stage for semen parameters is classified as A-. This evaluation encompasses several elements, including volume (the total count of spermatozoa and non-sperm cells present in the ejaculate, which must be calculated) and concentration, often referred to as sperm count. Number of sperm count x dilution factor/ volume x 1000 = sperm/mL. Stickiness: Semen is typically a semisolid, coagulated mass. At room temperature, semen usually begins to liquefy within a few minutes to approximately 15 minutes, becoming thinner and changing color. A standard liquefied semen sample has a homogeneous, grey-opalescent appearance (15).

Semen analysis should begin with a basic inspection shortly after liquefaction, ideally within 30 minutes but no later than 1 hour post-ejaculation. The microscopic evaluation of semen parameters involves examining sperm shape, motility, and count using light microscopy on slides. A comprehensive analysis includes assessment of motility (total and progressive), morphology (sperm shape), and concentration. Determining sperm concentration, along with evaluating motility and morphology, is essential for assessing fertility (16). The next step involves molecular evaluation of semen parameters to assess DNA integrity. This includes using the halo sperm method with the sperm chromatin structure assay (SCSA) kit to analyze sperm DNA. SCSA is a flow cytometric test that detects high levels of DNA fragmentation in sperm samples, a condition characterized by small breaks in DNA. Sperm DNA breaks are assessed indirectly by measuring DNA denaturability. SCSA is the most extensively studied method for determining DNA integrity. In this assay, sperm are exposed to a dye that highlights damaged DNA. The assay measures the susceptibility of sperm DNA to acid-induced denaturation *in situ*, followed by staining with the fluorescent dye acridine orange (17,18).

These observations were used to calculate the DNA fragmentation index (DFI), with a DFI of less than 25% was considered within the normal range. Normal sperm DNA exhibited radiating halos, whereas damaged sperm DNA exhibited either no halos or only minor halos. Fragmented sperm were defined as those having a small or absent halo (19). The DFI was calculated using the following formula:

DFI (%) =100× (number of spermatozoa with fragmented DNA/total number of spermatozoa) (20).

Sperm DNA fragmentation was measured using the SDFA kit (DNA Fragmentation Assay Kit; Ideh Varzan Farda, Tehran, Iran). This kit facilitates the detection of DNA fragmentation through a halo assay, where stained sperm are examined under bright-field microscopy. Following the manufacturer's protocol, sperm samples were processed, stained, and observed. The extent of DNA fragmentation was determined by assessing the halo size and contrast, with larger halos indicating intact DNA and smaller or absent halos indicating fragmentation.

Ethical clearance for this research was obtained from the Fasa University of Medical Sciences Ethics Committee on May 22, 2022, and the study was conducted in accordance with the approved protocol. This committee reviewed and endorsed the study's ethical considerations (ethical code: REC.1401.020, date: 11.05.2025).

Statistical Analysis

The data were analyzed using SPSS version 23, presenting the results as the median, 25th percentile (P25), and 75th percentile. The Wilcoxon signed-rank test, a non-parametric test, was used when the assumptions of the dependent t-test were violated. The significance level was set at $p \leq 0.05$.

Results

Study Population Characteristics

We identified 25 male patients (20-60 years) who were referred to the clinic for DTC, who underwent thyroidectomy, and who were selected for iodine therapy.

Hormonal Assessment Via Immunoassay

The median serum FSH level in patients increased significantly compared with levels before RAI therapy (RIT) ($p=0.002$; $p<0.05$ Wilcoxon test). However, values for LH, DHT, DHEA-SO4 (DHEA sulfate), T, and AMH did not change significantly before and after RIT (Figure 1 and Table 1).

Sperm Analysis

Through detailed microscopic examinations, essential parameters in patients such as semen volume (mL, $p=0.02$), total sperm count (million/ejaculate, $p=0.034$), sperm motility (%), and rapid progressive motility (%), showed significant changes before and after RAI therapy. However, we assessed characteristics such as liquefaction, color, odor, viscosity, agglutination, and aggregation during semen analysis; these assessments revealed no significant differences before and after RIT. Additionally, following World Health Organization (WHO) guidelines, we assessed sperm motility to determine the percentages of progressive, non-progressive, and immotile sperm. No significant changes were observed in these parameters before or after RIT. Furthermore, we evaluated semen pH; sperm count (million/mL); motile sperm (%); slow progressive sperm (%); non-motile sperm (%); round cells (million/mL); and normal and abnormal morphology (%), and found no significant differences before and after RIT (Figure 1a-e and Table 2). Figure 2 presents a semen analysis report generated using the High-Frame-rate Tracking-Computer-Assisted Semen Analysis system, following WHO 2010 (6th) guidelines.

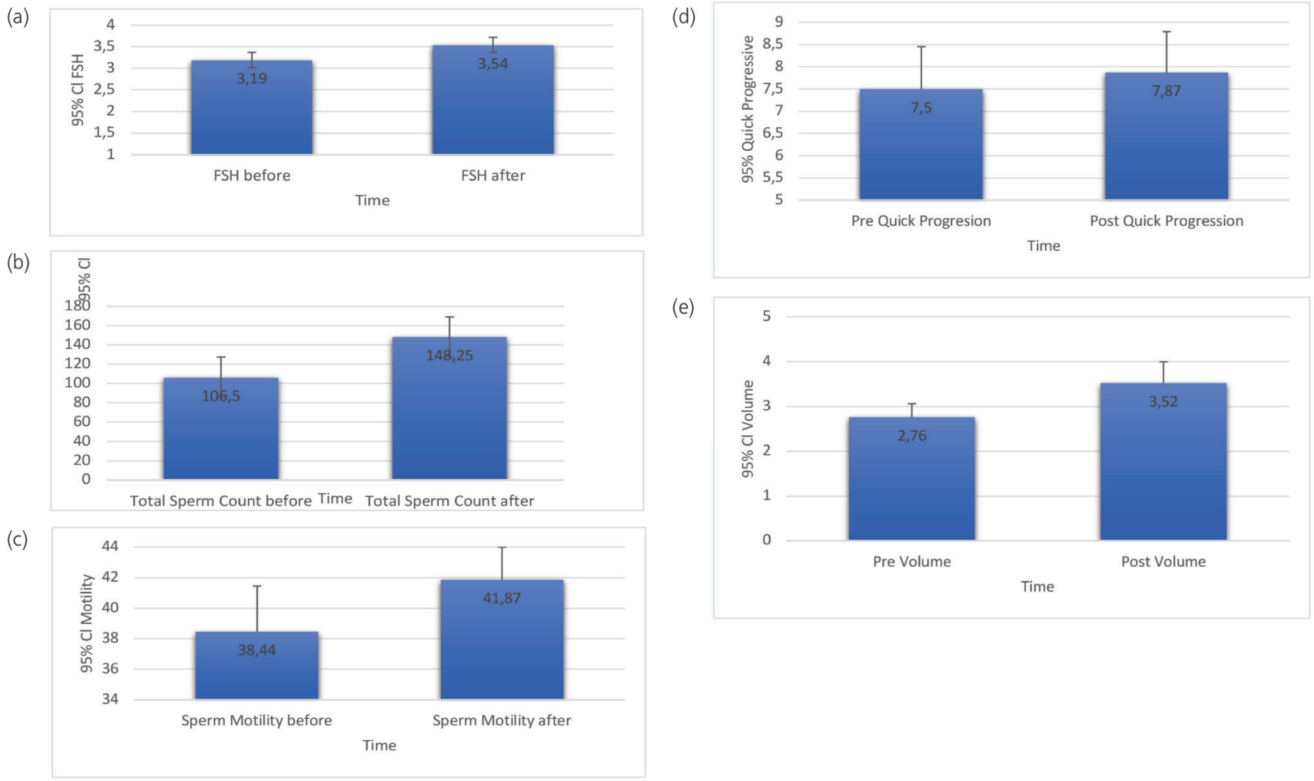

Figure 1. Values of different parameters before and after treatment with radioactive Iodide
(a): FSH values in patients before and after treatment with radioactive iodide (p-value=0.02)
(b): Total sperm count values in patients before and after treatment with radioactive iodide (p-value=0.034)
(c): Sperm motility values in patients before and after treatment with radioactive iodide (p-value=0.017)
(d): Quick progressive motility values in patients before and after treatment with radioactive iodide (p-value=0.031)
(e): Semen volume values in patients before and after treatment with radioactive iodide (p-value=0.020)

FSH: Follicle-stimulating hormone

Sperm DNA Fragmentation

Moreover, other WHO-defined dynamic parameters that use standardized terminology for velocity variables were measured using CASA systems. No significant change in sperm DNA fragmentation was observed before and after RIT (p=0.460; Table 2).

Discussion

In DTC patients, RAI has been widely used for postoperative remnant ablation. RAI causes side effects in DTC patients, particularly in male patients. Spermatogonia and the germ-cell-producing of the testis are the tissues most sensitive to radiation. Therefore, low doses of radiation to the

Table 1. Determining the effect of radioactive iodine on men's sex hormones before and after removing the thyroid gland

Variables	Mean ± SD before intervention	Mean ± SD after intervention	p-value
Follicle stimulating hormone	3.18±0.45	3.54±0.48 mIU/mL	0.02
Luteinizing hormone	3.70±0.40	3.87±0.39 mIU/mL	0.453
Testosterone	14.37±1.49	13.76±1.58	0.17
DHEA-SO4	348.75±46.24	354.93±49.54 mIU/mL	0.660
Dihydrotestosterone	585.41±49.54	598.64±65.51 Pg/mL	0.717
anti-Müllerian hormone	6.93±0.84	6.44±0.62 ng/mL	0.211

SD: Standard deviation

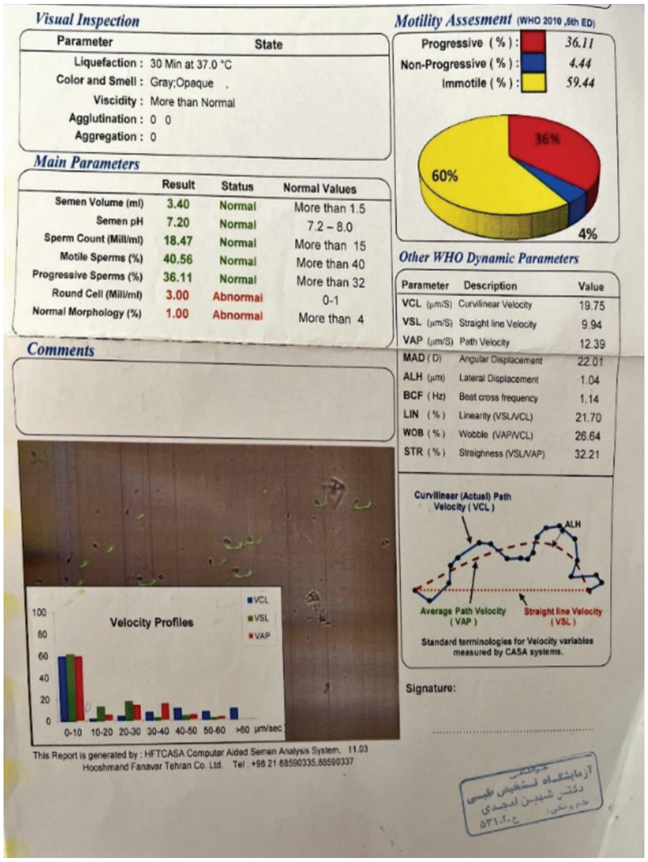

Visual Inspection

Parameter	State
Liquefaction :	30 Min at 37.0 °C
Color and Smell :	Gray;Opaque .
Viscidity :	More than Normal
Agglutination :	0 0
Aggregation :	0

Main Parameters

	Result	Status	Normal Values
Semen Volume (ml)	3.40	Normal	More than 1.5
Semen pH	7.20	Normal	7.2 – 8.0
Sperm Count (Mill/ml)	18.47	Normal	More than 15
Motile Sperms (%)	40.56	Normal	More than 40
Progressive Sperms (%)	36.11	Normal	More than 32
Round Cell (Mill/ml)	3.00	Abnormal	0-1
Normal Morphology (%)	1.00	Abnormal	More than 4

Comments

Motility Assesment (WHO 2010 ,5th ED)

Progressive (%) :	🟥	36.11
Non-Progressive (%) :	🟦	4.44
Immotile (%) :	🟨	59.44

Other WHO Dynamic Parameters

Parameter	Description	Value
VCL (µm/S)	Curvilinear Velocity	19.75
VSL (µm/S)	Straight line Velocity	9.94
VAP (µm/S)	Path Velocity	12.39
MAD (D)	Angular Displacement	22.01
ALH (µm)	Lateral Displacement	1.04
BCF (Hz)	Beat cross frequency	1.14
LIN (%)	Linearity (VSL/VCL)	21.70
WOB (%)	Wobble (VAP/VCL)	26.64
STR (%)	Straighness (VSL/VAP)	32.21

Signature:

This Report is generated by : HFTCASA Computer Aided Semen Analysis System. 11.03
Hooshmand Fanavar Tehran Co. Ltd. Tel : +98 21 88590335,88590337

آزمایشگاه تشخیص طبی
دکتر شهین امجدی

Figure 2. Semen analysis results including motility and velocity profiles [World Health Organization (WHO) 2010, 6th Ed.]. The report includes visual inspection parameters (liquefaction, color, viscosity, agglutination), main semen parameters (volume, pH, sperm count, motility, morphology), motility assessment results (progressive: 36.11%, non-progressive: 4.44%, immotile: 59.44%), and other WHO dynamic parameters (e.g., curvilinear velocity, straight-line velocity, average path velocity). Velocity profiles illustrate the distribution of sperm velocities, using standard terminology for velocity variables measured by CASA systems. Data were analyzed as part of a fertility evaluation study

Table 2. Determining the effect of radioactive iodine on microscopic observations of sperm analysis before and after removing the thyroid gland

Variables	Mean ± SD before intervention	Mean ± SD after intervention	Unit	p-value
Volume	2.76±0.30	3.52±0.48	mL	0.02
Liquefaction	28.12±1.20	28.12±1.43	min	0.914
Sperm count	41.31±7.52	44.12±5.98	Million/mL	0.98
Total sperm count	106.50±20.09	148.25±28.11	Million/ejaculate	0.034
Motility	38.43±3.01	41.84±2.13	%	0.017
Quick progressive motility	7.50±0.94	7.87±0.92	%	0.031
Slow progressive motility	26.62±2.60	29.87±1.90	%	0.48
Non-progressive motility	4.25±0.77	4.06±0.80	%	0.97
Non-motile	61.56±3.01	56.88±2.41	%	0.079
Normal morphology	4.25±0.78	4.81±0.67	%	0.111
Abnormal morphology	95.75±0.78	95.18±0.67	%	0.111
Count	20.98±3.62	24.31±3.54	Million/mL	0.285
Sperm DNA fragmentation	19.90±1.33	21.43±2.00	%	0.460

SD: Standard deviation

gonads can seriously disrupt their function (21,22). Our research revealed elevated serum FSH levels in a sample of 25 men aged 20-60 years. This outcome aligns with similar observations reported in other studies (23,24). Gonadotropins typically exert a direct influence on sex hormones and on the production of sperm and ova (25). The effects of gonadotropins on testicular cells delineate the precise pathways governing T synthesis, spermatogenesis, and sperm quality (6). The available literature indicates that the risk of permanent gonadal dysfunction may increase in certain patients of either sex following cumulative doses (26). Another study, albeit with a limited sample size, identified a positive correlation between radioiodine dose and FSH levels over a mean follow-up period exceeding seven years. However, their results did not demonstrate a significant impact of radioiodine treatment on infertility rates (27).

In a sample of 12 men with DTC undergoing I-131 therapy, an increase in serum FSH levels and a dose-dependent impairment of spermatogenesis were observed. However, clinically significant effects were mainly seen in individuals receiving multiple doses totaling over 100 mCi (5). Conversely, our results showed that levels of LH, DHT, DHEA, and T did not change significantly from before to after RIT. T secretion and spermatogenesis depend on the hormones FSH and LH, with FSH serving as a key indicator of spermatogenesis and LH playing a vital role in T production. These hormones are produced in the anterior pituitary gland (28). When assessing infertility, measuring LH and FSH is important because they have an inverse relationship with sperm concentration (29). Additionally, LH levels are linked to sperm motility (30). A meta-analysis found increases in FSH, LH, and T levels, as well as in sperm quality parameters; however, at one-year follow-up these increases were not statistically significant (1). Our findings suggest there were no changes in serum T levels or in the occurrence of oligospermia despite a temporary rise in FSH levels. These results are consistent with a study of testicular function following radioiodine therapy in patients with thyroid cancer (31). The transient increase in FSH generally reverses several months after receiving RAI therapy, indicating that high cumulative I-131 activity does not necessarily cause permanent infertility. Our data suggest that testicular dysfunction caused by I-131 therapy is likely temporary, consistent with another study in which all patients maintained normal T levels (9). T affects the paracrine activity of Sertoli cells, promoting their function and helping the maturation of spermatogonia into spermatocytes (32). Studies have demonstrated that Leydig cells in the testes are more resistant to radiation than the reproductive epithelium and are damaged only by high doses of therapeutic radiation (33). However, this study found no statistically significant differences in LH and T levels before and after RAI treatment, even in subgroup analyses. This indicates that Leydig cell function remains unaffected after RAI, although further research is needed to determine whether higher doses of RAI would produce different results.

DHEA, produced by the adrenal glands, is a precursor of T and estrogens, which are crucial for male reproductive health and sperm production (34). Reported DHT levels are likely to influence prostate growth (35). T can also be converted by the enzyme 5α-reductase 2 into a potent non-aromatizable androgen, 5α-DHT, which is required for the masculinization of the external genitalia in utero and for many of the changes associated with puberty, including the growth and activity of the prostate gland (36). Additionally, DHEA exhibits anti-inflammatory properties (37), while DHT contributes to improved oocyte quality and increased likelihood of conception. Both DHT and DHEA offer potential benefits for fertility (38). Our findings revealed that levels of DHT, DHEA, and T did not change significantly before and after RIT. Our investigation also assessed another factor: AMH levels before and after RIT did not change significantly. evidence shows that serum AMH levels are markedly decreased in infertile men (39). In our study, their levels remained unchanged before and after the intervention. AMH (Müllerian inhibiting substance, AMH) and inhibin B (InhB) are produced by the Sertoli cells of the testes. AMH is secreted during testis development and in adulthood, whereas sperm production in adult men is regulated by InhB. These hormones are also recognized as regulators of homeostasis. In a cohort study involving men over 50, InhB levels were inversely associated with age, although no age-related effect was observed in young men (40). Furthermore, these hormones were correlated with each other. The health status of older adults is influenced by the AMH/InhB ratio, although they (AMH and InhB) may be independent (41). In an animal study, AMH and InhB cooperatively inhibited testicular cancer, and AMH also suppressed aromatase activity in FSH-stimulated sertoli cells, independent of LH. Future research could explore AMH's role after RIT with respect to its physiological function in the testis (42). In infertile men, low serum AMH levels are associated with severely impaired gonadal function, as evidenced by compromised semen quality and a reduced T-to-LH ratio. Additionally, the role of circulating AMH during adulthood is less well understood (39).

Semen analysis currently serves as the benchmark for assessing male fertility status; however, a standard semen analysis does not guarantee fertility (1). Semen analysis was conducted within one hour of collection in accordance with the WHO laboratory manual, supplemented by additional guidelines (15). The assessment evaluated semen parameters, including pH, viscosity, volume, sperm concentration, motility, round cells, and morphology. Poor semen quality, characterized by abnormal physical parameters, low sperm count, reduced motility, and irregular morphology, is a significant contributor to male infertility. Our study results indicate a significant increase in semen volume, total sperm count, and sperm motility, particularly rapid progressive motility. Total sperm count is the number of spermatozoa in the ejaculate, calculated by multiplying sperm concentration by semen volume (43). The normal sperm concentration is ≥20 million sperm per milliliter of semen (3), and our study results confirm this.

A man is considered fertile when total motility is at least 40% and progressive motility is at least 32%. Sperm motility refers to the ability of sperm to move efficiently and is a crucial factor in fertility (44). Our results for motility and rapid progressive motility are consistent with previous reports that demonstrate that sperm motility is regulated by various factors, including intracellular and extracellular pH, the concentrations of calcium ions (Ca^{2+}) and bicarbonate ions (HCO_3-), and sperm surface proteins. Factors such as radiation, psychological stress, and environmental pollution can impair motility. For example, radiation exposure, mutations in CatSper genes, or psychological stress through hormonal changes and impaired calcium metabolism can impair sperm motility (44). Fertility clinics typically analyze sperm parameters such as density, count, motility, and morphology. Still, sperm DNA fragmentation testing, such as the SCSA, is often overlooked due to limited awareness, cost concerns, or practical considerations. This test, first described by Son in 1980, uses flow cytometry to detect DNA fragmentation through acid- or heat-induced denaturation and identifies poor-quality sperm (45). Healthy and mature sperm nuclei contain abundant disulfide bonds, resulting in their DNA being in the double-stranded form (46).

The SCSA detects sperm DNA fragmentation; rates exceeding 30% are associated with a significant decrease in term pregnancies. Multiple RAI treatments can cause permanent testicular damage, resulting in a 50% reduction in sperm count and a 40% reduction in FSH levels. These effects occur in 20% of patients who undergo multiple treatments and in 10% of those who receive a single treatment. Despite these potential risks, our findings indicate minimal changes in sperm DNA fragmentation measured before and after RIT, suggesting a limited impact on DNA integrity, which is consistent with Anderson's findings (47). The mechanisms underlying DNA damage in sperm may include unrepaired DNA breaks during chromatin remodeling and packaging, as well as abortive apoptosis during spermatogenesis. Other possible causes include the effects of endogenous endonucleases and caspases; exposure to various genotoxic agents for therapeutic purposes or from occupational or environmental sources; infections; certain types of cancer;

and oxidative damage (48). Taken together, these points suggest that administration of RAI is unlikely to impair long-term male fertility in DTC patients receiving doses of 100 mCi (3.7 GBq) or higher (49). Therefore, conflicting findings exist regarding the effect of RAI on semen quality; this relationship may depend on RAI dose and follow-up duration after treatment (1).

Study Limitations

The study assessed subjects before therapy and again two weeks afterward, thereby potentially overlooking long-term effects on male fertility. Exclusion criteria may limit the applicability of the results to the broader thyroid cancer patient population, as individuals with factors that influence fertility, such as varicocele or lifestyle factors, were excluded. Although the study evaluated sperm DNA fragmentation and semen parameters, the lack of a comprehensive longitudinal follow-up may hinder a thorough assessment of permanent fertility changes. Variations in RAI dosing and the lack of consensus on optimal dosing complicate the interpretation of results. Future research with diverse and extended follow-up periods is necessary to understand the long-term impact of RAI therapy on male fertility.

Conclusion

Radioiodine therapy for thyroid cancer may temporarily increase serum FSH levels, indicating a transient impact on gonadal function. Other reproductive hormones, such as LH, DHT, DHEA, and T, remain unaffected. Our results did not demonstrate that male patients with DTC experienced infertility after receiving a cumulative RAI dose of 150 mCi. Larger sample sizes and longer follow-up are needed to further assess the possible effects of sex and gonadal hormones on sperm DNA fragmentation. Further investigation into the role of AMH post-RIT in testicular physiological function is recommended.

Ethics

Ethics Committee Approval: Ethical clearance for this research was obtained from the Fasa University of Medical Sciences Ethics Committee on May 22, 2022, and the study was conducted in accordance with the approved protocol. This committee reviewed and endorsed the study's ethical considerations (ethical code: REC.1401.020, date: 11.05.2025).

Informed Consent: The authors declare that they have no competing interests.

Acknowledgments

The authors thank the Vice-Chancellor for Research at Fasa University of Medical Sciences.

Footnotes

Authorship Contributions

Surgical and Medical Practices: M.A., R.H., Concept: M.A., M.S., Design: M.A., M.S., Data Collection or Processing: R.H., M.S., Analysis or Interpretation: R.H., A.T., M.S., Literature Search: R.H., Writing: R.H., A.T., M.S.

Conflict of Interest: No conflict of interest was declared by the authors.

Financial Disclosure: The authors declared that this study has received no financial.

Availability of Data

The dataset analyzed during the current study is available from the corresponding author upon reasonable request.

References

1. Cai Y, Yang Y, Pang X, Li S. The effect of radioactive iodine treatment for differentiated thyroid cancer on male gonadal function: a meta-analysis. Endocr Connect. 2023;12:e230299.
2. Sherman SI, Perrier N, Clayman GL. Thyroid cancer. 60 years of survival outcomes at The University of Texas MD Anderson Cancer Center: Springer; 2012;295-310.
3. Silver RJ, Parangi S. Management of thyroid incidentalomas. Surg Clin North Am. 2004;84:907-919.
4. Haugen BR, Alexander EK, Bible KC, Doherty GM, Mandel SJ, Nikiforov YE, Pacini F, Randolph GW, Sawka AM, Schlumberger M, Schuff KG, Sherman SI, Sosa JA, Steward DL, Tuttle RM, Wartofsky L. 2015 American Thyroid Association management guidelines for adult patients with thyroid nodules and differentiated thyroid cancer: the American Thyroid Association guidelines task force on thyroid nodules and differentiated thyroid cancer. Thyroid. 2016;26:1-133.
5. Henderson BE, Ross RK, Pike MC, Casagrande JT. Endogenous hormones as a major factor in human cancer. Cancer Res. 1982;42:3232-3239.
6. Nies M, Arts EGJM, van Velsen EFS, Burgerhof JGM, Muller Kobold AC, Corssmit EPM, Netea-Maier RT, Peeters RP, van der Horst-Schrivers ANA, Cantineau AEP, Links TP. Long-term male fertility after treatment with radioactive iodine for differentiated thyroid carcinoma. Eur J Endocrinol. 2021;185:775-782.
7. Bendarska-Czerwińska A, Zmarzły N, Morawiec E, Panfil A, Bryś K, Czarniecka J, Ostenda A, Dziobek K, Sagan D, Boroń D, Michalski P, Pallazo-Michalska V, Grabarek BO. Endocrine disorders and fertility and pregnancy: an update. Front Endocrinol (Lausanne). 2023;13:970439.
8. Y, Cui L, Lu Y, Tan J, Dong X, Ni T, Yan J, Guan Y, Hao G, Liu JY, Zhang B, Wei D, Hong Y, He Y, Qi J, Xu B, Lu J, Zhang Q, Zhao S, Ji X, Du X, Zhang J, Liu J, Wang J, Huang Y, Huang D, Du Y, Vankelecom H, Zhang H, Chen ZJ. Prednisone vs placebo and live birth in patients with recurrent implantation failure undergoing in vitro fertilization: a randomized clinical trial. JAMA. 2023;329:1460-1468.
9. van Rijswijk J, Pham CT, Dreyer K, Verhoeve HR, Hoek A, de Bruin JP, Nap AW, Wang R, Lambalk CB, Hompes PGA, Mijatovic V, Karnon JD, Mol BW. Oil-based or water-based contrast for hysterosalpingography in infertile women: a cost-effectiveness analysis of a randomized controlled trial. Fertil Steril. 2018;110:754-760.
10. Rosário PW, Barroso AL, Rezende LL, Padrão EL, Borges MA, Guimarães VC, Purisch S. Testicular function after radioiodine therapy in patients with thyroid cancer. Thyroid. 2006;16:667-670.
11. Carballo M, Quiros RM. To treat or not to treat: the role of adjuvant radioiodine therapy in thyroid cancer patients. J Oncol. 2012;2012:707156.

12. Siegel RL, Miller KD, Jemal A. Cancer statistics, 2018. CA Cancer J Clin. 2018;68:7-30.
13. Nguyen NC, Anigati EM, Desai NB, Öz OK. Radioactive iodine therapy in differentiated thyroid cancer: an update on dose recommendations and risk of secondary primary malignancies. Semin Nucl Med. 2024;54:488-496.
14. Björndahl L, Barratt CL, Mortimer D, Jouannet P. 'How to count sperm properly': checklist for acceptability of studies based on human semen analysis. Hum Reprod. 2016;31:227-232.
15. Kandil H, Agarwal A, Saleh R, Boitrelle F, Arafa M, Vogiatzi P, Henkel R, Zini A, Shah R. Editorial commentary on draft of World Health Organization sixth edition laboratory manual for the examination and processing of human semen. World J Mens Health. 2021;39:577-580.
16. Bonde JP, Ernst E, Jensen TK, Hjollund NH, Kolstad H, Henriksen TB, Scheike T, Giwercman A, Olsen J, Skakkebaek NE. Relation between semen quality and fertility: a population-based study of 430 first-pregnancy planners. Lancet. 1998;352:1172-1177.
17. Evenson DP, Larson KL, Jost LK. Sperm chromatin structure assay: its clinical use for detecting sperm DNA fragmentation in male infertility and comparisons with other techniques. J Androl. 2002;23:25-43.
18. Spanò M, Bonde JP, Hjøllund HI, Kolstad HA, Cordelli E, Leter G. Sperm chromatin damage impairs human fertility. The Danish First Pregnancy Planner Study Team. Fertil Steril. 2000;73:43-50.
19. Agarwal A, Sharma R. Sperm chromatin assessment. Textbook of assisted reproductive techniques: CRC Press. 2023.
20. Rochdi C, Allai L, Bellajdel I, Taheri H, Saadi H, Mimouni A, Choukri M. Evaluation of sperm DNA fragmentation using halosperm technique after the freezing-thawing process in men: a study on the validation of the SCD protocol. J Reprod Infertil. 2024;25:12-19.
21. Hyer S, Vini L, O'Connell M, Pratt B, Harmer C. Testicular dose and fertility in men following I(131) therapy for thyroid cancer. Clin Endocrinol (Oxf). 2002;56:755-758.
22. De Felice F, Marchetti C, Marampon F, Cascialli G, Muzii L, Tombolini V. Radiation effects on male fertility. Andrology. 2019;7:2-7.
23. Wichers M, Benz E, Palmedo H, Biersack HJ, Grünwald F, Klingmüller D. Testicular function after radioiodine therapy for thyroid carcinoma. Eur J Nucl Med. 2000;27:503-507.
24. Rosario PW, Xavier AC, Calsolari MR. Recombinant human thyrotropin in thyroid remnant ablation with 131-iodine in high-risk patients. Thyroid. 2010;20:1247-1252.
25. Stamatiades GA, Carroll RS, Kaiser UB. GnRH-A key regulator of FSH. Endocrinology. 2019;160:57-67.
26. Ko KY, Yen RF, Lin CL, Cheng MF, Huang WS, Kao CH. Pregnancy outcome after I-131 therapy for patients with thyroid cancer: a nationwide population-based cohort study. Medicine (Baltimore). 2016;95:e2685.
27. Sawka AM, Lakra DC, Lea J, Alshehri B, Tsang RW, Brierley JD, Straus S, Thabane L, Gafni A, Ezzat S, George SR, Goldstein DP. A systematic review examining the effects of therapeutic radioactive iodine on ovarian function and future pregnancy in female thyroid cancer survivors. Clin Endocrinol (Oxf). 2008;69:479-490.
28. Fakhrildin MB. Correlation between seminal fluid analysis and levels of gonadotropins in serum and seminal plasma of normozoospermic men and infertile patients. 2007.
29. Sheikh MA, Begum B, KHAN MS, Turabi A, DANYAL A, Zaidi SSH. Azoospermia & oligozoospermia: semen and hormonal analysis of patients. The Professional Medical Journal. 2005;12:80-84.
30. Zhao W, Jing J, Shao Y, Zeng R, Wang C, Yao B, Hang D. Circulating sex hormone levels in relation to male sperm quality. BMC Urol. 2020;20:101.
31. Rosário PW, Ward LS, Carvalho GA, Graf H, Maciel RM, Maciel LM, Maia AL, Vaisman M; Sociedade brasileira de endocrinologia e metabologia. Thyroid nodules and differentiated thyroid cancer: update on the Brazilian consensus. Arq Bras Endocrinol Metabol. 2013;57:240-264.
32. Tyagi V, Scordo M, Yoon RS, Liporace FA, Greene LW. Revisiting the role of testosterone: are we missing something? Rev Urol. 2017;19:16-24.
33. Liang P, Changyue L, Dan M, Yajun L, Xiaojie W, Ying L. Study on the effect of postoperative radioactive 131 I treatment for differentiated thyroid cancer on fertility in people of reproductive age. Journal of Clinical Military Medicine. 2020;48:1099-1100.
34. Urysiak-Czubatka I, Kmieć ML, Broniarczyk-Dyła G. Assessment of the usefulness of dihydrotestosterone in the diagnostics of patients with androgenetic alopecia. Postepy Dermatol Alergol. 2014;31:207-215.
35. Swerdloff RS, Wang C. Dihydrotestosterone: a rationale for its use as a non-aromatizable androgen replacement therapeutic agent. Baillieres Clin Endocrinol Metab. 1998;12:501-506.
36. Kang HJ, Imperato-McGinley J, Zhu YS, Rosenwaks Z. The effect of 5α-reductase-2 deficiency on human fertility. Fertil Steril. 2014;101:310-316.
37. Danenberg HD, Alpert G, Lustig S, Ben-Nathan D. Dehydroepiandrosterone protects mice from endotoxin toxicity and reduces tumor necrosis factor production. Antimicrob Agents Chemother. 1992;36:2275-2279.
38. Nehra D, Le HD, Fallon EM, Carlson SJ, Woods D, White YA, Pan AH, Guo L, Rodig SJ, Tilly JL, Rueda BR, Puder M. Prolonging the female reproductive lifespan and improving egg quality with dietary omega-3 fatty acids. Aging Cell. 2012;11:1046-1054.
39. Holt R, Yahyavi SK, Kooij I, Andreassen CH, Andersson AM, Juul A, Jørgensen N, Blomberg Jensen M. Low serum anti-müllerian hormone is associated with semen quality in infertile men and not influenced by vitamin D supplementation. BMC Med. 2023;21:79.
40. Zarén P, Alson S, Henic E, Bungum M, Giwercman A. Interaction between serum levels of anti-müllerian hormone and the degree of sperm DNA fragmentation measured by sperm chromatin structure assay can be a predictor for the outcome of standard in vitro fertilization. PLoS One. 2019;14:e0220909.
41. Chong YH, Dennis NA, Connolly MJ, Teh R, Jones GT, van Rij AM, Farrand S, Campbell AJ, McLennan IS. Elderly men have low levels of anti-müllerian hormone and inhibin B, but with high interpersonal variation: a cross-sectional study of the sertoli cell hormones in 615 community-dwelling men. PLoS One. 2013;8:e70967.
42. Evenson D, Jost L. Sperm chromatin structure assay is useful for fertility assessment. Methods Cell Sci. 2000;22:169-189.
43. Oehninger S, Franken DR, Ombelet W. Sperm functional tests. Fertil Steril. 2014;102:1528-1533.
44. Sanità OMD. WHO laboratory manual for the examination and processing of human semen: World Health Organization; 2010.
45. Chakraborty S, Saha S. Understanding sperm motility mechanisms and the implication of sperm surface molecules in promoting motility. Middle East Fertility Society Journal. 2022;27:4.
46. Evenson DP. The Sperm Chromatin Structure Assay (SCSA(®)) and other sperm DNA fragmentation tests for evaluation of sperm nuclear DNA integrity as related to fertility. Anim Reprod Sci. 2016;169:56-75.
47. Bungum M, Giwercman A, Spanò M. Male subfertility and sperm chromatin damage. In: Zini A, Agarwal A, editors. Sperm chromatin: biological and clinical applications in male infertility and assisted reproduction. New York, NY: Springer Science+Business Media; 2011. p. 321-335.
48. Anderson C, Engel SM, Weaver MA, Zevallos JP, Nichols HB. Birth rates after radioactive iodine treatment for differentiated thyroid cancer. Int J Cancer. 2017;141:2291-2295.
49. Sakkas D, Alvarez JG. Sperm DNA fragmentation: mechanisms of origin, impact on reproductive outcome, and analysis. Fertil Steril. 2010;93:1027-1036.

Original Article

Mol Imaging Radionucl Ther 2026;35(1):10-18 ***DOI:****10.4274/mirt.galenos.2025.58751*

Automated Segmentation of Liver and Liver Tumors with SwinUNETR and UNET Neural Networks on ^{18}F-FDG PET/CT

SwinUNETR ve Residual UNET Nöral Ağlar ile ^{18}F-FDG PET/BT Karaciğer ve Karaciğer Tümörlerin Otomatik Segmentasyonu

Burak Demir, Hatice Kübra Yurtçu, Merve Ağcıoğlu Atalay, Fikret Ertek

University of Health Sciences Türkiye, Şanlıurfa Mehmet Akif İnan Training and Research Hospital, Clinic of Nuclear Medicine, Şanlıurfa, Türkiye

Abstract

Objectives: To develop and evaluate automated segmentation models for the liver and hepatic tumors on ^{18}F-fluorodeoxyglucose positron emission tomography/computed tomography (^{18}F-FDG PET/CT) using SwinUNETR and residual UNET architectures, and to assess their accuracy in complex clinical cases.

Methods: In this single-center retrospective study, 100 patients (48 males, 52 females; mean age 61±14 years) with ^{18}F-FDG-avid hepatic lesions from various primary malignancies were included. Liver segmentation was performed on non-contrast CT images using pairs of SwinUNETR and residual UNET models, and tumor segmentation was performed on masked PET images using separately trained pair of SwinUNETR and residual UNET model. Model performance was evaluated using the dice similarity coefficient (DSC), volumetric bias, and Bland-Altman analysis for metabolic tumor volume (MTV) and total lesion glycolysis (TLG).

Results: For liver segmentation, SwinUNETR achieved a median DSC of 97.59% (range: 95.41-98.93%) with a median volumetric bias of -0.94% (LoA: -3.76% to +0.50%), while residual UNET achieved a median DSC of 97.85% (range: 94.81-98.80%) with a median volumetric bias of -0.34% (LoA: -2.63% to +1.16%). For tumor segmentation, SwinUNETR achieved a median DSC of 92.62% (range: 80.75–97.46%), an MTV bias of -8.60% (LoA: -31.62% to +1.21%), and a TLG bias of -6.40% (LoA: -25.58% to +0.76%). Residual UNET achieved a median DSC of 93.07% (range: 80.74–98.18%), MTV bias of -4.33% (LoA: -24.36% to +10.12%), and TLG bias of -11.10% (LoA: -30.8% to +4.52%). Most MTV and TLG measurements were within ±10% of reference values.

Conclusion: Both SwinUNETR and Residual UNET achieved excellent liver segmentation accuracy and clinically acceptable tumor segmentation performance on ^{18}F-FDG PET/CT, with SwinUNETR showing slightly better performance in liver volumetric measurements. These open-source models could be integrated into clinical workflows to automate segmentation tasks, facilitate treatment planning for liver-directed therapies, and support reproducible quantitative imaging analyses.

Keywords: Deep learning, SwinUNETR, positron-emission tomography, molecular imaging, fluorodeoxyglucose, image processing

Öz

Amaç: Bu çalışmanın amacı SwinUNETR ve Residual UNET mimarilerini kullanarak ^{18}F-florodeoksiglukoz pozitron emisyon tomografisi/bilgisayarlı tomografinin (^{18}F-FDG PET/BT) görüntülerinde karaciğer ve hepatik tümörlerin otomatik segmentasyon modellerini geliştirmek ve değerlendirmek; ayrıca bu modellerin karmaşık klinik olgulardaki doğruluğunu incelemek olarak belirlenmiştir.

Address for Correspondence: Burak Demir, University of Health Sciences Türkiye, Şanlıurfa Mehmet Akif İnan Training and Research Hospital, Clinic of Nuclear Medicine, Şanlıurfa, Türkiye
E-mail: 4burakfe@gmail.com **ORCID ID:** orcid.org/0000-0002-0966-9988

Received: 15.08.2025 **Accepted:** 20.10.2025 **Epub:** 01.12.2025 **Publication Date:** 03.02.2026

Cite this article as: Demir B, Yurtçu HK, Ağcıoğlu Atalay M, Ertek F. Automated segmentation of liver and liver tumors with SwinUNETR and UNET neural networks on ^{18}F-FDG PET/CT. Mol Imaging Radionucl Ther. 2026;35(1):10-18.

Yöntem: Tek merkezli, retrospektif bu çalışmaya, çeşitli primer ve metastatik ^{18}F-FDG tutulumu gösteren karaciğer tümörleri bulunan 100 hasta (48 erkek, 52 kadın; ortalama yaş 61±14 yıl) dahil edildi. Karaciğer segmentasyonu kontrastsız BT görüntülerinde, tümör segmentasyonu ise maskeleme yapılmış PET görüntülerinde gerçekleştirildi. SwinUNETR ve Residual UNET modelleri karaciğer ve tümör segmentasyonu için ayrı ayrı eğitildi. Model performansı dice benzerlik katsayısı (DSC), volumetrik bias ve metabolik tümör hacmi (MTV) ile total lezyon glikolizi (TLG) değerleri Bland-Altman analizi ile karşılaştırıldı.

Bulgular: Karaciğer segmentasyonunda SwinUNETR modeli ile %97,59 (aralık: %95,41-98,93) medyan DSC ve -%0,94 (LoA: -%3,76 ila +%0,50) medyan volumetrik bias elde edilmiştir. Residual UNET modelinde ise %97,85 (aralık: %94,81-98,80) medyan DSC ve -%0,34 (LoA: -%2,63 ila +%1,16) bias değerleri izlenmiştir. Tümör segmentasyonunda SwinUNETR modelinde %92,62 (aralık: %80,75-97,46) medyan DSC, -%8,60 MTV bias (LoA: -%31,62 ila +%1,21) ve -%6,40 TLG bias (LoA: -%25,58 ila +%0,76) değerleri gözlenmiştir. Residual UNET modeli ise %93,07 (aralık: %80,74-98,18) medyan DSC, -%4,33 MTV bias (LoA: -%24,36 ila +%10,12) ve -%11,10 TLG bias (LoA: -%30,8 ila +%4,52) değerlerine sahip olarak izlenmiştir. MTV ve TLG ölçümlerinin çoğu referans değerlerin ±%10 aralığında yer aldı.

Sonuç: SwinUNETR ve Residual UNET modelleri, ^{18}F-FDG PET/BT görüntülerinde yüksek derecede karaciğer segmentasyon doğruluğu ve klinik olarak kabul edilebilir tümör segmentasyonu performansı sağlamıştır. SwinUNETR modeli ise karaciğer segmentasyonunda Residual UNET modeline göre daha iyi sonuç vermiştir. Bu açık kaynaklı modeller, klinik iş akışlarına entegre edilerek segmentasyon görevlerini otomatikleştirebilir, karaciğere yönelik tedavi planlamasını kolaylaştırabilir ve tekrarlanabilir nicel görüntüleme analizlerini destekleyebilir.

Anahtar kelimeler: Derin öğrenme, SwinUNETR, pozitron emisyon tomografisi, moleküler görüntüleme, florodeoksiglikoz, görüntü işleme

Introduction

Primary liver malignancies, particularly hepatocellular carcinoma (HCC), represent a major global health burden, ranking as one of the leading causes of cancer-related mortality worldwide (1). In addition to primary tumors, the liver is a frequent site of metastatic spread from various malignancies, including colorectal, breast, and pancreatic cancers (2,3,4). Early detection and accurate characterization of hepatic lesions are essential, as the prognosis of patients with liver involvement depends heavily on timely diagnosis and appropriate therapeutic intervention. Proper treatment planning—whether through surgical resection, transplantation, systemic therapy, or locoregional approaches—can significantly improve survival outcomes in both primary and secondary hepatic malignancies.

Accurate delineation of the liver and its tumors plays a pivotal role in several advanced treatment strategies. For therapies such as selective internal radiation therapy (SIRT) (SIRT, also known as radioembolization) and stereotactic body radiotherapy, precise volumetric and spatial characterization of tumor burden is required to optimize dosimetry, minimize healthy tissue damage, and maximize therapeutic efficacy (5-7). Furthermore, quantitative imaging biomarkers that have been shown to be reliable prognostic factors after radioembolization, such as metabolic tumor volume (MTV) and total lesion glycolysis (TLG) on ^{18}F-fluorodeoxyglucose positron emission tomography/computed tomography (^{18}F-FDG PET/CT), rely on precise segmentation to ensure reproducibility across clinical and research settings (8,9).

Over the past decade, deep learning–based methods have revolutionized medical image segmentation, with convolutional neural networks (CNNs) and, more recently, transformer-based architectures delivering state-of-the-art performance (10-12). Tools such as TotalSegmentator have demonstrated the potential of generalized pre-trained models to achieve high accuracy in multi-organ segmentation tasks (13). In liver imaging, these approaches have significantly reduced the need for labor-intensive manual contouring, thus accelerating clinical workflows and enabling large-scale quantitative studies.

The SwinUNETR architecture, a transformer-based model incorporating hierarchical shifted-window self-attention and UNet-style encoder–decoder design, has shown strong performance in complex 3D segmentation tasks (10,11). By leveraging global contextual information while preserving fine anatomical details, SwinUNETR has the potential to outperform conventional CNN-based architectures in challenging segmentation scenarios. In clinical reality, diseased livers often present with anatomical distortions caused by ascites, postoperative changes, large tumor burdens, or extensive metastatic infiltration. Such conditions may degrade the performance of general-purpose segmentation models, underscoring the need for disease-specific model training tailored to these complex cases.

Previous studies on liver segmentation using neural networks have generally employed fully convolutional architectures such as Residual UNET and have been performed on contrast-enhanced CT images. For example, in a recent study, Yashaswini et al. (14) evaluated the performance of Residual UNET models for liver and tumor segmentation on CT imaging and reported a Dice score of 91.44% for liver segmentation. Additionally, several other studies have investigated liver and tumor segmentation using CNNs (15,16). However, the utility and potential superiority of

SwinUNETR for liver and tumor segmentation, compared to Residual UNET models, have not yet been explored. Furthermore, although there are multiple studies on tumor segmentation in PET imaging, research combining PET and CT imaging for segmentation remains rare.

In this study, we aimed to develop and evaluate automated segmentation models, using both SwinUNETR-V2 and residual U-Net architectures, to segment the liver and hepatic tumors from ^{18}F-FDG PET/CT images. Our goal was to assess their accuracy in the context of challenging clinical cases and to explore the feasibility of disease-specific segmentation models that can maintain robust performance in anatomically complex livers. The developed models are also intended for use in conjunction with the previously developed radioembolization dosimetry module for 3D Slicer (17).

Materials and Methods

Patients and Study Design

This single-center, retrospective study included patients with ^{18}F-FDG-avid hepatic lesions from various malignancies who underwent ^{18}F-FDG PET/CT imaging from January 2025 to July 2025. Written informed consent was obtained from all patients before imaging. Exclusion criteria were: (1) significant respiratory artefacts; (2) artefacts secondary to patient motion; and (3) artefacts secondary to metallic objects or prostheses on CT imaging. The study was approved by the Ethics Committee of Harran University (approval no: HRÜ-25.11.02, date: 16.06.2025), with additional approval from the institutional review board. The developed segmentation models and training scripts (18,19), images of four patients for testing (20), and the SlicerAether segmentation module for 3D Slicer (18) are available in public repositories.

^{18}F-FDG PET/CT Protocol and Preprocessing of the Data

Imaging was performed using a Siemens Biograph Horizon™ 4R system. Patients fasted for at least 6 hours before imaging, and blood glucose levels were checked prior to the scan. Those with a blood glucose level above 200 mg/dL did not undergo scanning. Images were acquired from the vertex to the proximal femur with the patient in the supine position. Whole-body ^{18}F-FDG PET/CT imaging was performed approximately 1 h after an intravenous injection of ^{18}F-FDG at 3.7 MBq/kg. For PET/CT imaging, PET images were acquired for 90 seconds per bed position and were reconstructed using attenuation correction measured from non-contrast CT images. For reconstruction of PET images, the TrueX+TOF (UltraHD-PET) algorithm was used with 4 iterations and 10 subsets, a 5-mm post-processing Gaussian filter, and a 180 × 180 matrix. The resulting voxel size was 4.11392 × 4.11392 × 1.50 mm. All PET images were converted to standardized uptake values (SUVs), normalized to body weight, and resampled to an isotropic voxel size of 2 × 2 × 2 mm prior to training. No further normalization other than conversion to SUV values was used.

Non-contrast-enhanced CT images were acquired at 130 kV with a variable tube current modulated according to patient weight using the CareDose4D (Siemens Healthineers) and reconstructed with a 512 × 512 matrix. The resulting voxel size was 1.367 × 1.367 × 1.50 mm. Similarly, the CT images were resampled to an isotropic voxel size of 2×2×2 mm before training. For CT images, voxel intensities were normalized using a linear scaling transformation in which values between -135 hounsfield unit (HU) and +215 HU were mapped to the range 0.0-10.0; values outside this range were clipped to the nearest boundary.

For preprocessing, PET and CT volumes were cropped to a bounding box encompassing the upper abdomen to remove empty voxels and reduce computational load. The liver was manually segmented on CT images for all patients, and the resulting liver masks were used to zero out voxels outside the liver in the PET volumes. A spherical reference volume of interest was placed in the non-tumoral liver parenchyma, and a threshold equal to 1.5 times the liver reference SUV_{mean} was used for manual tumor segmentation. Afterwards, the CT images, masked PET images, and liver and tumor segmentation masks were saved for further processing.

Training volumes were split into overlapping 96 × 96 × 96-voxel patches, yielding 680 training pairs. No patching was applied during testing; instead, a sliding-window inference with the same patch size was used. Preprocessing was performed using 3D Slicer (version 5.9) and custom Python scripts (21,22).

Model Architecture Loss Function and Training Parameters

A volumetric segmentation model based on the SwinUNETR architecture, originally proposed by Hatamizadeh et al. (10) and later extended by He et al. (11) as SwinUNETR-V2, was implemented. SwinUNETR-V2 integrates the Swin Transformer with a UNET-style encoder–decoder and residual convolutional blocks at the start of each Swin stage, enabling high representational capacity for 3D medical images (10,23). In this study, one SwinUNETR-V2 model was trained to segment the liver in CT images, and another model with identical parameters was trained to segment tumors in masked PET images. Both models used a feature size of 24, transformer depths of (2, 2, 2, 2), attention heads of (3, 6, 12, 24), a dropout path rate of 0.0, input volumes of 96 × 96 × 96 voxels, and gradient checkpointing to reduce memory usage. Each model had approximately 18.3 million trainable parameters and was trained with a batch size of 1.

We also utilized UNET-structured models with residual blocks for comparison with SwinUNETR models (12). The 3D residual UNET model was configured with an input batch size of 4 and a total of 76.8M trainable parameters. This network employed five resolution levels with channel sizes of 64, 128, 256, 512, and 1024; two residual units per level; strides of (2, 2, 2, 2) for down- and up-sampling; and 3 × 3 × 3 convolution kernels.

The implementation was based on the PyTorch and MONAI frameworks and executed on a graphics processing unit (GPU)-enabled system, allowing efficient handling of 3D volumetric data (20,21,22). The GPU and central processing unit models used for training were an NVIDIA GeForce RTX 4060 with 8 GB of VRAM and an Intel Core i3-9100F (3.60 GHz). The Dice similarity coefficient (DSC) was calculated as follows (24,25,26):

$$Dice\ score = \frac{2 \times |X \cap Y|}{|X| + |Y|}$$

Here, X denotes the set of voxels in the predicted segmentation; Y denotes the set of voxels in the ground-truth segmentation; and $|X \cap Y|$ denotes the number of overlapping voxels. Dice loss was defined as follows:

Dice loss = 1 – Dice score.

In addition, cross-entropy loss values were calculated, and a hybrid loss function was used for training:

Training Loss Function = 0.5 × Dice Loss + 0.5 × Cross Entropy Loss

Testing of the Models and Performance Evaluation Metrics

A total of four models were developed for the segmentation of the liver and liver lesions. For liver segmentation, the reference liver volume, the predicted liver volume, and their intersection were computed. Model performance was assessed using the DSC, where a value of 1 indicates perfect overlap between the predicted and reference segmentation, and a value of 0 indicates no overlap.

For tumor segmentation on PET images, the DSC was also used as the primary evaluation metric. In addition, MTV and TLG were calculated for both the reference and model-predicted segmentations. TLG was defined as:

$TLG = MTV \times SUV_{mean}$

Statistical Analysis

Descriptive statistics were reported as counts and percentages for categorical variables, and as mean ± standard deviation and median (range) for continuous variables. A p-value less than 0.05 was considered statistically significant for all analyses. Dice scores obtained from the SwinUNETR and residual UNET models were compared using the Wilcoxon signed-rank test.

For tumor segmentation, predicted and reference MTV and TLG values were compared using Bland-Altman plots. The bias, along with 95% confidence intervals (CIs) and limits of agreement (LoA), was calculated for both models. All statistical analyses were performed using RStudio (version 2025.05.1), IBM SPSS Statistics (version 27), and BA-plotteR (27,28).

Results

Patients and General Characteristics

A total of 110 patients were initially considered for inclusion. Six patients were excluded due to respiratory artifacts, and four were excluded due to metallic artifacts in the upper abdominal CT images. Consequently, 100 patients (48 males, 52 females) with various malignancies were included in the study. The mean age was 61±14 years. The most common primary malignancies were breast cancer (28%), colorectal carcinoma (23%), lung cancer (13%), gastric cancer (8%), and pancreatic cancer (6%). The remaining patients had HCC, lymphoma, ovarian cancer, esophageal cancer, gallbladder cancer, cervical cancer, soft tissue sarcoma, tumors of unknown origin, or thyroid cancer. More than half of the patients (55%) had more than five FDG-avid liver lesions, 22% had 2-5 FDG-avid lesions, and 23% had a single FDG-avid lesion. The liver reference SUV_{mean} was 2.17±0.48 g/mL, and the mean tumor SUV_{max} was 10.52±7.50 g/mL.

Patients were randomly assigned to a training set (n=85) and a test set (n=15). In the test set, nine patients were female and six were male. Primary malignancies in this group included breast cancer (n=6), colorectal carcinoma (n=3), lung cancer (n=2), and lymphoma (n=2). The remaining patients had pancreatic cancer, tumors of unknown origin, or esophageal cancer. The mean age of the test group was 59±15 years, and the mean reference liver SUV_{mean} was 2.25±0.32 g/mL.

Segmentation of Liver on CT Images

In the test group, the median reference liver volume was 1679 mL (range: 887.6-2536.3 mL). The SwinUNETR model achieved a median Dice score of 97.59% (range: 95.41%-98.93%). The median liver volume estimated by SwinUNETR was 1672.2 mL (range: 872.9-2414.4 mL). Bland-Altman analysis demonstrated a median bias of –0.94% (95% CI: -1.05 to -0.64), with lower and upper LoA of -3.76% and +0.50%, respectively (Figure 1). These results indicate that SwinUNETR slightly underestimated the liver volume but maintained high segmentation accuracy.

The Residual UNET model achieved a median dice score of 97.85% (range, 94.81-98.80%). The median liver volume estimated by Residual UNET was 1693.17 mL (range: 891.24-2361.7 mL). Bland-Altman analysis revealed a median bias of -0.34% (95% CI: -0.58 to -0.17); LoA: -2.63% to +1.16%. When comparing the dice scores of the two models, SwinUNETR had higher scores in 13 patients (87%) and lower scores in 2 patients (13%) (p=0.036; Figure 2). The DSC values for each patient and the differences between SwinUNETR and Residual UNET models in liver segmentation are given in Table 1.

Segmentation of Tumors on Masked PET Images

In the test group, the median number of liver tumors was 6 (range: 1-39), and the median reference MTV was 58.71 mL (range: 2.20-374.20 mL). The median SUV_{max}, SUV_{mean}, and TLG values in the reference segmentations were 9.98 g/mL (range: 5.46-18.65 g/mL), 4.76 g/mL (range: 3.20-9.21 g/mL), and 337.92 g (range: 8.76-3447.90 g), respectively.

The SwinUNETR model achieved a median dice score of 92.62% (range: 80.75%-97.46%). The median MTV and TLG estimated by SwinUNETR were 50.84 mL (range: 1.62-343.36 mL) and 287.11 g (range: 6.86-3334.18 g), respectively. In the Bland-Altman analysis, the SwinUNETR model demonstrated a median bias of -8.60% (95% CI: -16.8 to -2.15) for MTV, with lower and upper LoA of -31.62% and +1.21%, respectively. Similarly, SwinUNETR model had a median bias of -6.40% (95% CI: -10.08 to -2.13) for TLG, with lower and upper LoA of -25.58% and +0.76%, respectively.

The Residual UNET model achieved a median dice score of 93.07% (range: 80.74-98.18%). The medians of MTV and TLG estimated by Residual U-Net were 56.22 mL (range: 1.70-400.15 mL) and 269.20 g (range: 6.40-3015.43 g), respectively. In the Bland-Altman analysis, the Residual UNET model demonstrated a median bias of -4.33% (95% CI: -10.62% to -1.59%) for MTV, with lower and upper LoA of -24.36% and +10.12%, respectively. Similarly, the Residual UNET model showed a median bias of -11.10% (95% CI: -16.87 to -6.22) for TLG, with lower and upper LoA of -30.8% and +4.52%, respectively. When dice scores were compared, SwinUNETR outperformed Residual UNET in 8 patients (53%) and scored lower in 7 patients (47%) (p=0.570). Examples of patient segmentation results are shown in Figures 3 and 4. The DSC values for each patient

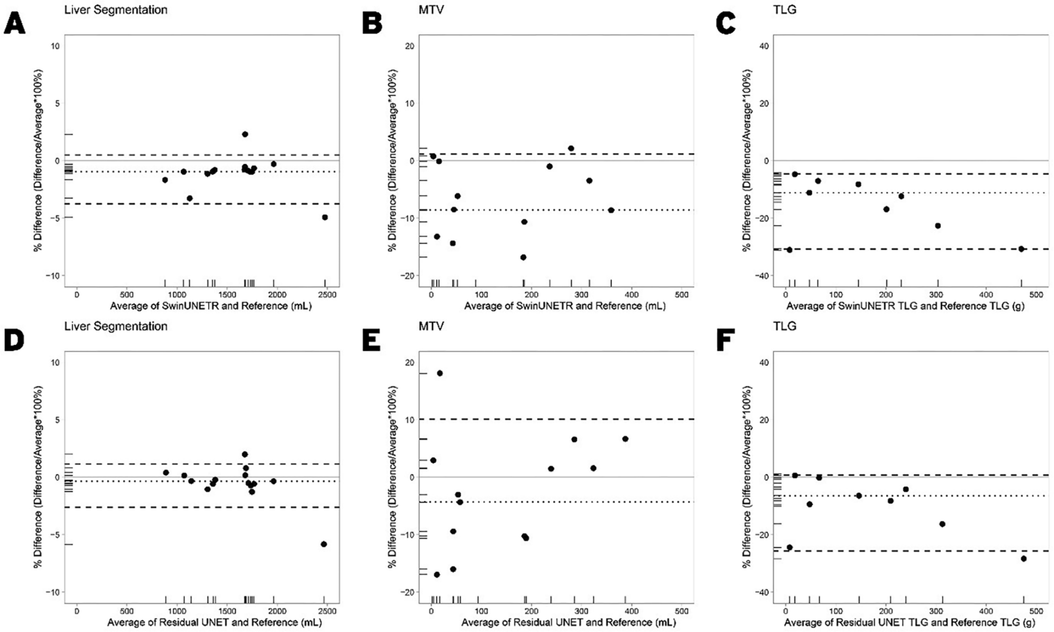

Figure 1. Bland-Altman plots of the segmentations predicted with SwinUNETR (A, B, C) and residual UNET (D, E, F) compared to the reference segmentation
MTV: Metabolic tumor volume, TLG: Total lesion glycolysis

and the differences between SwinUNETR and Residual UNET models in tumor segmentation are given in Table 2.

Discussion

In this study, both the SwinUNETR and residual UNET models achieved excellent performance in liver segmentation on CT images, with median dice scores exceeding 97% and narrow LoA. Although the SwinUNETR model slightly outperformed the residual UNET in terms of dice score, the difference was modest, and both approaches demonstrated highly reliable volumetric agreement with

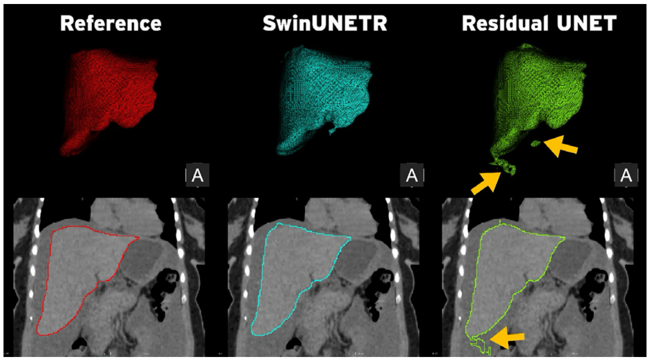

Figure 2. Reference and predicted segmentation results of a 36-year-old female patient with lymphoma. Significant ascites can be observed; SwinUNETR and Residual UNET models achieved dice scores of 97.65% and 97.36%, respectively, for liver segmentation. In the Residual UNET model, several extrahepatic regions are falsely identified as liver because of ascites (yellow arrows)

Table 1. The DSC values and differences in segmentation of liver calculated for both SwinUNETR and residual UNET models for each patient are given

Patients	SwinUNETR DSC	Residual UNET DSC	Difference
Patient 1	98.93%	98.20%	+0.73%
Patient 2	98.84%	98.60%	+0.24%
Patient 3	98.81%	98.80%	+0.02%
Patient 4	98.81%	98.64%	+0.16%
Patient 5	98.71%	98.50%	+0.21%
Patient 6	98.63%	98.51%	+0.12%
Patient 7	97.65%	97.36%	+0.29%
Patient 8	97.59%	97.85%	-0.26%
Patient 9	97.57%	98.12%	-0.54%
Patient 10	97.26%	97.20%	+0.06%
Patient 11	97.25%	97.13%	+0.12%
Patient 12	96.62%	96.56%	+0.06%
Patient 13	95.89%	95.88%	+0.01%
Patient 14	95.73%	95.25%	+0.48%
Patient 15	95.41%	94.81%	+0.59%

DSC: Dice similarity coefficient

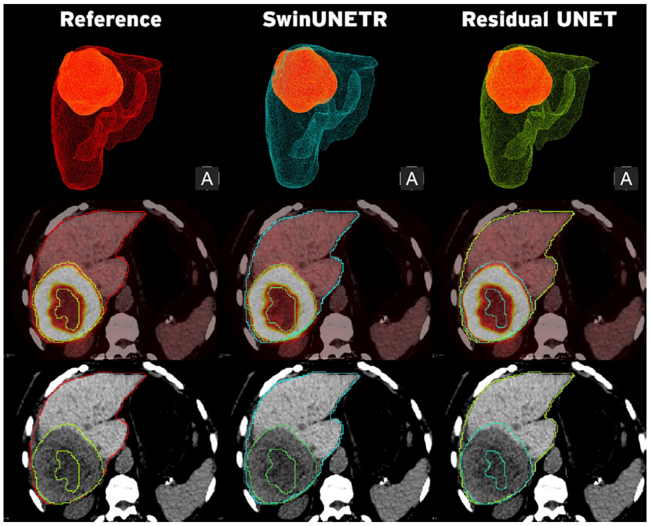

Figure 3. Reference and predicted segmentation results of an 81-year-old female patient with diffuse large B cell lymphoma. A large, strongly fluorodeoxyglucose-avid mass with areas of necrosis can be observed in the right lobe of the liver. SwinUNETR achieved dice scores of 98.71% for liver segmentation and 95.66% for tumor segmentation, while residual UNET achieved 98.50% for liver segmentation and 96.36% for tumor segmentation

Table 2. The DSC values and differences in segmentation of tumors calculated for both SwinUNETR and residual UNET models for each patient are given

Patients	SwinUNETR DSC	Residual UNET DSC	Difference
Patient 1	97.46%	97.33%	+0.13%
Patient 2	97.07%	98.18%	-1.11%
Patient 3	96.35%	89.91%	+6.44%
Patient 4	96.02%	93.99%	+2.03%
Patient 5	95.94%	94.70%	+1.23%
Patient 6	95.66%	96.36%	-0.70%
Patient 7	93.74%	94.58%	-0.84%
Patient 8	92.62%	90.29%	+2.32%
Patient 9	91.01%	85.93%	+5.08%
Patient 10	90.25%	93.07%	-2.81%
Patient 11	90.06%	93.07%	-3.01%
Patient 12	87.84%	94.29%	-6.44%
Patient 13	86.76%	89.17%	-2.41%
Patient 14	82.37%	87.53%	-5.16%
Patient 15	80.75%	80.74%	+0.02%

DSC: Dice similarity coefficient

reference segmentations. While both models may produce errors in patients with liver disease such as hepatosteatosis (Figure 5) or ascites (Figure 2) these results indicate that transformer-based and residual convolutional architectures are viable options for accurate hepatic segmentation in clinical and research settings.

For tumor segmentation on masked PET images, both models also demonstrated high performance, although their accuracy was lower than for liver segmentation. This is not unexpected, as tumor segmentation in FDG PET is inherently more challenging. Factors such as image noise, heterogeneous tracer uptake, and the presence of physiological uptake in adjacent structures can introduce false-positive voxels. Furthermore, variations in SUV thresholding methods can lead to differences in measured MTV and TLG, even for the same lesion. Despite these challenges, the majority of the predicted MTV and TLG values in our study were within ±10% of reference measurements, a level of agreement that is likely sufficient for many clinical applications, including treatment planning and response assessment. From a practical standpoint, these models could be integrated into clinical workflows to automate time-consuming segmentation tasks, assist in treatment planning for radiotherapy or radioembolization, and provide reproducible volumetric measurements for research studies. Given their open-source availability, they can also serve as a foundation for further development, including fine-tuning for specific scanner protocols or disease subtypes.

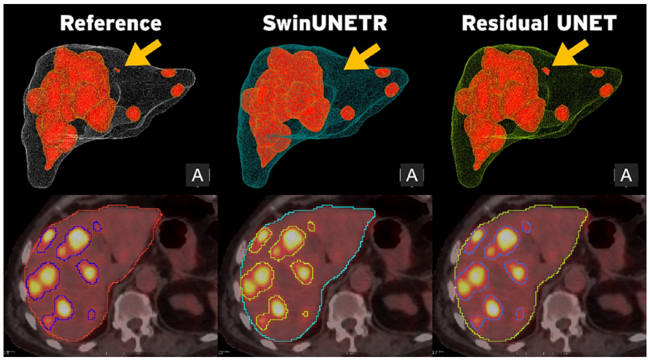

Figure 4. Reference and predicted segmentation results of an 81-year-old male patient with rectal carcinoma. Multiple strongly fluorodeoxyglucose-avid lesions can be observed in both lobes of the liver. While both models successfully predicted most lesions, SwinUNETR missed a small metastasis, and the residual UNET model predicted the same lesion to be larger than the reference (yellow arrows). SwinUNETR achieved dice scores of 97.26% (liver) and 97.07% (tumor); residual UNET achieved 97.20% (liver) and 98.18% (tumor)

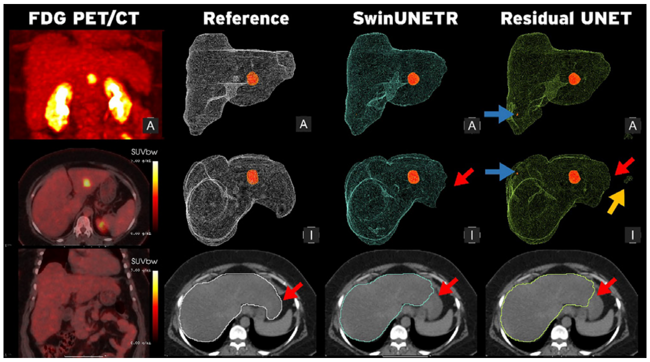

Figure 5. Reference and predicted segmentation results of a 56-year-old female patient with breast cancer metastasis of the liver. The patient had significant hepatosteatosis with hepatomegaly, and the lateral segment of the left lobe of the liver extended into the upper left quadrant. As a result, both the SwinUNETR and Residual UNET models failed to recognize the most lateral portions of the liver (red arrows); additionally, the UNET model produced a false-positive region erroneously labeled as liver (yellow arrow). In addition, the residual UNET model produced small false-positive foci in tumor segmentation due to noise in PET images (indicated by the blue arrows). SwinUNETR and Residual UNET models achieved Dice scores of 95.41% and 94.81% for liver segmentation and 91.01% and 85.93% for tumor segmentation, respectively

Our results compare favorably with the literature. Previous studies have reported Dice scores for liver segmentation in the range of 94-97% using deep learning methods (29,30,31), placing both of our models at the higher end of this reported range. In tumor segmentation using deep learning methods, Leung et al. (32) developed models using ^{18}F-FDG PET/CT and Galium-68 prostate-specific membrane antigen PET/CT and showed that median DSCs of up to 0.83 can be achieved for patients with lung cancer, melanoma, lymphoma, and prostate cancer. Although the dice scores achieved by both models (median >92%) indicate a high degree of accuracy, particularly given the heterogeneity of the test cohort, we masked the liver segment to simplify a two-pass algorithm; therefore, direct comparison was not feasible. Our approach differs by being specifically optimized for hepatic tumor segmentation on PET, potentially enhancing performance in cases of complex intrahepatic disease. In this context, Luo et al. (33) investigated the role of deep learning models in the detection and diagnosis of focal lesions in ^{18}F-FDG PET/CT images and achieved a Dice coefficient of 0.740. In addition, the developed models demonstrated high performance in differentiating benign from malignant liver nodules.

Study Limitations

Our study has several limitations. First, it was conducted at a single center; external validation on datasets from other institutions would be necessary to confirm generalizability. Second, although our models demonstrated high accuracy, tumor segmentation performance was still influenced by PET noise and by the thresholding approach used to generate ground truth. Third, we were unable to compare our results directly with TotalSegmentator because our ground-truth labels include the intrahepatic segments of the inferior vena cava and the portal vein, which TotalSegmentator delineates as separate structures. Finally, although our test set contained a range of primary and metastatic lesions, sample sizes for certain tumor subtypes were relatively small, which may limit the generalizability of our findings across all disease presentations.

Conclusion

Both the SwinUNETR and residual UNET models achieved excellent accuracy for liver segmentation and high performance for hepatic tumor segmentation on ^{18}F-FDG PET/CT, with most volumetric measurements falling within clinically acceptable limits. While SwinUNETR demonstrated slightly superior performance, both architectures showed potential for integration into clinical workflows and research pipelines. Given their open-source availability and adaptability, these models could support automated, reproducible segmentation in treatment planning and quantitative imaging.

Ethics

Ethics Committee Approval: The study was approved by the Ethics Committee of Harran University (approval no: HRÜ-25.11.02, date: 16.06.2025), with additional approval from the institutional review board.

Informed Consent: Written informed consent was obtained from all patients before imaging.

Footnotes

Authorship Contributions

Surgical and Medical Practices: B.D., Concept: B.D., Design: B.D., Data Collection or Processing: B.D., H.K.Y., F.E., M.A.A., Analysis or Interpretation: B.D., H.K.Y., F.E., M.A.A., Literature Search: B.D., Writing: B.D.

Conflict of Interest: No conflict of interest was declared by the authors.

Financial Disclosure: The authors declared that this study has received no financial support.

References

1. Sung H, Ferlay J, Siegel RL, Laversanne M, Soerjomataram I, Jemal A, Bray F. Global Cancer Statistics 2020: GLOBOCAN estimates of ıncidence and mortality worldwide for 36 cancers in 185 countries. CA Cancer J Clin. 2021;71:209-249.
2. Ntanasis-Stathopoulos I, Liatsou E, Dedes N, Triantafyllakis K, Tsilimigras DI, Gavriatopoulou M. Multidisciplinary management of colorectal liver metastases. In: Interdisciplinary cancer research. Springer Nature; 2024.
3. Van Cutsem E, Cervantes A, Adam R, Sobrero A, Van Krieken JH, Aderka D, Aranda Aguilar E, Bardelli A, Benson A, Bodoky G, Ciardiello F, D'Hoore A, Diaz-Rubio E, Douillard JY, Ducreux M, Falcone A, Grothey A, Gruenberger T, Haustermans K, Heinemann V, Hoff P, Köhne CH, Labianca R, Laurent-Puig P, Ma B, Maughan T, Muro K, Normanno N, Österlund P, Oyen WJ, Papamichael D, Pentheroudakis G, Pfeiffer P, Price TJ, Punt C, Ricke J, Roth A, Salazar R, Scheithauer W, Schmoll HJ, Tabernero J, Taïeb J, Tejpar S, Wasan H, Yoshino T, Zaanan A, Arnold D. ESMO consensus guidelines for the management of patients with metastatic colorectal cancer. Ann Oncol. 2016;27:1386-1422.
4. Clark AM, Ma B, Taylor DL, Griffith L, Wells A. Liver metastases: microenvironments and ex-vivo models. Exp Biol Med (Maywood). 2016;241:1639-1652.
5. Weber M, Lam M, Chiesa C, Konijnenberg M, Cremonesi M, Flamen P, Gnesin S, Bodei L, Kracmerova T, Luster M, Garin E, Herrmann K. EANM procedure guideline for the treatment of liver cancer and liver metastases with intra-arterial radioactive compounds. Eur J Nucl Med Mol Imaging. 2022;49:1682-1699.
6. Chiesa C, Sjogreen-Gleisner K, Walrand S, Strigari L, Flux G, Gear J, Stokke C, Gabina PM, Bernhardt P, Konijnenberg M. EANM dosimetry committee series on standard operational procedures: a unified methodology for ^{99m}Tc-MAA pre- and 90Y peri-therapy dosimetry in liver radioembolization with 90Y microspheres. EJNMMI Phys. 2021;8:77.
7. Dawson LA, Ten Haken RK. Partial volume tolerance of the liver to radiation. Semin Radiat Oncol. 2005;15:279-283.
8. Hwang SH, Hong HS, Kim D, Kim GM, Lee HW, Lee M, Kim DY, Park MA, Yun M. Total lesion glycolysis on 18F-FDG PET/CT is a better prognostic factor than tumor dose on 90Y PET/CT in patients with hepatocellular carcinoma treated with 90Y transarterial radioembolization. Clin Nucl Med. 2022;47:e437-e443.
9. Demir B, Soydal C, Kucuk NO, Celebioglu EC, Bilgic MS, Kuru Oz D, Elhan AH, Kir KM. Voxel-based dosimetry with integrated Y-90 PET/MRI and prediction of response of primary and metastatic liver tumors to radioembolization with Y-90 glass microspheres. Ann Nucl Med. 2025;39:31-46.
10. Hatamizadeh A, Nath V, Tang Y, Yang D, Roth HR, Xu D. Swin UNETR: Swin transformers for semantic segmentation of brain tumors in MRI images. Arxiv. 2022.
11. He Y, Nath V, Yang D, Tang Y, Myronenko A, Xu D. SwinUNETR-V2: stronger swin transformers with stagewise convolutions for 3D medical image segmentation. Lecture Notes in Computer Science. 2023.
12. Kerfoot E, Clough J, Oksuz I, Lee J, King AP, Schnabel JA. Left-ventricle quantification using residual U-Net. Lecture Notes in Computer Science. 2019.
13. Wasserthal J, Breit HC, Meyer MT, Pradella M, Hinck D, Sauter AW, Heye T, Boll DT, Cyriac J, Yang S, Bach M, Segeroth M. TotalSegmentator: robust segmentation of 104 anatomic structures in CT images. Radiol Artif Intell. 2023;5:e230024.
14. Yashaswini GN, Manjunath RV, Shubha B, Prabha P, Aishwarya N, Manu HM. Deep learning technique for automatic liver and liver tumor segmentation in CT images. Journal of Liver Transplantation. 2025;17:100251.
15. Li X, Chen H, Qi X, Dou Q, Fu CW, Heng PA. H-DenseUNet: hybrid densely connected UNet for liver and tumor segmentation from CT volumes. IEEE Trans Med Imaging. 2018;37:2663-2674.
16. Ghofrani F, Behnam H, Motlagh HDK. Liver segmentation in CT images using deep neural networks. 2020 28th Iranian Conference on Electrical Engineering, ICEE. 2020.
17. Demir B, Soydal C, Kucuk NO, Celebioglu EC, Bilgic MS, Kuru Oz D, Elhan AH, Kir KM. Voxel-based dosimetry with integrated Y-90 PET/MRI and prediction of response of primary and metastatic liver tumors to radioembolization with Y-90 glass microspheres. Ann Nucl Med. 2025;39:31-46.

18. 4burakfe/SlicerAether: This extension allows users to utilize SwinUNETR and UNET models to segment multimodality images. Available from: https://github.com/4burakfe/SlicerAether/tree/main
19. Claritas/Segmentation Edition at main · 4burakfe/Claritas. Available from: https://github.com/4burakfe/Claritas/tree/main/Segmentation%20 Edition
20. Release Sample Cases · 4burakfe/SlicerAether. Available from: https://github.com/4burakfe/SlicerAether/releases/tag/Sample_Cases
21. Fedorov A, Beichel R, Kalpathy-Cramer J, Finet J, Fillion-Robin JC, Pujol S, Bauer C, Jennings D, Fennessy F, Sonka M, Buatti J, Aylward S, Miller JV, Pieper S, Kikinis R. 3D slicer as an image computing platform for the quantitative ımaging network. Magn Reson Imaging. 2012;30:1323-1341.
22. 3D Slicer image computing platform | 3D Slicer. Available from: https://www.slicer.org/
23. Liu Z, Lin Y, Cao Y, Hu H, Wei Y, Zhang Z, Lin S, Guo B. Swin transformer: hierarchical vision transformer using shifted windows. IEEE/CVF International Conference on Computer Vision (ICCV). 2021.
24. Wang Z, Popordanoska T, Bertels J, Lemmens R, Blaschko MB. Dice semimetric losses: optimizing the dice score with soft labels. lecture notes in computer science. 2023.
25. Wang Z, Ning X, Blaschko MB. Jaccard metric losses: optimizing the jaccard ındex with soft labels. Adv Neural Inf Process Syst. 2023.
26. Milletari F, Navab N, Ahmadi SA. V-Net: Fully convolutional neural networks for volumetric medical image segmentation. 2016 Fourth International Conference on 3D Vision IEEE. 2016.
27. Goedhart J, Rishniw M. BA-plotteR - A web tool for generating Bland-Altman plots and constructing limits of agreement. Res Vet Sci. 2021;137:281-286.
28. R Core Team. R: A Language and environment for statistical computing. Foundation for Statistical Computing. 2022.
29. Heimann T, Van Ginneken B, Styner MA, Arzhaeva Y, Aurich V, Bauer C, Beck A, Becker C, Beichel R, Bekes G, Bello F de, Binnig G, Bischof H, Bornik A, Cashman PM, Chi Y, Cordova A, Dawant BM, Fidrich M, Furst JD, Furukawa D, Grenacher L, Hornegger J, Kainmuller D, Kitney RI, Kobatake H, Lamecker H, Lange T, Lee J, Lennon B, Li R, Li S, Meinzer HP, Nemeth G, Raicu DS, Rau AM, Rikxoort EM van, RoussonM, Rusko L, Saddi KA, Schmidt G, Seghers D, Shimizu A, Slagmolen P, Sorantin E, Soza G, Susomboon R, Waite JM, Wimmer A, Wolf I. Comparison and evaluation of methods for liver segmentation from CT datasets. IEEE Trans Med Imaging. 2009;28:1251-1265.
30. Meng L, Tian Y, Bu S. Liver tumor segmentation based on 3D convolutional neural network with dual scale. J Appl Clin Med Phys. 2020;21:144-157.
31. Christ PF, Elshaer MEA, Ettlinger F, Tatavarty S, Bickel M, Bilic P, Rempfler M, Armbruster M, Hofmann F, D'Anastasi M, Sommer WH, Ahmadi SA, Menze BH. Automatic liver and lesion segmentation in CT using cascaded fully convolutional neural networks and 3D conditional random fields. Lecture Notes in Computer Science. 2016.
32. Leung KH, Rowe SP, Sadaghiani MS, Leal JP, Mena E, Choyke PL, Du Y, Pomper MG. Deep semisupervised transfer learning for fully automated whole-body tumor quantification and prognosis of cancer on PET/CT. J Nucl Med. 2024;65:643-650.
33. Luo Y, Yang Q, Hu J, Qin X, Jiang S, Liu Y. Preliminary study on detection and diagnosis of focal liver lesions based on a deep learning model using multimodal PET/CT images. Eur J Radiol Open. 2024;14:100624.

Original Article

Mol Imaging Radionucl Ther 2026;35(1):19-27 ***DOI:****10.4274/mirt.galenos.2025.19052*

The Prognostic Significance of Preoperative Staging ^{18}F-FDG PET/MRI Findings in Gastric Cancer Patients Undergoing Gastrectomy

Gastrektomi Yapılan Mide Kanseri Hastalarında Preoperatif Evreleme ^{18}F-FDG PET/MRG Bulgularının Prognostik Önemi

Seda Gülbahar Ateş, Uğuray Aydos, Ramazan Kalkan, Ümit Özgür Akdemir, Lütfiye Özlem Atay

Gazi University Faculty of Medicine, Department of Nuclear Medicine, Ankara, Türkiye

Abstract

Objective: The aim of this retrospective study was to investigate the prognostic value of preoperative findings on ^{18}F-fluorodeoxyglucose positron emission tomography/magnetic resonance imaging (^{18}F-FDG PET/MRI) in gastric cancer (GC) patients who underwent total or subtotal gastrectomy.

Methods: Patients with GC who underwent pretreatment staging with ^{18}F-FDG PET/MRI and subsequently underwent total or subtotal gastrectomy were included in the study. Demographic and clinicopathologic features of patients were recorded. The maximum wall thickness of gastric tumors, the minimum apparent diffusion coefficient (ADC_{min}), the total number and maximum standard uptake values (SUV_{max}) of ^{18}F-FDG-positive lymph nodes, the short-axis diameter of the largest lymph node, and the tumor SUV_{max}-to-liver SUV_{mean} ratio on ^{18}F-FDG PET/MRI were recorded. Predictors of mortality were evaluated using Cox proportional hazards regression models. Survival analysis was conducted using the Kaplan-Meier method.

Results: Seventy-eight patients with GC who underwent gastrectomy were included in the study. The median follow-up duration was 23.9 months (interquartile range: 33.4); 39 patients (50.0%) died during follow-up. In the multivariate analysis, the tumor SUV_{max}/liver SUV_{mean} ratio ($p=0.002$) and tumor histopathologic group ($p<0.001$) were identified as independent predictors of overall survival. The mean overall survival was 42.7 months [95% confidence interval (CI): 35.8-49.6]. The mean overall survival in the signet-ring cell carcinoma/other subtypes group (31.4 months; 95% CI: 22.3-40.4) was significantly shorter than that in the adenocarcinoma group (49.2 months; 95% CI: 40.3-58.2) ($p=0.019$). Patients with a tumor SUV_{max}/liver SUV_{mean} ratio greater than 2.6 on ^{18}F-FDG PET/MRI (35.7 months; 95% CI: 27.6-43.7) had a shorter overall survival than those with a ratio lower than 2.6 (57.1 months; 95% CI: 46.5-67.7) ($p=0.005$).

Conclusion: The tumor SUV_{max}-to-liver SUV_{mean} ratio may serve as a robust imaging biomarker for prognosis and for determining histopathologic subtype in GC patients who underwent total or subtotal gastrectomy.

Keywords: Gastric cancer, ^{18}F-FDG PET/MRI, prognosis, overall survival

Öz

Amaç: Bu retrospektif çalışmanın amacı, total veya subtotal gastrektomi uygulanan mide kanseri (GC) tanılı hastalarda preoperatif ^{18}F-florodeoksiglukoz pozitron emisyon tomografisi/manyetik rezonans görüntüleme (^{18}F-FDG PET/MRG) bulgularının prognostik değerini araştırmaktır.

Address for Correspondence: Seda Gülbahar Ateş, Gazi University Faculty of Medicine, Department of Nuclear Medicine, Ankara, Türkiye
E-mail: sdsdglbhr@gmail.com **ORCID ID:** orcid.org/0000-0003-0422-0863

Received: 04.07.2025 **Accepted:** 26.10.2025 **Epub:** 28.11.2025 **Publication Date:** 03.02.2026

Cite this article as: Gülbahar Ateş Seda, Aydos U, Kalkan R, Akdemir ÜÖ, Atay LÖ. The prognostic significance of preoperative staging ^{18}F-FDG PET/MRI findings in gastric cancer patients undergoing gastrectomy. Mol Imaging Radionucl Ther. 2026;35(1):19-27.

Yöntem: Tedavi öncesi evreleme amacıyla ^{18}F-FDG PET/MRG çekilmiş ve ardından total veya subtotal gastrektomi uygulanmış GC tanılı hastalar çalışmaya dahil edilmiştir. Hastaların demografik ve klinikopatolojik özellikleri kaydedilmiştir. ^{18}F-FDG PET/MRG görüntülemesinde mide tümörlerinin maksimum duvar kalınlığı, minimum görünen difüzyon katsayısı (ADC$_{min}$) değeri, ^{18}F-FDG pozitif lenf nodu sayısı ve bu lenf nodlarının maksimum standart tutulum değeri (SUV$_{maks}$) değeri, en büyük lenf nodunun kısa eksen çapı ve tümör SUV$_{maks}$/karaciğer SUV$_{ortalama}$ oranı değerlendirilmiştir. Mortaliteyi ön gören faktörleri belirlemek amacıyla Cox regresyon analizi yapılmıştır. Sağkalım analizi Kaplan-Meier yöntemiyle değerlendirilmiştir.

Bulgular: Çalışmaya gastrektomi uygulanmış 78 hasta dahil edildi. Medyan takip süresi 23,9 (çeyrekler açıklığı: 33,4) ay olarak hesaplandı ve takip sürecinde 39 (%50,0) hastada mortalite izlendi. Çok değişkenli analizde tümör SUV$_{maks}$/karaciğer SUV$_{ortalama}$ oranı (p=0,002) ve tümörün histopatolojik grubu (p<0,001) genel sağkalımın bağımsız belirleyicileri olarak saptandı. Ortalama genel sağkalım 42,7 ay [%95 güven aralığı (GA): 35,8-49,6] idi. Taşlı yüzük hücreli karsinom/diğer alt tipler grubunda ortanca sağkalım süresi (31,4 ay, %95 GA: 22,3-40,4), adenokarsinom grubuna kıyasla (49,2 ay, %95 GA: 40,3-58,2) anlamlı derecede daha kısaydı (p=0,019).^{18}F-FDG PET/MRG'de tümör SUV$_{maks}$/karaciğer SUV$_{ortalama}$ oranı 2,6'dan yüksek olan hastalarda sağkalım (35,7 ay, %95 GA: 27,6-43,7), bu oranın 2,6'dan düşük olduğu hastalara kıyasla daha kısa bulundu (57,1 ay, %95 GA: 46,5-67,7) (p=0,005).

Sonuç: Total veya subtotal gastrektomi uygulanmış GC hastalarında tümör SUV$_{maks}$/karaciğer SUV$_{ortalama}$ oranı, histopatolojik alt tip ile birlikte, prognostik bir görüntüleme biyobelirteci olarak öne çıkmaktadır.

Anahtar Kelimeler: Mide kanseri, ^{18}F-FDG PET/MRG, prognoz, genel sağkalım

Introduction

Gastric cancer (GC) is the fifth most common cancer worldwide in both incidence and cancer-related mortality (1). It is a global health problem characterized by various risk factors, aggressive clinical behavior, and typically late-stage diagnosis. GC is a heterogeneous disease comprising multiple histopathologic subtypes and molecular features (2).

The appropriate management of GC patients is based on accurate staging. Computed tomography (CT) is the gold-standard imaging modality for staging GC. Moreover, in current clinical practice, when endoscopic ultrasound is performed to evaluate early-stage non-metastatic disease, especially in candidates for endoscopic resection, diagnostic laparoscopy can be used to identify radiologically occult peritoneal disease. ^{18}F-fluorodeoxyglucose (^{18}F-FDG) positron emission tomography (PET) is increasingly used for staging GC to assess lymph node involvement and distant metastases, despite ongoing debate about its routine use in GC (2,3,4). It can provide various image-derived semiquantitative parameters, including maximum standardized uptake value (SUV$_{max}$), and qualitative diagnostic data. ^{18}F-FDG PET/CT has been shown to change treatment management in 3%-29% of GC patients (5). The use of these modalities improves staging accuracy and thus therapeutic management of GC.

The standard treatment for GC is surgery, with the primary goal of complete resection with negative margins (3). However, locoregional recurrence and cancer-related mortality can occur even after a curative surgical approach (6,7,8,9). Therefore, in the era of personalized medicine, predicting prognosis in GC patients who have undergone curative surgery may alter therapeutic management and ultimately improve patient outcomes. The prognostic significance of ^{18}F-FDG PET/CT parameters in GC has been investigated in various studies, although most included heterogeneous patient populations with respect to therapeutic approach (10,11). A limited number of studies have focused specifically on operated GC. Moreover, to the best of our knowledge, despite a few studies on ^{18}F-FDG PET/ PET/magnetic resonance imaging (MRI) in GC patients (12,13,14,15), no study has evaluated its prognostic value in this population. The MRI component of PET/MRI may enhance the prognostic value of ^{18}F-FDG PET in GC patients by providing functional information and superior soft-tissue contrast. Accordingly, the aim of the present study was to evaluate the prognostic value of preoperative ^{18}F-FDG PET/MRI staging findings in GC patients who underwent total or subtotal gastrectomy.

Material and Methods

Patient Population

This retrospective study was approved by Gazi University President's Office Ethics Commission (number: 2025-1103, date: 17.06.2025). The requirement for informed consent was waived. Patients with GC who underwent pretreatment staging with ^{18}F-FDG PET/MRI and subsequently underwent total or subtotal gastrectomy between 2018 and 2024 were included in the present study. Patients who had distant metastases on ^{18}F-FDG PET/MRI or a second primary malignancy were excluded from the study.

Clinicopathologic Features

Demographic and clinicopathologic features of patients were assessed using the hospital information system. Patients' ages, gender, and body mass index; history of chemotherapy and radiotherapy; type of gastrectomy (proximal, distal, or total); and extent of lymph node dissection (D1 or D1+, D2 or D2+) were recorded. Tumor histopathologic subtype and Lauren classification, the location and diameter of primary gastric tumors, the total number of dissected lymph nodes and the number of metastatic lymph nodes, the diameter of the largest metastatic lymph node, and pathological T (pT) and N (pN) stages according to the 8th tumor–node–metastasis (TNM) staging system were obtained from the pathology reports. The status of human epidermal growth factor receptor 2 (HER_2/neu), the presence of lymphovascular and perineural invasion, and the positivity of surgical margins and peritoneal lavage fluid were recorded. Patients' follow-up was determined from medical records and continued until death, loss to follow-up, or the last documented medical visit. Follow-up duration and overall survival were calculated from the date of PET/MRI acquisition until the date of death or last clinical follow-up.

PET/MRI Acquisition

^{18}F-FDG PET/MRI images were acquired on an integrated 3-T PET/MRI scanner (GE Signa PET/MRI, GE Healthcare, Waukesha, Wisconsin, USA) equipped with a time-of-flight (TOF) PET detector in our department. Patients fasted for at least 4 hours before ^{18}F-FDG PET/MRI. The serum glucose levels measured at the time of ^{18}F-FDG injection were less than 200 mg/dL. ^{18}F-FDG was intravenously administered at a dose of 1.85 MBq/kg body weight. Whole-body ^{18}F-FDG PET/MRI was performed from the vertex of the skull to the upper thigh 60 min after the ^{18}F-FDG injection. ^{18}F-FDG PET/MRI acquisition included axial T1-weighted and coronal T2-weighted MRI sequences, axial diffusion-weighted imaging (DWI) (DWI; b-values of 50 and 800 s/mm^2), and apparent diffusion coefficient (ADC) images, acquired with five or six bed positions. PET scans were obtained using MRI sequences, and the acquisition time per bed position was 4 minutes. The other construction parameters were: the ordered subsets expectation maximization algorithm with TOF technique; field of view= 60 cm × 60 cm; matrix= 256 × 256; filter cut-off= 5.0 mm; subsets= 28; iterations= 2. Attenuation correction was performed by the Dixon-based segmentation method.

Image Analysis

PET images were evaluated using GE Healthcare Volume Share 5 software (Advantage Workstation 4.6, Buc, France). ^{18}F-FDG PET/MRI scans were evaluated simultaneously by two nuclear medicine physicians, who reached consensus. The maximum wall thickness of primary gastric tumors was measured on T1W MRI, and the SUV_{max} of primary gastric tumors was recorded. The minimum ADC (ADC_{min}) values of primary gastric tumors were measured on ADC images. Lymph nodes demonstrating higher ^{18}F-FDG uptake than background activity were considered positive. The total number of ^{18}F-FDG-positive lymph nodes, the SUV_{max} of ^{18}F-FDG-positive lymph nodes, and the short-axis diameter of the largest lymph node were recorded. The SUV_{mean} of the liver was calculated using a spherical region of interest with a 3-cm diameter placed within normal parenchyma of the right hepatic lobe. The ratios of primary tumor SUV_{max} to liver SUV_{mean}, lymph node SUV_{max} to tumor SUV_{max}, and lymph node SUV_{max} to liver SUV_{mean} were calculated.

Statistical Analysis

Statistical analyses were conducted using the SPSS software version 27. The distributions of the variables were assessed using visual methods (histograms and probability plots) and analytical methods (Kolmogorov-Smirnov and Shapiro-Wilk tests). Descriptive statistics were presented as frequencies for ordinal/nominal variables, medians and interquartile ranges (IQRs) for non-normally distributed variables, and mean ± standard deviation for normally distributed variables. The Mann-Whitney U test and the Kruskal-Wallis test were used to compare the histopathological groups and ^{18}F-FDG PET/MRI findings. Optimal cut-off values for continuous variables were determined using the Youden index (sensitivity + specificity - 1) obtained from ROC curve analyses. Cox regression analyses were performed to identify predictors of mortality using univariate and multivariate models with backward selection. A sensitivity analysis was also performed to assess the robustness of the results after excluding rare non-adenocarcinoma pathologies from the signet ring cell carcinoma group. Survival analysis was performed using the Kaplan-Meier method. An overall Type I error rate of 5% was used to determine statistical significance.

Results

A total of 78 patients with GC who underwent gastrectomy were included in the present study. The clinicopathological characteristics of the patients are summarized in Table 1. The mean age of the patients was 65.4±13.9 years; 47 (60.3%) were male. Of the 78 patients, 46 (59.0%) were assigned to the adenocarcinoma group, including 28 with well- to moderately differentiated adenocarcinoma, 15 with poorly differentiated adenocarcinoma, and 3 with adenocarcinoma of undefined subtype. The remaining 32 patients (41.0%) were included in the signet-ring cell carcinoma and other subtypes group, comprising 28 patients with signet-ring cell carcinoma and 4 patients with rare non-adenocarcinoma pathologies (2 with lymphoepithelioma-like carcinomas, 1 with mixed adenoneuroendocrine carcinoma, and 1 with large-cell neuroendocrine carcinoma).

Table 1. The patients' clinicopathologic characteristics

Clinicopathologic features		Mean ± standard deviation median (interquartile range), n (%)
Age		65.4±13.9
Gender	Male	47 (60.3%)
	Female	31 (39.7%)
Body mass index		26.2±4.6
Type of gastrectomy	Proximal gastrectomy	14 (17.9%)
	Distal gastrectomy	27 (34.6%)
	Total gastrectomy	37 (47.4%)
Lymph node dissection	D1 and D1+ dissection	4 (5.1%)
	D2 and D2+ dissection	74 (94.9%)
Tumor histopathologic group	Adenocarcinoma group	46 (59%)
	Signet ring cell carcinoma/other subtypes group	32 (41%)
Location primary gastric tumor	Cardia	14 (17.9%)
	Corpus	21 (26.9%)
	Antrum	26 (33.3%)
	More than one region	17 (21.8%)
pT stage (n=69)	pT1-2	12 (17.4%)
	pT3	23 (33.3%)
	pT4	34 (49.3%)
pN stage (n=78)	pN0	22 (28.2%)
	pN1-2	26 (33.2%)
	pN3	30 (38.5%)
Diameter of primary gastric tumors (cm)		5.0 (3.8)
The total number of dissected lymph nodes		26.4±12.0
The total number of metastatic lymph nodes		4.0 (10.0)
The diameter of the largest metastatic lymph node (cm) (n=16)		2.2±0.9
Lauren classification (n=53)	Intestinal type	24 (45.3%)
	Diffuse/signet ring cell carcinoma type	26 (49.1%)
	Other pathologies	3 (5.7%)
Her$_2$neu (n=68)	Positive	9 (13.2%)
	Negative	59 (86.8%)
Lymphovascular invasion (n=62)	Positive	17 (27.4%)
	Negative	45 (72.6%)
Perineural invasion (n=57)	Positive	18 (31.6%)
	Negative	39 (68.4%)
The positivity of surgical margins (n=73)	Positive	12 (16.4%)
	Negative	61 (83.6%)
The positivity of peritoneal lavage fluid (n=35)	Positive	6 (17.1%)
	Negative	29 (82.9%)
The history of chemotherapy	None	21 (26.9%)
	Pre-operative neoadjuvant chemotherapy	28 (35.9%)
	Post-operative adjuvant chemotherapy	29 (37.2%)
The history of post-operative radiotherapy		13 (16.7%)
Mortality	Positive	39 (50.0%)
	Negative	39 (50.0%)
Follow-up duration (months)		23.9 (33.4)

Table 2. The findings of ^{18}F-FDG PET/MRI

Features	Median (interquartile range)			p value
	All patients (n=78)	Adenocarcinoma group	Signet ring cell carcinoma/ other subtypes group	
The maximum wall thickness of primary tumors (mm)	19.0 (14.5)	21.9 (13.1)	17.4 (11.3)	p=0.044
Tumor SUV_{max}	10.2 (12.3)	16.4 (13.9)	6.6 (6.6)	p<0.001
Tumor ADC_{min} ($x10^{-6}mm^2/sec$)	778.0 (282.0)	755.0 (292.0)	876.0 (318.0)	p=0.105
Total number of ^{18}F-FDG positive lymph nodes	0 (5.0)	1.0 (5.0)	0 (5.0)	p=0.332
Lymph node SUV_{max}	6.3 (6.2)	6.8 (5.3)	4.7 (5.7)	p=0.136
The short axis diameter of the largest lymph node (mm)	7.1 (7.8)	8.4 (8.0)	6.4 (6.1)	p=0.025
Tumor SUV_{max}/liver SUV_{mean} ratio	4.3 (4.9)	6.0 (6.2)	2.9 (3.3)	p<0.001
Lymph node SUV_{max}/tumor SUV_{max} ratio	0.47 (0.34)	0.46 (0.33)	0.48 (0.32)	p=0.332
Lymph node SUV_{max}/liver SUV_{mean} ratio	2.6 (2.5)	2.9 (2.7)	2.4 (2.4)	p=0.569

SUV_{max}: Maximum standardized uptake value, ADC_{min}: Minimum apparent diffusion coefficient, SUV_{mean}: Mean standardized uptake value, ^{18}F-FDG PET/MRI: ^{18}F-fluorodeoxyglucose positron emission tomography/magnetic resonance imaging

The numbers of patients who underwent proximal, distal, and total gastrectomy were 14 (17.9%), 27 (34.6%), and 37 (47.4%), respectively. Furthermore, most patients (94.9%) underwent D2 or D2+ lymph node dissection (Table 1).

The findings from ^{18}F-FDG PET/MRI are shown in Table 2. The maximum wall thickness of primary tumors (p=0.044), tumor SUV_{max} (p<0.001), the ratio of tumor SUV_{max} to liver SUV_{mean} (p<0.001), and the short-axis diameter of the largest lymph node (p=0.025) were significantly higher in the adenocarcinoma group compared with the signet-ring cell carcinoma and other subtypes group (Table 2).

The median follow-up duration was 23.9 (IQR: 33.4) months and 39 (50.0%) patients died during the follow-up. The results of univariate and multivariate analyses for predicting overall survival in GC patients who underwent gastrectomy are shown in Table 3. In the univariate analysis, the type of gastrectomy (p=0.002), tumor histopathologic group (p=0.021), pT stage (p=0.025), pN stage (p=0.004), the presence of lymphovascular (p=0.013) and perineural (p=0.017) invasion, tumor ADC_{min} (p=0.023), the maximum wall thickness of primary tumors (p=0.031), the total number of ^{18}F-FDG positive lymph nodes (p=0.027), the short axis diameter of the largest lymph node (p=0.007), and the tumor SUV_{max}/liver SUV_{mean} ratio (p=0.008) were significantly associated with mortality in GC patients who underwent total or subtotal gastrectomy (Table 3). However, no statistically significant differences were found between mortality and other clinicopathological features presented in Table 1 or PET/MRI findings presented in Table 2 (all p>0.05).

In the multivariate analysis, the tumor SUV_{max}-to-liver SUV_{mean} ratio on pre-treatment ^{18}F-FDG PET/MRI (p=0.002) and the tumor histopathologic group (p<0.001) were identified as independent predictors of overall survival in GC patients who underwent total or subtotal gastrectomy (Table 3). A tumor SUV_{max}/liver SUV_{mean} ratio greater than 2.6 on staging ^{18}F-FDG PET/MRI was significantly associated with an approximately 4.4-fold increased risk of mortality during follow-up among GC patients who underwent total or subtotal gastrectomy. Additionally, the signet ring cell carcinoma/other subtypes group was associated with an approximately 5.9-fold higher risk of mortality during follow-up within the same patient cohort.

In a sensitivity analysis excluding four rare non-adenocarcinoma pathologies (two with lymphoepithelioma-like carcinoma, one with mixed adenoneuroendocrine carcinoma, and one with large-cell neuroendocrine carcinoma) from the signet ring cell carcinoma group, the same independent predictors, the tumor histopathologic group [p<0.001, odds ratio (OR): 5.42, 95% confidence interval (CI): 2.14-13.75] and the tumor SUV_{max}-to-SUV_{mean} ratio (p<0.001, OR: 7.18, 95% CI: 2.27-22.69), remained statistically significant in the multivariate analysis. These findings confirm that the Cox regression model remained robust after exclusion of rare non-adenocarcinoma pathologies.

Table 3. The results of univariate and multivariate analyses for predicting overall survival in gastric cancer patients

Univariate analysis			
	OR	**95% CI**	**p value**
Type of gastrectomy (proximal, distal, total) (ref. proximal)			0.002
Type of gastrectomy (1)	1.128	0.339-3.753	0.844
Type of gastrectomy (2)	3.812	1.327-10.948	0.013
Tumor histopathologic type (ref. adenocarcinoma group)	2.097	1.116-3.941	**0.021**
pT stage (ref. pT1-2)			**0.025**
pT stage (1)	2.777	0.599-12.863	0.192
pT stage (2)	5.585	1.309-23.829	0.020
pN stage (ref. pN0)			**0.004**
pN stage (1)	3.654	1.185-11.271	0.024
pN stage (2)	5.974	2.028-17.597	0.001
Lymphovascular invasion (ref. negative)	4.542	1.382-14.931	**0.013**
Perineural invasion (ref. negative)	3.622	1.253-10.471	**0.017**
Tumor ADC_{min} (≤94, >94) (ref. ≤94)	0.365	0.153-0.873	**0.023**
The maximum wall thickness of primary tumors (≤13.6,>13.6 mm) (ref. ≤13.6)	2.622	1.092-6.300	**0.031**
Total number of ^{18}F-FDG positive lymph nodes (4, >4) (ref. ≤4)	2.058	1.087-3.897	**0.027**
The short axis diameter of the largest lymph node (≤8.7, >8.7 mm) (ref. ≤8.7)	2.435	1.281-4.627	**0.007**
Tumor SUV_{max}/liver SUV_{mean} ratio (≤2.6, >2.6) (ref. ≤2.6)	3.256	1.355-7.826	**0.008**
Multivariate analysis (backward-wald method)			
	OR	**95% CI**	**p value**
Tumor SUV_{max}/liver SUV_{mean} ratio (≤2.6, >2.6) (ref. ≤2.6)	4.361	1.256-15.147	**0.020**
Tumor histopathologic type (ref. adenocarcinoma group)	5.859	2.229-15.397	**<0.001**

*Statistically significant parameters were shown in the table.
Ref: Reference category, SUV_{max}: Maximum standardized uptake value, ADC_{min}: Minimum apparent diffusion coefficient, SUV_{mean}: Mean standardized uptake value, OR: Odds ratio, CI: Confidence interval, ^{18}F-FDG: ^{18}F-fluorodeoxyglucose

Mean and median overall survival were 42.7 months (95% CI: 35.8-49.6) and 37.4 months (95% CI: 9.04-65.87), respectively, among GC patients who underwent total or subtotal gastrectomy. The estimated overall survival rates at 12, 24, and 36 months were 77.5%, 53.5%, and 48.5%, respectively. During the follow-up period, The median overall survival was not reached in the adenocarcinoma group and in patients with a tumor SUV_{max}/liver SUV_{mean} ratio lower than 2.6. Therefore, mean overall survival times were reported. The mean overall survival in the signet-ring cell carcinoma/other subtypes group (31.4 months, 95% CI: 22.3-40.4) was significantly shorter than that in the adenocarcinoma group (49.2 months, 95% CI: 40.3-58.2) (p=0.019, Figure 1A). Moreover, the patients with a tumor SUV_{max}/liver SUV_{mean} ratio greater than 2.6 (35.7 months, 95% CI: 27.6-43.7) on staging ^{18}F-FDG PET/MRI had a shorter overall survival than those with a ratio lower than 2.6 (57.1 months, 95% CI: 46.5-67.7) (p=0.005, Figure 1B).

Discussion

In the era of precision medicine, stratifying oncology patients based on survival outcomes may alter treatment approaches and ultimately improve patient management. Therefore, identifying prognostic biomarkers plays a pivotal role in the transition to individualized treatment in oncology. Therefore, ^{18}F-FDG PET/MRI is a unique modality that can provide multiparametric imaging biomarkers in different malignancies. In this study investigating the prognostic value of pretreatment ^{18}F-FDG PET/MRI in GC patients who underwent total or subtotal gastrectomy, the tumor SUV_{max}-to-liver SUV_{mean} ratio and the tumor histopathologic group were found to be independent predictors of overall survival. Although the tumor ADC_{min} on pretreatment ^{18}F-FDG PET/MRI was significantly associated with overall survival in the univariate analysis, it did not remain an independent predictor in the multivariate analysis.

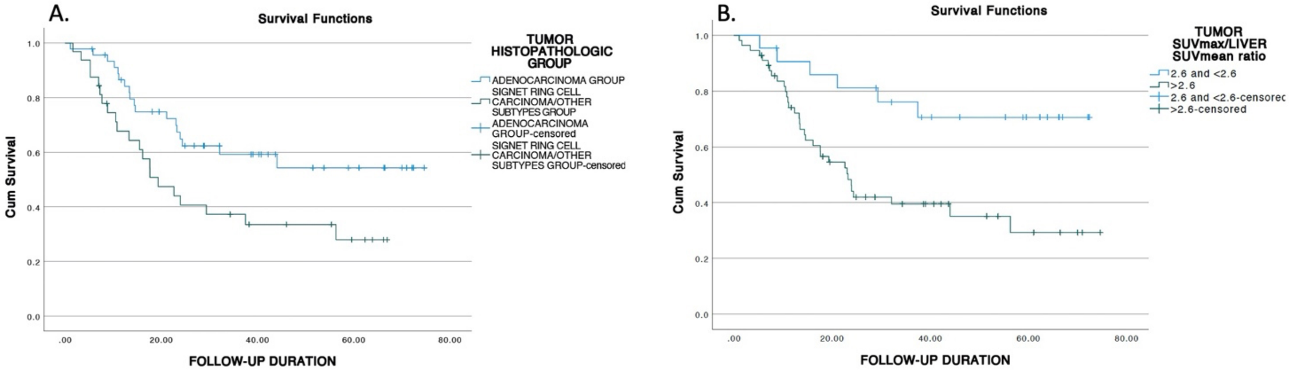

Figure 1. Kaplan-Meier survival analysis according to the tumor histopathologic group (A) and the tumor SUV$_{max}$/liver SUV$_{mean}$ ratio (B)
SUV$_{max}$: Maximum standardized uptake value, SUV$_{mean}$: Mean standardized uptake value

In the present study, the tumor SUV$_{max}$ was not a significant prognostic factor for overall survival in GC patients who underwent total or subtotal gastrectomy. The prognostic value of the semi-quantitative parameters derived from ^{18}F-FDG PET, especially SUV$_{max}$, has been evaluated in GC patients. Contrary to our results, several studies have demonstrated that a higher SUV$_{max}$ on pretreatment ^{18}F-FDG PET was associated with poorer recurrence-free survival and overall survival in GC patients who underwent total or subtotal gastrectomy (16,17,18,19). On the other hand, similar to our study, some studies have reported no significant association between SUV$_{max}$ and prognosis in GC patients who underwent total or subtotal gastrectomy (20,21). Therefore, these discrepancies among the studies could be attributed to differences in patient populations and in the distribution of histopathological subtypes, since histopathological subtypes of GC may exhibit distinct metabolic characteristics and tumor behaviors. In the study investigating the predictive impact of SUV$_{max}$ by histologic subtype, although the primary tumor SUV$_{max}$ was an independent predictor of overall survival in patients with poorly differentiated adenocarcinoma or signet-ring cell GC, it was not significant in patients with well- to moderately differentiated adenocarcinoma (22). Thus, the prognostic value of the tumor SUV$_{max}$ may be influenced by the histopathologic subtypes in GC patients, which may account for conflicting results among studies with different patient populations.

In this study, unlike tumor SUV$_{max}$, the tumor SUV$_{max/}$liver SUV$_{mean}$ ratio was identified as an independent predictor of overall survival in GC patients. This ratio represents the normalized glycolytic activity of the primary gastric tumor relative to that of the liver. Since SUV$_{max}$ can be influenced by several parameters, such as acquisition time, blood glucose level, and other physiological or technical factors, a normalized metric of tumor metabolic activity, such as the tumor SUV$_{max}$/liver SUV$_{mean}$ ratio, might provide a more reliable and consistent measurement. However, in contrast to our results, the studies by Kwon et al. (17) and Liu et al. (21) demonstrated no significant relationship between the tumor SUV$_{max}$/liver SUV$_{mean}$ ratio and either overall survival or progression-free survival in advanced GC patients. These inconsistencies among studies may be due to differences in therapeutic approaches, including neoadjuvant therapies, across patient populations. Despite discrepancies among studies, our findings underscore the potential prognostic utility of the tumor SUV$_{max}$/liver SUV$_{mean}$ ratio in GC patients undergoing total or subtotal gastrectomy.

PET/MRI is a promising modality that offers higher soft-tissue contrast, functional imaging, and multiparametric imaging biomarkers (15). The integration of functional MR sequences, such as DWI and ADC images, into the standard PET/MRI protocol may enhance its diagnostic and prognostic capabilities across different malignancies. DWI reflects the mobility of water protons in tissues, while ADC is a quantitative imaging biomarker that measures the mobility of water molecules in tissues. As a result of the higher cellularity and decreased extracellular space in tumors, water diffusion is restricted, and ADC values decrease (23). The potential prognostic role of ADC value in various cancers has been shown in previous studies (24,25,26,27). To the best of our knowledge, no u^{18}F-FDG PET/MRI study has investigated its prognostic value in GC; however, a limited number of studies have examined the prognostic value of ADC and DWI MRI in GC (26,27). The study by Giganti et al. (27) demonstrated that a lower ADC value was an independent predictor of poorer prognosis in GC patients who underwent gastrectomy with or without neoadjuvant chemotherapy. Furthermore, Giganti et al. (26) reported that ADC values were associated with TNM stage and overall survival in GC patients who underwent gastrectomy without neoadjuvant chemotherapy. Since these two studies used DWI-ADC MRI and did not incorporate metabolic data from ^{18}F-FDG PET in their analyses, these results must be compared with our results cautiously. In our study, although the tumor ADC_{min} on pre-treatment ^{18}F-FDG PET/MRI was significantly associated with overall survival in GC patients, it was not found to be an independent predictor in the multivariate analysis. The tumor SUV_{max}/liver SUV_{mean} ratio and tumor histopathologic group may be more robust prognostic biomarkers than ADC_{min} in GC patients.

In the present study, the tumor histopathologic group was identified as an independent predictor of overall survival in GC patients. The overall survival in the signet-ring-cell carcinoma group was significantly lower than in the adenocarcinoma group. Consistent with our results, the relationship between signet ring cell carcinoma and poor prognosis has been demonstrated by several studies (28,29). Recent studies indicate that the prognostic impact of signet ring cell pathology depends on the stage of GC, being favorable in early tumor stages but adverse in advanced tumor stages (28,30,31). In our study, the signet ring cell carcinoma group had a worse prognosis than the adenocarcinoma group among GC patients who underwent gastrectomy, further supporting its prognostic relevance even in early-stage disease. Moreover, consistent with the literature, the histopathologic features, such as the pT stage, pN stage, the presence of lymphovascular and perineural invasion, as well as PET/MRI findings, including the maximum wall thickness of primary tumors, the total number of ^{18}F-FDG-positive lymph nodes, and the short-axis diameter of the largest lymph node, were significantly associated with overall survival in GC patients (19,20,32,33). Nevertheless, the tumor histopathologic group and the tumor SUV_{max}/liver SUV_{mean} ratio on pretreatment ^{18}F-FDG PET/MRI were found to be more robust prognostic factors than other histopathologic features and PET/MRI findings.

Study Limitations

The present study has some limitations. First, this study is retrospective and single-center, with a limited sample size. Due to its retrospective nature, the patient population was heterogeneous with respect to neoadjuvant therapy. Moreover, complete histopathological data were not available for all patients. Therefore, multicenter prospective studies with larger cohorts are needed to validate and expand upon these findings.

Conclusion

The tumor SUV_{max}/liver SUV_{mean} ratio, a normalized metric of tumor metabolic activity relative to liver metabolic activity, may serve as a robust imaging biomarker for prognosis and for histopathologic subtype classification in GC patients who underwent total or subtotal gastrectomy. Furthermore, multiparametric data derived from ^{18}F-FDG PET/MRI may offer a comprehensive approach to prognostic evaluation in GC patients. ^{18}F-FDG PET/MRI may emerge not only as a diagnostic tool but also as a valuable prognostic modality in the management of GC.

Ethics

Ethics Committee Approval: This retrospective study was approved by Gazi University President's Office Ethics Commission (number: 2025-1103, date: 17.06.2025).

Informed Consent: This retrospective study.

Footnotes

Authorship Contributions

Surgical and Medical Practices: S.G.A., U.A., R.K., Ü.Ö.A., L.Ö.A., Concept: S.G.A., U.A., Design: S.G.A., U.A., R.K., Ü.Ö.A., L.Ö.A., Data Collection or Processing: S.G.A., U.A., R.K., Ü.Ö.A., Analysis or Interpretation: S.G.A., U.A., Ü.Ö.A., L.Ö.A., Literature Search: G.A., Writing: S.G.A., U.A., Ü.Ö.A., L.Ö.A.

Conflict of Interest: No conflict of interest was declared by the authors.

Financial Disclosure: The authors declared that this study has received no financial support.

References

1. Sung H, Ferlay J, Siegel RL, Laversanne M, Soerjomataram I, Jemal A, Bray F. Global Cancer Statistics 2020: GLOBOCAN estimates of incidence and mortality worldwide for 36 cancers in 185 countries. CA Cancer J Clin. 2021;71:209-249.
2. Sundar R, Nakayama I, Markar SR, Shitara K, van Laarhoven HWM, Janjigian YY, Smyth EC. Gastric cancer. Lancet. 2025;405:2087-2102.
3. Ajani JA, D'Amico TA, Bentrem DJ, Corvera CU, Das P, Enzinger PC, Enzler T, Gerdes H, Gibson MK, Grierson P, Gupta G, Hofstetter WL, Ilson DH, Jalal S, Kim S, Kleinberg LR, Klempner S, Lacy J, Lee B, Licciardi F, Lloyd S, Ly QP, Matsukuma K, McNamara M, Merkow RP, Miller AM, Mukherjee S, Mulcahy MF, Perry KA, Pimiento JM, Reddi DM, Reznik S, Roses RE, Strong VE, Su S, Uboha N, Wainberg ZA, Willett CG, Woo Y, Yoon HH, McMillian NR, Stein M. Gastric Cancer, Version 2.2025, NCCN clinical practice guidelines in oncology. J Natl Compr Canc Netw. 2025;23: 169-191.

4. Lordick F, Carneiro F, Cascinu S, Fleitas T, Haustermans K, Piessen G, Vogel A, Smyth EC; ESMO Guidelines Committee. Electronic address: clinicalguidelines@esmo.org. Gastric cancer: ESMO Clinical Practice Guideline for diagnosis, treatment and follow-up. Ann Oncol. 2022;33:1005-1020.
5. Foley KG, Coomer W, Coles B, Bradley KM. The impact of baseline ^{18}F-FDG PET-CT on the management and outcome of patients with gastric cancer: a systematic review. Br J Radiol. 2022;95:20220437.
6. Roukos DH, Lorenz M, Karakostas K, Paraschou P, Batsis C, Kappas AM. Pathological serosa and node-based classification accurately predicts gastric cancer recurrence risk and outcome, and determines potential and limitation of a Japanese-style extensive surgery for western patients: a prospective with quality control 10-year follow-up study. Br J Cancer. 2001;84:1602-1609.
7. Schwarz RE, Smith DD. Clinical impact of lymphadenectomy extent in resectable gastric cancer of advanced stage. Ann Surg Oncol. 2007;14:317-328.
8. Schwarz RE, Zagala-Nevarez K. Recurrence patterns after radical gastrectomy for gastric cancer: prognostic factors and implications for postoperative adjuvant therapy. Ann Surg Oncol. 2002;9:394-400.
9. Songun I, Putter H, Kranenbarg EM, Sasako M, van de Velde CJ. Surgical treatment of gastric cancer: 15-year follow-up results of the randomised nationwide Dutch D1D2 trial. Lancet Oncol. 2010;11:439-449.
10. Wu Z, Zhao J, Gao P, Song Y, Sun J, Chen X, Ma B, Wang Z. Prognostic value of pretreatment standardized uptake value of F-18-fluorodeoxyglucose PET in patients with gastric cancer: a meta-analysis. BMC Cancer. 2017;17:275.
11. Tang L, Wang XJ, Baba H, Giganti F. Gastric cancer and image-derived quantitative parameters: part 2-a critical review of DCE-MRI and ^{18}F-FDG PET/CT findings. Eur Radiol. 2020;30:247-260.
12. Peng B, Sun H, Hou J, Luo JX. PET/MRI is superior to PET/CT in detecting oesophago and gastric carcinomas: a meta-analysis. Cancer Imaging. 2025;25:50.
13. Liu Y, Zheng D, Liu JJ, Cui JX, Xi HQ, Zhang KC, Huang XH, Wei B, Wang XX, Xu BX, Li K, Gao YH, Liang WQ, Tian JH, Chen L. Comparing PET/MRI with PET/CT for pretreatment staging of gastric cancer. Gastroenterol Res Pract. 2019;2019:9564627.
14. Zheng D, Liu Y, Liu J, Li K, Lin M, Schmidt H, Xu B, Tian J. Improving MR sequence of ^{18}F-FDG PET/MR for diagnosing and staging gastric cancer: a comparison study to ^{18}F-FDG PET/CT. Cancer Imaging. 2020;20:39.
15. Gülbahar Ateş S, Aydos U, Akdemir ÜÖ, Yüksel O, Üner A, Dursun A, Atay LÖ. Respiratory-gated ^{18}F fluorodeoxyglucose positron emission tomography/magnetic resonance imaging in evaluation of primary gastric lesions and gastric lymph nodes in patients with gastric cancer. Clin Oncol (R Coll Radiol). 2022;34:810-818.
16. Kim J, Lim ST, Na CJ, Han YH, Kim CY, Jeong HJ, Sohn MH. Pretreatment F-18 FDG PET/CT parameters to evaluate progression-free survival in gastric cancer. Nucl Med Mol Imaging. 2014;48:33-40.
17. Kwon HR, Pahk K, Park S, Kwon HW, Kim S. Prognostic value of metabolic information in advanced gastric cancer using preoperative ^{18}F-FDG PET/CT. Nucl Med Mol Imaging. 2019;53:386-395.
18. Lee JE, Hong SP, Ahn DH, Jeon TJ, Kang MK, Kwon CI, Ko KH, Hwang SG, Park PW, Rim KS. The role of ^{18}F-FDG PET/CT in the evaluation of gastric cancer recurrence after curative gastrectomy. Yonsei Med J. 2011;52:81-88.
19. Na SJ, o JH, Park JM, Lee HH, Lee SH, Song KY, Choi MG, Park CH. Prognostic value of metabolic parameters on preoperative ^{18}F-fluorodeoxyglucose positron emission tomography/computed tomography in patients with stage III gastric cancer. Oncotarget. 2016;7:63968-63980.
20. Song J, Li Z, Chen P, Yu J, Wang F, Yang Z, Wang X. A ^{18}FDG PET/CT-based volume parameter is a predictor of overall survival in patients with local advanced gastric cancer. Chin J Cancer Res. 2019;31:632-640.
21. Liu G, Yin H, Cheng X, Wang Y, Hu Y, Liu T, Shi H. Intra-tumor metabolic heterogeneity of gastric cancer on ^{18}F-FDG PETCT indicates patient survival outcomes. Clin Exp Med. 2021;21:129-138.
22. Chon HJ, Kim C, Cho A, Kim YM, Jang SJ, Kim BO, Park CH, Hyung WJ, Ahn JB, Noh SH, Yun M, Rha SY. The clinical implications of FDG-PET/CT differ according to histology in advanced gastric cancer. Gastric Cancer. 2019;22:113-122.
23. Giganti F, Tang L, Baba H. Gastric cancer and imaging biomarkers: part 1 - a critical review of DW-MRI and CE-MDCT findings. Eur Radiol. 2019;29:1743-1753.
24. Lambrecht M, Van Calster B, Vandecaveye V, De Keyzer F, Roebben I, Hermans R, Nuyts S. Integrating pretreatment diffusion weighted MRI into a multivariable prognostic model for head and neck squamous cell carcinoma. Radiother Oncol. 2014;110:429-434.
25. Matsumoto M, Tsunematsu M, Hamura R, Haruki K, Furukawa K, Shirai Y, Uwagawa T, Onda S, Taniai T, Tanji Y, Yanagaki M, Ikegami T. The minimum apparent diffusion coefficient value on preoperative magnetic resonance imaging in resectable pancreatic cancer: a new prognostic factor for biologically borderline resectable pancreatic cancer. Surg Today. 2025;55:1461-1470.
26. Giganti F, Ambrosi A, Chiari D, Orsenigo E, Esposito A, Mazza E, Albarello L, Staudacher C, Del Maschio A, De Cobelli F. Apparent diffusion coefficient by diffusion-weighted magnetic resonance imaging as a sole biomarker for staging and prognosis of gastric cancer. Chin J Cancer Res. 2017;29:118-126.
27. Giganti F, Orsenigo E, Esposito A, Chiari D, Salerno A, Ambrosi A, Albarello L, Mazza E, Staudacher C, Del Maschio A, De Cobelli F. Prognostic role of diffusion-weighted MR imaging for resectable gastric cancer. Radiology. 2015;276:444-452.
28. Dal Cero M, Bencivenga M, Liu DHW, Sacco M, Alloggio M, Kerckhoffs KGP, Filippini F, Saragoni L, Iglesias M, Tomezzoli A, Carneiro F, Grabsch HI, Verlato G, Torroni L, Piessen G, Pera M, de Manzoni G. Clinical features of gastric signet ring cell cancer: results from a systematic review and meta-analysis. Cancers (Basel). 2023;15.
29. Piessen G, Messager M, Leteurtre E, Jean-Pierre T, Mariette C. Signet ring cell histology is an independent predictor of poor prognosis in gastric adenocarcinoma regardless of tumoral clinical presentation. Ann Surg. 2009;250:878-887.
30. Chon HJ, Hyung WJ, Kim C, Park S, Kim JH, Park CH, Ahn JB, Kim H, Chung HC, Rha SY, Noh SH, Jeung HC. Differential prognostic implications of gastric signet ring cell carcinoma: stage adjusted analysis from a single high-volume Center in Asia. Ann Surg. 2017;265:946-953.
31. Mariette C, Carneiro F, Grabsch HI, van der Post RS, Allum W, de Manzoni G; European Chapter of International Gastric Cancer Association. Consensus on the pathological definition and classification of poorly cohesive gastric carcinoma. Gastric Cancer. 2019;22:1-9.
32. Song BI, Kim HW, Won KS, Ryu SW, Sohn SS, Kang YN. Preoperative standardized uptake value of metastatic lymph nodes measured by ^{18}F-FDG PET/CT improves the prediction of prognosis in gastric cancer. Medicine (Baltimore). 2015;94:e1037.
33. Kwon HW, An L, Kwon HR, Park S, Kim S. Preoperative nodal ^{18}F-FDG avidity rather than primary tumor avidity determines the prognosis of patients with advanced gastric cancer. J Gastric Cancer. 2018;18:218-229.

Original Article

Mol Imaging Radionucl Ther 2026;35(1):28-34

DOI:*10.4274/mirt.galenos.2025.75768*

Beyond the Primary Tumor: Malignancy Risk and Evaluation Strategies for ^{18}F-FDG PET/CT-Detected Incidentalomas

Primer Tümörün Ötesinde: ^{18}F-FDG PET/BT ile Saptanan İnsidentalomalarda Malignite Riski ve Değerlendirme Stratejileri

Yasemin Keskin[1], Damla Bağcı[1], Ali Haluk Ulucanlar[1], Gülin Uçmak[2]

[1]*University of Health Sciences Türkiye, Dr. Abdurrahman Yurtaslan Ankara Oncology Training and Research Hospital, Clinic of General Surgery, Ankara, Türkiye*

[2]*University of Health Sciences Türkiye, Dr. Abdurrahman Yurtaslan Ankara Oncology Training and Research Hospital, Clinic of Nuclear Medicine, Ankara, Türkiye*

Abstract

Objectives: The increasing use of ^{18}F-fluorodeoxyglucose positron emission tomography/computed tomography (^{18}F-FDG PET/CT) imaging has led to the frequent detection of incidentalomas. This study aimed to investigate the prevalence, locations, malignancy rates, and clinical evaluations of incidentalomas detected during preoperative staging with ^{18}F-FDG PET/CT in patients with surgically relevant primary tumors.

Methods: A total of 251 patients who underwent preoperative ^{18}F-FDG PET/CT imaging between January 2019 and December 2023 were retrospectively analyzed. Incidental uptake sites were classified into six anatomical regions: thyroid, colon, rectum, prostate, cervix/uterus, and breast. Data regarding maximum standardized uptake value (SUV_{max}) values, biopsy status, imaging follow-up, and histopathological outcomes were recorded and compared with population-based incidence data from the literature.

Results: The most frequent incidentalomas were detected in the thyroid (11.6%), followed by cervix/uterus (9.6%), colon (7.6%), prostate (4.4%), breast (2.4%), and rectum (2.0%). Malignancy was confirmed in incidentalomas of the thyroid (85.7%), prostate (83.3%), colon (71.4%), rectum (50.0%), and breast (33.3%). Malignancy rates for the thyroid, breast, colorectal, and prostate groups were significantly higher than population-based estimates ($p<0.05$). No statistically significant correlation was found between SUV_{max} and malignancy status across localization groups.

Conclusion: Incidental findings on ^{18}F-FDG PET/CT imaging are common and carry a considerable risk of malignancy, particularly in thyroid, prostate, and colorectal sites. Given the observed diagnostic yield, further clinical evaluation, including tissue diagnosis, should be considered in cases with focal uptake, especially when located in high-risk anatomical regions. Awareness of these findings is essential for timely management and appropriate therapeutic decision-making.

Keywords: Incidentaloma, malignancy, preoperative staging, ^{18}F-FDG PET/CT

Öz

Amaç: ^{18}F-florodeoksiglukoz pozitron emisyon tomografisi/bilgisayarlı tomografi (^{18}F-FDG PET/BT) kullanımının artması, insidentalomaların sık tespit edilmesine yol açmıştır. Bu çalışmada, cerrahi açısından anlamlı primer tümörü olan hastalarda preoperatif evreleme sırasında ^{18}F-FDG PET/BT ile saptanan insidentalomaların prevalansı, lokalizasyonu, malignite oranları ve klinik değerlendirme süreçleri araştırılmıştır.

Address for Correspondence: Yasemin Keskin, University of Health Sciences Türkiye, Dr. Abdurrahman Yurtaslan Ankara Oncology Training and Research Hospital, Clinic of General Surgery, Ankara, Türkiye

E-mail: konuk.yasemin@gmail.com **ORCID ID:** orcid.org/0000-0002-2618-3349

Received: 23.06.2025 **Accepted:** 11.11.2025 **Epub:** 19.12.2025 **Publication Date:** 03.02.2026

Cite this article as: Keskin Y, Bağcı D, Ulucanlar AH, Uçmak G. Beyond the primary tumor: malignancy risk and evaluation strategies for ^{18}F-FDG PET/CT-detected incidentalomas. Mol Imaging Radionucl Ther. 2026;35(1):28-34.

Yöntem: Ocak 2019-Aralık 2023 tarihleri arasında preoperatif ^{18}F-FDG PET/BT görüntülemesi yapılan toplam 251 hasta retrospektif olarak incelenmiştir. Saptanan insidental tutulumlar anatomik olarak altı bölgeye ayrılmıştır: tiroid, kolon, rektum, prostat, serviks/uterus ve meme. İlgili odaklara ait maksimum standart tutulum değeri (SUV$_{maks}$) değerleri, biyopsi durumu, görüntüleme takipleri ve histopatolojik sonuçlar kaydedilmiş ve literatürdeki toplum temelli insidans verileriyle karşılaştırılmıştır.

Bulgular: En sık insidentalomalar tiroidde (%11,6), ardından serviks/uterus (%9,6), kolon (%7,6), prostat (%4,4), meme (%2,4) ve rektumda (%2,0) saptanmıştır. Malignite oranları tiroidde %85,7, prostatta %83,3, kolonda %71,4, rektumda %50,0 ve memede %33,3 olarak belirlenmiştir. Tiroid, meme, kolorektal ve prostat gruplarında saptanan malignite oranları, toplum temelli tahminlere kıyasla anlamlı derecede yüksek saptanmıştır ($p<0,05$). SUV$_{maks}$ değerleri ile malignite durumu arasında lokalizasyon grupları genelinde istatistiksel olarak anlamlı bir ilişki saptanmamıştır.

Sonuç: ^{18}F-FDG PET/BT görüntülemesinde saptanan insidental bulgular yaygın olup özellikle tiroid, prostat ve kolorektal bölgelerde belirgin bir malignite riski taşımaktadır. Tanısal testlerin artışı göz önüne alındığında, odak tutulumu gösteren ve yüksek riskli anatomik bölgelerde yer alan lezyonlarda doku tanısı dahil olmak üzere ileri klinik değerlendirme önerilmelidir. Bu bulgulara yönelik farkındalık, zamanında müdahale ve uygun tedavi kararlarının verilmesi açısından kritik öneme sahiptir.

Anahtar kelimeler: İnsidentaloma, malignite, preoperatif evreleme, ^{18}F-FDG PET/CT

Introduction

The term "positron emission tomography (PET)-associated incidental neoplasm (PAIN)" was first described by Katz and Shaha (1) in their 2008 publication and refers to a neoplasm incidentally detected during PET/computed tomography (CT) imaging performed for unrelated reasons.

Incidental findings detected on ^{18}F-fluorodeoxyglucose (^{18}F-FDG) PET/CT are more frequent in patients older than 45 years, with a cumulative incidence ranging from 0.2% to 8.9%. Since FDG uptake is related to cellular glucose transport, it may occur not only in malignancies but also in infections, inflammation, and benign tumors. The prevalence of malignant incidentalomas varies between 1.2% and 1.7% (2).

In patients with a known diagnosis of malignancy, examinations typically focus on the primary disease, which may lead to overlooking a coincident benign or malignant lesion. However, the presence of an additional neoplasm is not negligible, and incidentalomas require further qualified evaluation and clinical investigation.

The aim of this study is to compare the rate of incidentalomas detected among patients hospitalized in the general surgery department with global incidence rates and to evaluate the proportion of patients who underwent further investigation and the distribution of benign and malignant lesions. Based on the data obtained, the study also aims to develop recommendations for clinicians regarding the appropriate management of incidentalomas.

Materials and Methods

Patient Selection

Patients who underwent surgery for a primary malignancy and received ^{18}F-FDG PET/CT imaging for preoperative staging at the Department of General Surgery, University of Health Sciences Türkiye, Dr. Abdurrahman Yurtaslan Ankara Oncology Training and Research Hospital, between January 2019 and December 2023 were retrospectively included in this study. Ethical approval was obtained from the Non-Interventional Clinical Research Ethics Committee of University of Health Sciences Türkiye, Dr. Abdurrahman Yurtaslan Ankara Oncology Training and Research Hospital under the (number: 2024-10/148, date: 31.10.2024).

Inclusion criteria for the study were patients aged 18 years or older and patients who underwent ^{18}F-FDG PET/CT imaging for staging of a primary malignancy within the field of general surgery. Exclusion criteria included patients under 18 years of age; patients whose ^{18}F-FDG PET/CT findings were attributable to metastasis; patients with inaccessible medical records; patients who were not followed up at our center; and patients who had received treatment targeting the primary tumor before staging.

Data Collection

The following were retrospectively reviewed: demographic characteristics (age and sex) of the patients included in the study; locations of their primary tumors; localizations of the incidentalomas; maximum standardized uptake value (SUV$_{max}$) of the incidentalomas; whether additional imaging was performed for the incidentalomas and the resulting imaging findings; whether a biopsy was performed for the incidentalomas and, if available, the biopsy results.

Study Design

In the present study, patients with primary tumors falling within the scope of general surgery—specifically those located in the esophagus, stomach, small intestine, colon, liver, gallbladder and biliary tract, pancreas, breast, and thyroid—were included. Based on an initial literature review, patients were grouped by the anatomical localization of incidentalomas, focusing on incidental uptake foci detected in the thyroid, colon, rectum, prostate, and breast. Any focal uptake in these regions that differed from typical patterns was considered suspicious for an incidentaloma.

Following identification of a cervical malignancy during further investigation of incidental uterine uptake in one patient, a uterus–cervix group was added to the classification. For all patients, the following were recorded: whether there was incidental uptake in these regions; the corresponding SUV_{max} values (without applying any threshold); whether further investigations were conducted; the outcomes of these investigations; and whether a biopsy was performed.

The objective of this research was to evaluate the frequency with which incidentalomas are detected on preoperative ^{18}F-FDG PET/CT scans relative to their incidence in the general population, and to quantify the proportion that represent malignant disease. The study sought to raise surgeons' awareness of the clinical significance of incidental findings.

^{18}F-FDG PET/CT

All patients underwent imaging using an integrated PET/CT scanner (Siemens Biograph 6 TruePoint). Prior to the ^{18}F-FDG PET/CT examination, patients fasted for at least 6 hours and serum glucose levels at the time of tracer administration were confirmed to be below 150 mg/dL. ^{18}F-FDG was administered intravenously at a dose of 3.3 MBq/kg (90 µCi/kg) via an automated infusion system (Intego PET Infusion system). PET and low-dose CT images were acquired in a single session, with the CT performed without intravenous iodinated contrast and covering the region from the skull vertex to the distal thighs. CT images were used for attenuation correction and anatomical localization. All image data were reviewed on a dedicated workstation (Syngovia, Siemens Medical Solutions) in standard planes, including maximum intensity projection views. Both visual assessment and quantitative analysis were performed. For quantitative evaluation, SUV_{max}, normalized to body weight, was manually determined for the primary tumor and relevant regions. All findings were documented in the whole-body ^{18}F-FDG PET/CT report.

Statistical Analysis

The data were analyzed using SPSS version 11.5. Descriptive statistics for categorical variables were expressed as frequency (percentage). For comparisons of numerical variables between two categories of a qualitative variable, the Mann-Whitney U test was used because the assumptions of normality were not met. To evaluate differences in numerical variables across qualitative variables with more than two categories, the Kruskal-Wallis H test was applied. When a significant difference among more than two groups was detected, Bonferroni-adjusted Mann-Whitney U tests were conducted to determine which specific group pairs accounted for the difference. Associations between categorical variables were analyzed using chi-square test and Fisher's exact test. A one-proportion Z test was used to compare the observed incidence rate in the study population with the known population rate. The risk factors affecting the categorical variable were analyzed using univariate and multivariate logistic regression analyses. A p value of less than 0.05 was considered statistically significant throughout the analyses.

Results

A total of 251 patients who underwent ^{18}F-FDG PET/CT for preoperative staging were included in the present study. The mean age of the patients was 61.68 years, and 72.1% were female. When patients were classified by primary tumor location, 157 (62.5%) had breast cancer, 32 (12.7%) rectal cancer, 21 (8.4%) gastric cancer, 18 (7.2%) colon cancer, 10 (4.9%) esophageal cancer, 9 (3.6%) pancreatic cancer, 2 (0.8%) thyroid cancer, and one patient each (0.4%) had liver or adrenal gland malignancies (Table 1).

Table 2 presents the localization of incidentalomas and tumor-related variables. Significant differences were observed between incidentaloma localization and SUV_{max}, tumor presence, and whether additional imaging was performed (p=0.001, p<0.001, and p=0.004, respectively). The highest mean SUV_{max} was observed in colon incidentalomas, whereas the lowest was observed in breast incidentalomas. Pairwise comparisons revealed that the significant differences in incidentaloma localization across primary tumor types were primarily driven by the following pairs: breast vs. cervix (p=0.025), breast vs. rectum (p=0.004), breast vs. colon (p<0.001), thyroid vs. colon (p<0.001), and prostate vs. colon (p=0.030).

Table 1. Descriptive data for demographic characteristics

Variables	
Age	
Mean ± SD	61.68±13.43
Gender, n (%)	
Female	181 (72.1)
Male	70 (27.9)
Primary tumor localization, n (%)	
Breast	157 (62.5)
Rectum	32 (12.7)
Stomach	21 (8.4)
Colon	18 (7.2)
Esophagus	10 (4.0)
Pancreas	9 (3.6)
Thyroid	2 (0.8)
Liver	1 (0.4)
Adrenal gland	1 (0.4)

SD: Standard deviation

Incidentaloma rates by anatomical site were: 11.6% in the thyroid, 9.6% in the cervix, 7.6% in the colon, 4.4% in the prostate, 2.4% in the breast, and 2.0% in the rectum. The distribution of incidentaloma locations by primary tumor site is presented in Table 3. All patients with rectal or breast incidentalomas underwent additional imaging, compared with 37.6% of thyroid incidentalomas, 78.9% of colon incidentalomas, 63.6% of prostate incidentalomas, and 70.8% of cervical incidentalomas.

The localization of incidentalomas was compared with prevalence rates reported in the literature. Table 4 presents a comparison of the study findings with population-based rates. Significantly higher detection rates were observed in the thyroid, breast, colorectal, and prostate groups than in the general population ($p<0.001$, $p<0.001$, $p=0.002$, and $p<0.001$, respectively). The population incidence rates were based on studies by Albano et al. (3) (thyroid), Panareo et al. (2) (breast), Treglia et al. (4) (colorectal), and Mannas et al. (5) (prostate). No reference data were identified in the literature regarding incidental cervical or uterine findings.

Following advanced evaluation of incidentalomas, the malignancy rates were as follows: 85.7% in the thyroid, 71.4% in the colon, 50.0% in the rectum, 83.3% in the prostate, and 33.3% in the breast.

Table 5 presents the analysis of SUV_{max} values in patients diagnosed with malignancy, stratified by incidentaloma localization. Despite this evaluation, the comparison of SUV_{max} between malignant and benign lesions across different sites did not demonstrate any statistically significant differences. ($p>0.05$) (Table 5).

Risk factors potentially affecting malignancy were evaluated (Table 6). Based on the results of univariate and multivariate logistic regression analyses, no variable was identified as a significant risk factor, either individually or in combination.

Table 2. Comparisons of variables based on incidentaloma localizations

Variables	**Incidentaloma localization**						**p value**
	Thyroid	**Colon**	**Rectum**	**Prostate**	**Cervix/uterus**	**Breast**	
Incidentaloma, n (%)	29 (11.6)	19 (7.6)	5 (2.0)	11 (4.4)	24 (9.6)	6 (2.4)	**<0.001**[b]
SUV_{max} Mean ± SD	4.65±1.94	9.74±4.85	7.82±2.09	5.77±4.01	5.92±2.75	2.80±0.96	**0.001**[a]
Additional imaging performed, n (%)	11 (37.9)	15 (78.9)	5 (100.0)	7 (63.6)	17 (70.8)	6 (100.0)	**0.004**[c]
Biopsy, n (%)	7 (24.1)	7 (36.8)	2 (40.0)	2 (18.2)	6 (25.0)	3 (50.0)	**0.642**[c]
Biopsy result, Benign Malign	 1 (14.3) 6 (85.7)	 2 (28.6) 5 (71.4)	 1 (50.0) 1 (50.0)	 1 (50.0) 1 (50.0)	 1 (16.7) 5 (83.3)	 2 (66.7) 1 (33.3)	0.365[c]

SD: Standard deviation, [a]: Kruskal-Wallis H test, [b]: Chi-square test, [c]: Fisher's exact test, SUV_{max}: Maximum standardized uptake value

Table 3. Incidentaloma distribution based on primary tumor localization

Primary tumor localization	**Incidentaloma localization, n (%)**					
	Thyroid	**Colon**	**Rectum**	**Prostate**	**Cervix/uterus**	**Breast**
Breast	19 (65.5)	6 (31.6)	3 (60.0)	1 (9.1)	19 (79.2)	5 (83.3)
Rectum	3 (10.3)	6 (31.6)	-	3 (27.2)	-	1 (16.7)
Stomach	4 (13.7)	3 (15.7)	-	5 (45.5)	2 (8.3)	-
Colon	1 (3.5)	2 (10.5)	1 (20.0)	1 (9.1)	3 (12.5)	-
Esophagus	1 (3.5)	1 (5.3)	1 (20.0)	1 (9.1)	-	-
Pancreas	1 (3.5)	1 (5.3)	-	-	-	
Thyroid	-	-	-	-	-	-
Liver	-	-	-	-	-	-
Adrenal gland	-	-	-	-	-	-

Table 4. Incidence rates of incidentaloma localizations

Incidentaloma localization	Incidence rate (%)	Population-based rate (%)	p value
Thyroid	12.0	4.0	**<0.001**[a]
Breast	2.4	1.2	**<0.001**[a]
Colorectal	7.6	3.6	**0.002**[a]
Prostate	4.4	1.4	**<0.001**[a]
Cervix/uterus	9.6	-	-

[a]: One-sample proportion test

Table 5. SUV_{max} values in malignant tumors confirmed by biopsy across incidentaloma localizations

Incidentaloma localization	SUV_{max}		p value
	Mean ± SD	Median (min-max)	
Thyroid	5.66±3.36	4.96 (1.95-10.78)	0.857[a]
Colon	10.91±6.46	8.57 (4.87-20.24)	0.381[a]
Rectum	5.09± -	5.09 (5.09-5.09)	1.000[a]
Prostate	17.49± -	17.49 (17.49-17.49)	1.000[a]
Cervix/uterus	7.28±3.14	7.00 (3.63-10.80)	0.333[a]
Breast	3.02± -	3.02 (3.02-3.02)	1.000[a]

SD: Standard deviation, Min: Minimum, Max: Maximum, [a]: Mann-Whitney U test, SUV_{max}: Maximum standardized uptake value

Table 6. Univariate and multivariate logistic regression analysis results for risk factors affecting malignancy

	Univariate			Multivariate		
Variables	OR	95% CI (min-max)	p value	OR	95% CI (min-max)	p value
Age	0.971	0.913-1.033	0.350	0.964	0.897-1.037	0.322
Gender (Female)	1.385	0.213-8.983	0.733	2.132	0.283-16.019	0.462
SUV_{max}	0.957	0.822-1.113	0.566	0.990	0.831-1.180	0.915

OR: Odds ratio, CI: Confidence interval, Min: Minimum, Max: Maximum, SUV_{max}: Maximum standardized uptake value

Discussion

Incidentalomas are lesions detected incidentally on imaging performed for unrelated clinical indications. With increasing use of ^{18}F-FDG PET/CT, detection of PAIN (PET-PAIN) has become more frequent. PAIN is most commonly observed in the thyroid, gastrointestinal tract, and lungs, with a reported cumulative incidence of 1-3% (2).

In our study, the overall rate of incidentalomas was slightly below the lower limit reported in the literature, with the thyroid being the most common site (11.6%). Previous reports suggest that 27-44% of all malignancies diagnosed incidentally on PET/CT originate from the thyroid gland (1). Thyroid uptake can appear as either diffuse or focal activity: diffuse uptake is associated with inflammatory conditions, whereas focal uptake is more frequently linked to nodular pathology. The reported incidence of focal thyroid uptake on ^{18}F-FDG PET/CT ranges from 2-4%, with an associated risk of malignancy of 20-30% (3). Larger cohort studies report variability in malignancy rates, ranging from 9.8% to 28% (6,7), which likely reflects differences in the patient populations selected for further evaluation. For example, while Chen et al. (8) reported a 14% malignancy rate with 83% of patients undergoing biopsy, another study found a 42% malignancy rate in a cohort where only 11% underwent biopsy (9). A review of more recent data reveals that Lee et al. (10) identified thyroid incidentalomas in 2.7% of patients, with a malignancy rate of 56.5% among these lesions.

In our study, 37.6% of patients underwent further imaging, and 24.1% underwent biopsy; malignancy was found in 85.7% of those biopsied. This high rate likely reflects a preselection bias favoring patients with higher clinical suspicion. Nonetheless, such a high malignancy rate may contribute to clinical uncertainty regarding which patients warrant further investigation or biopsy. This ambiguity can result in either unnecessary procedures or missed malignancy diagnoses. Therefore, patients with focal or unilateral thyroid uptake should be prioritized for further evaluation (1). Physical examination remains essential; malignancy rates were 24% in patients with thyroid-related findings on examination versus only 6% in those without. This underscores the importance of thorough physical assessment when thyroid incidentalomas are detected. While data on diffuse uptake are limited because biopsy is rarely performed in such cases, at a minimum, an ultrasonographic evaluation is advisable.

Breast incidentalomas are rare findings on PET/CT (2). In our cohort, they accounted for 2.4% of incidentalomas, the lowest rate observed. Notably, 62.5% of these cases represented primary breast malignancies. Panareo et al. (2) reported a 1.17% prevalence of breast incidentalomas among 3,675 patients undergoing PET/CT for non-breast malignancies; 15 of the 22 biopsied cases were malignant. Menon and Bourke (11) reported a malignancy risk of 56.2% for breast incidentalomas. In contrast, we observed a lower rate (33.3%), which may be attributable to the effectiveness of national breast cancer screening programs in Türkiye. In patients undergoing regular screenings with no significant risk factors, a more conservative approach may be appropriate.

The incidence of prostate incidentalomas has been reported as 0.086-1.4% (5). These lesions may represent prostate cancer, benign prostatic hyperplasia, or prostatitis. In our study, 63.6% of patients with prostate incidentalomas underwent further investigation, and 83.3% of these were found to have malignancy — a rate significantly higher than previously reported [5.4% by Han et al. (12) and 12.5% by Bertagna et al. (13)]. Bertagna et al. (13)]. These findings raise concerns about the 36.3% of patients who were not investigated further and highlight the need for heightened clinical vigilance and multidisciplinary collaboration in managing such cases.

Colon and rectal incidentalomas were observed in 7.6% and 2.0% of patients, respectively. Further investigations were conducted in 78.9% of colonic cases and in all rectal cases. A meta-analysis by Treglia et al. (4) reported a combined prevalence of 3.6% for focal colorectal incidentalomas, suggesting that our findings are higher. In our study, colonoscopic evaluation revealed malignant or premalignant lesions in 71.4% of colonic and 50.0% of rectal incidentalomas—the former slightly exceeding rates reported in the literature (68-69.5%) (4,14). This underscores the importance of a cautious approach to incidental colorectal uptake. Clinicians should also be mindful of physiological uptake patterns in the colon that could obscure malignant lesions. Endoscopic evaluation is warranted for all focal uptakes, even in the absence of morphological abnormalities.

Incidental uterine or cervical uptake was observed in 9.6% of patients—higher than that observed in the breast, prostate, colon, or rectum. However, existing literature offers limited data on these localizations. In our study, 70.8% of such cases underwent further assessment, and malignancy was confirmed in 83.3% of those assessed. These findings highlight the importance of increased awareness and more structured evaluation protocols for uterine/cervical incidentalomas.

SUV_{max} is often considered in clinical decision-making. However, it is influenced by tumor biology and various technical factors. Although multiple studies have attempted to establish SUV_{max} thresholds, results remain inconsistent in distinguishing between benign and malignant lesions (15-17). Consequently, SUV_{max} should not be used as a standalone predictor of malignancy. In recent years, studies have indicated that SUV_{max} serves as a valuable prognostic marker in patients with a confirmed diagnosis of malignancy (18-20). However, based on the findings of this study, SUV_{max} does not reliably distinguish benign from malignant lesions when histopathological confirmation is lacking.

Study Limitations

This study has several limitations. Patients with incidental uptake who were not evaluated further may have been inadvertently excluded. Additionally, not all patients underwent biopsy, potentially introducing selection bias in malignancy rate estimates.

Conclusion

This study highlights the importance of further evaluation of incidental uptakes detected by ^{18}F-FDG PET/CT and the need for tissue diagnosis based on the characteristics of the lesions. Unlike other imaging modalities, PET/CT provides comprehensive information by evaluating the entire body rather than focusing on a specific region. Incidental findings outside the primary malignancy site occur with a notable frequency and should not be underestimated. For clinicians, awareness of such findings is crucial in identifying patient groups who may require further diagnostic work-up and treatment.

Ethics

Ethics Committee Approval: Ethical approval was obtained from the Non-Interventional Clinical Research Ethics Committee of University of Health Sciences Türkiye, Dr. Abdurrahman Yurtaslan Ankara Oncology Training and Research Hospital under the (number: 2024-10/148, date: 31.10.2024).

Informed Consent: This study has been reviewed retrospectively.

Footnotes

Authorship Contributions

Surgical and Medical Practices: Y.K., D.B., A.H.U., Concept: Y.K., D.B., A.H.U., G.U., Design: Y.K., D.B., Data Collection or Processing: Y.K., D.B., Analysis or Interpretation: Y.K., A.H.U., Literature Search: Y.K., G.U., Writing: Y.K., D.B., A.H.U., G.U.

Conflict of Interest: No conflict of interest was declared by the authors.

Financial Disclosure: The authors declared that this study has received no financial support.

References

1. Katz SC, Shaha A. PET-associated incidental neoplasms of the thyroid. J Am Coll Surg. 2008;207:259-264.
2. Panareo S, Urso L, Nieri A, Caracciolo M, Valpiani G, Torricelli P, Frassoldati A, Cittanti C, Rollo M, Bartolomei M. Clinical-diagnostic relevance of breast “incidentaloma” detected during ^{18}F-fluoro-2-deoxy-D-glucose positron emission tomography/computed tomography: correlation with radiological imaging and histopathology. Indian Journal of Nuclear Medicine. 2021;36:385-390.
3. Albano D, Durmo R, Bertagna F, Giubbini R. ^{18}F-choline PET/CT incidental thyroid uptake in patients studied for prostate cancer. Endocrine. 2019;63:531-536.
4. Treglia G, Taralli S, Salsano M, Muoio B, Sadeghi R, Giovanella L. Prevalence and malignancy risk of focal colorectal incidental uptake detected by (18)F-FDG-PET or PET/CT: a meta-analysis. Radiol Oncol. 2014;48:99-104.
5. Mannas MP, Lee T, Pourghiasian M, Wilson DC, Black PC. Incidentalomas of the prostate detected by 18-fluoro-2-deoxy-D-glucose positron emission tomography/computed tomography. Can Urol Assoc J. 2020;14:E180-E184.
6. Ceriani L, Milan L, Virili C, Cascione L, Paone G, Trimboli P, Giovanella L. Radiomics analysis of [^{18}F]-fluorodeoxyglucose-avid thyroid incidentalomas improves risk stratification and selection for clinical assessment. Thyroid. 2021;31:88-95.
7. Erdoğan M, Korkmaz H, Torus B, Avcı M, Boylubay ŞM, Çiriş M, Yıldız M, Şengül SS. The role of metabolic volumetric parameters in predicting malignancy in incidental thyroid nodules detected in ^{18}F-FDG PET/CT Scans. Mol Imaging Radionucl Ther. 2021;30:86-92.
8. Chen YK, Ding HJ, Chen KT, Chen YL, Liao AC, Shen YY, Su CT, Kao CH. Prevalence and risk of cancer of focal thyroid incidentaloma identified by ^{18}F-fluorodeoxyglucose positron emission tomography for cancer screening in healthy subjects. Anticancer Res. 2005;25:1421-1426.
9. Are C, Hsu JF, Schoder H, Shah JP, Larson SM, Shaha AR. FDG-PET detected thyroid incidentalomas: need for further investigation? Ann Surg Oncol. 2006;14:239-247.
10. Lee H, Chung YS, Lee JH, Lee KY, Hwang KH. Characterization of focal hypermetabolic thyroid incidentaloma: an analysis with F-18 fluorodeoxyglucose positron emission tomography/computed tomography parameters. World J Clin Cases. 2022;10:155-5.
11. Menon P, Bourke A. Breast incidentalomas on 18- Fluorodeoxyglucose positron emission tomography-computed tomography performed for a non-mammary cause: significance and outcomes. J Med Imaging Radiat Oncol. 2023;67:357-364.
12. Han EJ, H O J, Choi WH, Yoo IR, Chung SK. Significance of incidental focal uptake in prostate on 18-fluoro-2-deoxyglucose positron emission tomography CT images. Br J Radiol. 2010;83:915-920.
13. Bertagna F, Piccardo A, Dib B, Bertoli M, Fracassi F, Bosio G, Giubbini R, Biasiotto G, Giovanella L, Treglia G. Multicentre study of ^{18}F-FDG-PET/CT prostate incidental uptake. Jpn J Radiol. 2015;33:538-546. Epub 2015 Jul 8.
14. Servente L, Gigirey V, García Fontes M, Alonso O. Incidental focal colonic uptake in studies ^{18}F-FDG PET/CT. Rev Esp Med Nucl Imagen Mol. 2018;37:15-19.
15. Thuillier P, Bourhis D, Roudaut N, Crouzeix G, Alavi Z, Schick U, Robin P, Kerlan V, Salaun PY, Abgral R. Diagnostic value of FDG PET-CT quantitative parameters and deauville-like 5 point-scale in predicting malignancy of focal thyroid incidentaloma. Front Med (Lausanne). 2019;6:24.
16. Bertagna F, Treglia G, Piccardo A, Giubbini R. Diagnostic and clinical significance of F-18-FDG-PET/CT thyroid incidentalomas. J Clin Endocrinol Metab. 2012;97:3866-3875.
17. Gherghe M, Lazar AM, Mutuleanu MD, Stanciu AE, Martin S. Radiomics analysis of [^{18}F]FDG PET/CT thyroid incidentalomas: how can it improve patients’ clinical management? A systematic review from the literature. Diagnostics (Basel). 2022;12:471.
18. Lim JH, Choi JY, Im Y, Yoo H, Jhun BW, Jeong BH, Park HY, Lee K, Kim H, Kwon OJ, Han J, Ahn MJ, Kim J, Um SW. Prognostic value of SUVmax on ^{18}F-fluorodeoxyglucose PET/CT scan in patients with malignant pleural mesothelioma. PLoS One. 2020;15:e0229299.
19. McGahan W, Chikatamarla V, Thomas P, Cavallucci D, O’Rourke N, Burge M. High SUVmax on routine pre-operative FDG-PET predicts early recurrence in pancreatic and peri-ampullary cancer. HPB (Oxford). 2022;24:1387-1393. Epub 2022 Jan 30.
20. Lee MI, Jung YJ, Kim DI, Lee S, Jung CS, Kang SK, Pak K, Kim SJ, Kim HY. Prognostic value of SUVmax in breast cancer and comparative analyses of molecular subtypes: a systematic review and meta-analysis. Medicine (Baltimore). 2021;100:e2674.

Original Article

Mol Imaging Radionucl Ther 2026;35(1):35-43 ***DOI:****10.4274/mirt.galenos.2025.92259*

Quantitative characterization of ^{18}F-PSMA-1007 and [^{68}Ga]Ga-PSMA-11 PET-CT Imaging in Suspected Prostate Cancer: A Single-centre Experience

Şüpheli Prostat Kanserinde ^{18}F-PSMA-1007 ve [^{68}Ga]Ga-PSMA-11 PET-BT Görüntülemesinin Kantitatif Karakterizasyonu: Tek Merkezli Bir Deneyim

Bal Sanghera[1], Gerry Lowe[2], Sophie Sanghera[3], Wai Lup Wong[4]

[1]*St. Barts Health Nhs Trust, Clinic of Nuclear Medicine, London, United Kingdom*
[2]*Paul Strickland Scanner Centre, Clinic of Pet Physics, Northwood, United Kingdom*
[3]*King College London Faculty of Medicine, Department of Physics, London, United Kingdom*
[4]*Paul Strickland Scanner Centre, Clinic of Radiology, Northwood, United Kingdom*

Abstract

Objectives: We record quantitative differences between ^{18}F-prostate specific membrane antigen (^{18}F-PSMA)-1007 and [^{68}Ga]Ga-PSMA-11 positron emission tomography (PET) prostate scans at our centre to investigate if significant differences exist between suspected lesion and lesion/background parameters studied. We also assess the potential impact of such differences on tracer interchangeability when supply is constrained.

Methods: Sixty-one [^{68}Ga]Ga-PSMA-11 and seventy-two ^{18}F-PSMA-1007 patients were analysed in two cohorts, each comprising 200 lesions. Clinical reports were used to determine maximum standard uptake values (SUV_{max}) was recorded for suspected lesions (T). Similarly, normalisations of mean standardized uptake (SUV_{mean}) and standardized uptake value-peak (SUV_{peak}) using lean body mass (SUV_{lbm}) and body surface area (SUV_{bsa}) were estimated. SUV_{mean} of liver backgrounds (B) was recorded to estimate T/B ratios. Metabolic tumour volume and total lesion PSMA (TL-PSMA) were investigated as functional volume surrogates. The Mann-Whitney U test was used to identify significant differences between the [^{68}Ga]Ga-PSMA-11 and ^{18}F-PSMA-1007 distributions.

Results: Significant differences were observed for lesion SUV_{max} ($p=0.0004$), SUV_{peak} ($p=0.0017$), SUV_{mean} ($p=0.0007$), SUV_{lbm} ($p=0.0002$), and SUV_{bsa} ($p=0.0005$) in lesions with higher [^{68}Ga]Ga-PSMA-11 SUV. Similarly, significant differences were observed in liver SUV_{max} ($p<0.0001$), SUV_{peak} ($p<0.0001$), and SUV_{mean} ($p<0.0001$), with higher values for ^{18}F-PSMA-1007. T/B ($p<0.0001$) and TL-PSMA ($p=0.0063$) also exhibited significantly higher [^{68}Ga]Ga-PSMA-11 values.

Conclusion: Consistent, predictable, and significant differences were observed in ^{18}F-PSMA-1007 and [^{68}Ga]Ga-PSMA-11 PET scans of lesion, liver, volume surrogates, supporting tracer interchangeability for patients with suspected prostate cancer. Our results also support the recent commissioning of PSMA-based PET tracers in England.

Keywords: PET-CT, prostate, fluorine radioisotopes, gallium radioisotopes, quantitative evaluation, PSMA-1007, Gallium-68 PSMA-11

Address for Correspondence: Bal Sanghera, St. Barts Health Nhs Trust, Clinic of Nuclear Medicine, London, United Kingdom
E-mail: bal.sanghera@nhs.net **ORCID ID:** orcid.org/0000-0003-0206-7834

Received: 16.06.2025 **Accepted:** 21.12.2025 **Publication Date:** 03.02.2026

Cite this article as: Sanghera B, Lowe G, Sanghera S, Wong WL. Quantitative characterization of ^{18}F-PSMA-1007 and [^{68}Ga]Ga-PSMA-11 PET-CT imaging in suspected prostate cancer: a single-centre experience. Mol Imaging Radionucl Ther. 2026;35(1):35-43.

Öz

Amaç: Merkezimizde, ^{18}F-prostat spesifik membran antijeni (^{18}F-PSMA)-1007 ile [^{68}Ga]Ga-PSMA-11 pozitron emisyon tomografisi (PET) prostat görüntülemeleri arasındaki nicel farklılıkları kaydederek, şüpheli lezyonlar ile lezyon/arka plan parametreleri arasında anlamlı farklar olup olmadığını araştırmayı amaçladık. Ayrıca, tedarik kısıtlı olduğunda bu farklılıkların radyofarmasötiklerin birbirinin yerine kullanılabilirliği üzerindeki olası etkisini değerlendirdik.

Yöntem: İki kohortta incelenmek üzere, 61 adet [^{68}Ga]Ga-PSMA-11 ve 72 adet ^{18}F-PSMA-1007 hastası analiz edildi; her kohort 200 lezyon içermekteydi. Klinik raporlar kullanılarak şüpheli lezyonlar (T) için maksimum standart tutulum değeri (SUV$_{maks}$) kaydedildi. Benzer şekilde, ortalama standart tutulum (SUV$_{ortalama}$) ve standart tutulum değeri-tepe (SUV$_{zirve}$), yağsız vücut kütlesi (SUV$_{lbm}$) ve vücut yüzey alanı (SUV$_{bsa}$) ile normalize edilerek hesaplandı. T/B (tümör/arka plan) oranlarını tahmin etmek amacıyla karaciğer arka planlarının SUV$_{ortalama}$ değerleri kaydedildi. Metabolik tümör hacmi ve toplam lezyon PSMA (TL-PSMA), fonksiyonel hacim göstergeleri olarak incelendi. [^{68}Ga]Ga-PSMA-11 ile ^{18}F-PSMA-1007 dağılımları arasındaki anlamlı farkları belirlemek için Mann-Whitney U testi kullanıldı.

Bulgular: Lezyon SUV$_{maks}$ (p=0,0004), SUV$_{zirve}$ (p=0,0017), SUV$_{ortalama}$ (p=0,0007), SUV$_{lbm}$ (p=0,0002) ve SUV$_{bsa}$ (p=0,0005) değerlerinde, daha yüksek [^{68}Ga]Ga-PSMA-11 SUV'u olan lezyonlarda anlamlı farklar gözlendi. Benzer şekilde, karaciğer SUV$_{maks}$ (p<0,0001), SUV$_{zirve}$ (p<0,0001) ve SUV$_{ortalama}$ (p<0,0001) değerlerinde de anlamlı farklar saptandı ve bu değerler ^{18}F-PSMA-1007 için daha yüksekti. T/B oranı (p<0,0001) ve TL-PSMA (p=0,0063) da anlamlı olarak daha yüksek [^{68}Ga]Ga-PSMA-11 değerleri gösterdi.

Sonuç: ^{18}F-PSMA-1007 ve [^{68}Ga]Ga-PSMA-11 PET görüntülemelerinde lezyon, karaciğer ve hacim göstergelerine ilişkin tutarlı, öngörülebilir ve anlamlı farklılıklar gözlenmiştir. Bu bulgular, prostat kanseri şüphesi olan hastalarda radyofarmasötiklerin birbirinin yerine kullanılabilirliğini desteklemektedir. Sonuçlarımız ayrıca İngiltere'de PSMA tabanlı PET radyofarmasötiklerinin yakın zamanda devreye alınmasını da desteklemektedir.

Anahtar kelimeler: PET-BT, prostat, flor radyoizotopları, galyum radyoizotopları, nicel değerlendirme, PSMA-1007, Galyum-68 PSMA-11

Introduction

Prostate cancer is the most frequently diagnosed cancer and the second most common cause of death among males in the United Kingdom (UK) (1). The most widely used positron emission tomography/computed tomography (PET/CT) oncology imaging agent in England is ^{18}F-fluorodeoxyglucose but it has limitations in diagnosing prostate cancer (2). In contrast, prostate specific membrane antigen (PSMA) imaging agents, such as [^{68}Ga]Ga-PSMA and ^{18}F-PSMA, have shown promise in clinical practice (3,4) and in targeted radioligand therapy applications (5). New prostate cancer-targeted PET imaging agents continue to be developed (6,7,8,9) while ^{99m}Tc-labelled PSMA ligands for single-photon emission tomography have also been explored for logistical reasons (10).

Availability of PET imaging agents is often limited in the UK, leading to diagnostic delays. Generator-eluted [^{68}Ga]Ga-PSMA-11, with a short half-life (~68 minutes), has been used widely because of its availability. However, ^{18}F-PSMA-1007, with a longer half-life (~110 minutes), offers greater geographic availability. This may address regional supply inequities while receiving substantial clinical support.

Many prostate cancer imaging studies have focused on the efficacy of radiopharmaceuticals using qualitative parameters such as detectability. However, more recent investigations have compared quantitative differences and their potential impact on analyses (11,12). For example, the VISION prostate cancer trial (13,14) incorporates lutetium-177 (^{177}Lu) Lu-PSMA-617 therapy and defines positive lesions as those with lesion-to-liver uptake ratios tumor-to-background (T/B) >1 measured on ^{68}Ga-PSMA-11 PET/CT scans.

However, different biodistribution effects have been identified between ^{18}F-PSMA-1007 and [^{68}Ga]Ga-PSMA-11 uptake in prostate cancer, leading to significant differences in lesion maximum standard uptake values (SUV$_{max}$). Increased hepatic excretion results in significantly higher ^{18}F-PSMA-1007 liver mean standardized uptake (SUV$_{mean}$), and similar significant differences are observed in the blood pool and spleen (4). Caution is therefore advised when the liver is used as a background tissue in T/B ratio estimation and when tracers are interchanged due to supply shortages. Characterising PET/CT quantitative parameters is essential for interpreting the clinical consequences of using different tracers. This highlights the importance of precise quantitative PET investigations (15,16).

In this study, routine clinically referred PET/CT scans using ^{18}F-PSMA-1007 and [^{68}Ga]Ga-PSMA-11 for suspected prostate cancer are characterised. Quantitative differences between radiopharmaceuticals are recorded, and their clinical implications are discussed, particularly when radiopharmaceuticals are interchanged. Ideally, the results of this local quantitative study can support national commissioning approval of PET-PSMA imaging agents. This outcome would reduce waiting lists and enhance clinical workflows for prostate cancer diagnosis and treatment.

Materials and Methods

A total of 61 [^{68}Ga]Ga-PSMA-11 and 72 ^{18}F-PSMA-1007 standard-of-care patients were scanned at our centre according to routine referral criteria for clinical indications of suspected prostate cancer. The inclusion criteria comprised all consecutively scanned subjects identified in the PET imaging database. Patients with observed liver lesions were excluded from further analysis.

Subjects were analysed as two separate imaging-agent cohorts, each consisting of 200 suspected lesions, including metastatic sites of disease. Within the [^{68}Ga]Ga-PSMA-11 cohort, the mean ± standard deviation (SD) for weight, body surface area ($_{bsa}$), lean body mass ($_{lbm}$), injected activity, and uptake time were 86.1±16.9 kg, 2±0.2 m^2, 63.2±6.8 kg, 187.8±23.9 MBq, and 63.3±9.7 min, respectively. The same values in ^{18}F-PSMA-1007 subjects were 83.6±13.6 kg, 2±0.2 m2, 61.4±7.1 kg, 342±42 MBq, and 94.1±8 MBq, respectively.

Images were acquired using a BIOGRAPH mCT-S64 4R PET/CT scanner operating in step-and-shoot mode. Corrections for geometry, randoms, dead time, scatter, and attenuation were applied to the emission data. PET images were reconstructed using ordered-subsets expectation maximization with point-spread-function modeling and time-of-flight, using 2 iterations, 21 subsets, a 200 × 200 matrix, and a 5-mm FWHM Gaussian filter. Non-contrast CT scan parameters were as follows: 120 kVp; 10 mA for the topogram; 120 kVp with modulated mA; pitch of 0.8; and 3-mm CT slices. The scanner adhered to strict QC protocols, received manufacturer-recommended servicing, and was accredited annually under the Guy's and St Thomas' PET Core Lab national clinical trial programme.

Finalized clinical reports, created by PET/CT consultant radiologists, were reviewed by experienced PET physicists to identify the location of reported or suspected lesions. Lesion SUV$_{max}$, SUV$_{mean}$, standardized uptake value-peak (SUV$_{peak}$), SUV$_{lbm}$, and SUV$_{bsa}$ normalizations were recorded for each imaging agent. Liver background SUV$_{mean}$ was also noted, and the ratio of suspected lesion SUV$_{max}$ to liver background SUV$_{mean}$ was calculated to derive T/B ratios. Furthermore, functional volume-based surrogates metabolic tumor volume (MTV) and total lesion PSMA /(TL-PSMA) (i.e., MTV x lesion SUV$_{mean}$) were compared between the ^{18}F-PSMA-1007 and [^{68}Ga]Ga-PSMA-11 cohorts.

Siemens Syngo.viaTM imaging analysis software, with manual operator control, was used to record SUVs using different normalizations and to estimate MTV and TL-PSMA for each patient. The Shapiro-Wilk normality test in the StatsDirect^{TM} statistical software package indicated that Mann-Whitney analysis should be used to identify significant differences between the distributions of [^{68}Ga]Ga-PSMA-11 and ^{18}F-PSMA-1007. A 95% confidence interval was used, and statistical significance was defined as $p<0.05$. This study was conducted as an anonymized clinical audit without the need for patient consent.

Results

A total of 133 patients and 400 suspected lesions, identified on ^{18}F-PSMA-1007 and [^{68}Ga]Ga-PSMA-11 PET/CT scans, were analysed. Results are presented in box-and-whisker plots (minimum, first quartile, median, third quartile, maximum), with the mean value denoted by X.

Suspected Lesion SUV

Statistically significant differences were observed in the distributions of SUV$_{max}$ ($p=0.0004$), SUV$_{peak}$ ($p=0.0017$), and SUV$_{mean}$ ($p=0.0007$) between [^{68}Ga]Ga-PSMA-11 and ^{18}F-PSMA-1007 (Figure 1). These differences were also observed in SUV$_{lbm}$ ($p=0.0002$) and SUV$_{bsa}$ ($p=0.0005$) normalizations. In all cases, [^{68}Ga]Ga-PSMA-11 exhibited higher mean and median values than ^{18}F-PSMA-1007 (Figure 2).

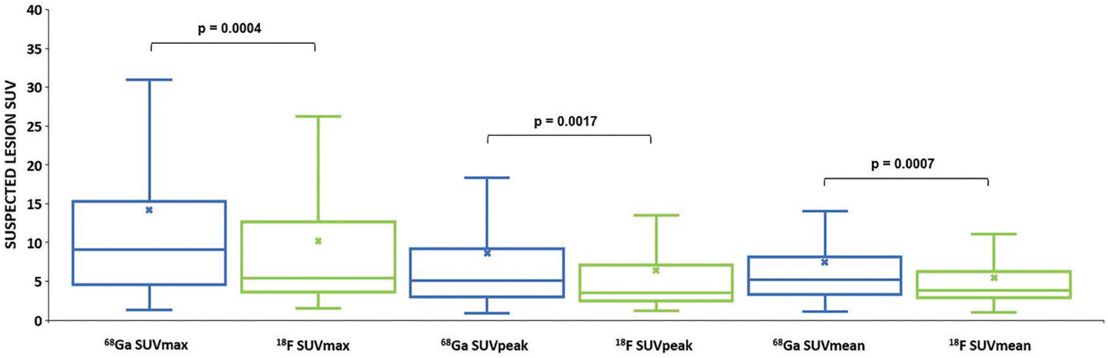

Figure 1. Suspected lesion SUV$_{max}$, SUV$_{peak}$, SUV$_{mean}$ distributions in [^{68}Ga]Ga-PSMA-11 and ^{18}F-PSMA-1007 PET scans

SUV$_{max}$: Maximum standard uptake values, SUV$_{mean}$: Mean standardized uptake, SUV$_{peak}$: Standardized uptake value-peak, ^{18}F-PSMA: ^{18}F-prostate specific membrane antigen, PET: Positron emission tomography, SUV$_{bsa}$: Body surface area, SUV$_{lsa}$: Lean body mass

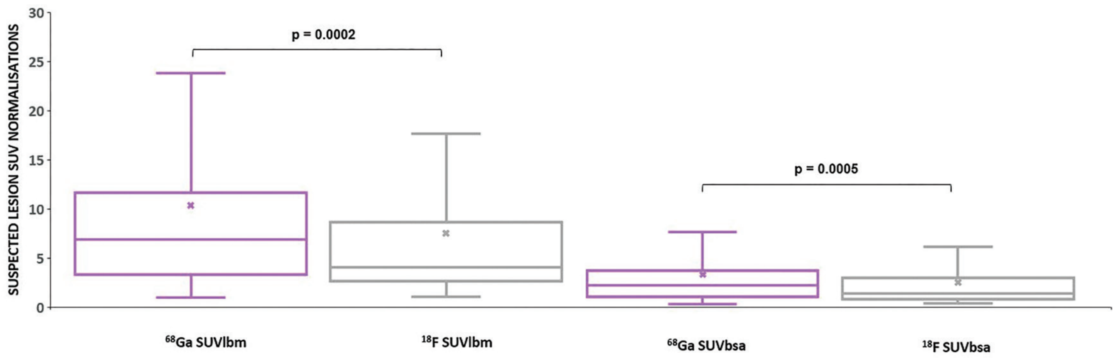

Figure 2. Suspected lesion SUV$_{max}$ with lean body mass and surface area normalisation distributions in [^{68}Ga]Ga-PSMA-11 and ^{18}F-PSMA-1007 PET scans

SUV$_{max}$: Maximum standard uptake values, ^{18}F-PSMA: ^{18}F-prostate specific membrane antigen, PET: Positron emission tomography

Liver SUV

Liver SUV results showed highly significant differences between the distributions of [^{68}Ga]Ga-PSMA-11 and ^{18}F-PSMA-1007. Specifically, SUV$_{max}$ ($p<0.0001$), SUV$_{peak}$ ($p<0.0001$), and SUV$_{mean}$ ($p<0.0001$) were higher for ^{18}F-PSMA-1007 than for [^{68}Ga]Ga-PSMA-11 (Figure 3).

T/B

T/B ratio distributions differed significantly ($p<0.0001$), with [^{68}Ga]Ga-PSMA-11 exhibiting higher mean and median values than ^{18}F-PSMA-1007 (Figure 4, left two datasets).

MTV

There was no significant difference in MTV distributions between [^{68}Ga]Ga-PSMA-11 and ^{18}F-PSMA-1007 ($p>0.05$; Figure 4, middle two datasets).

TL-PSMA

Significant differences were found in TL-PSMA distributions ($p=0.0063$), with [^{68}Ga]Ga-PSMA-11 exhibiting higher median and lower mean values compared to ^{18}F-PSMA-1007 Figure 4 (right 2 datasets).

%COV

Results indicated greater variability in [^{68}Ga]Ga-PSMA-11 distributions than in ^{18}F-PSMA-1007 for suspected lesion SUV (irrespective of normalisation), liver SUV$_{mean}$, and T/B. However, %COV for ^{18}FPSMA-1007 was higher for remaining liver SUV, MTV, and TL-PSMA volume estimations (Figure 5).

Discussion

Our centre initially used the widely available [^{68}Ga]Ga-PSMA-11 for prostate cancer imaging on PET/CT. However, logistical supply challenges, combined with substantially increased demand for scans led to long national delays in service delivery. As a result, together with others, we introduced ^{18}F-PSMA-1007 to address the backlog, and we now primarily use this imaging agent. The difference

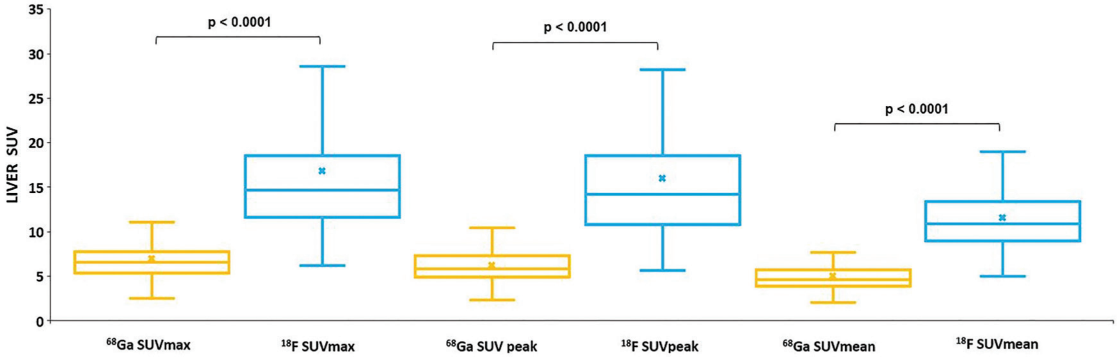

Figure 3. Background liver SUV$_{mean}$ distributions in [^{68}Ga]Ga-PSMA-11 and ^{18}F-PSMA-1007 PET scans

SUV$_{mean}$: Mean standardized uptake, PSMA: Prostate specific membrane antigen, PET: Positron emission tomography, SUVmax: Maximum standard uptake values, SUVpeak: Standardized uptake value-peak

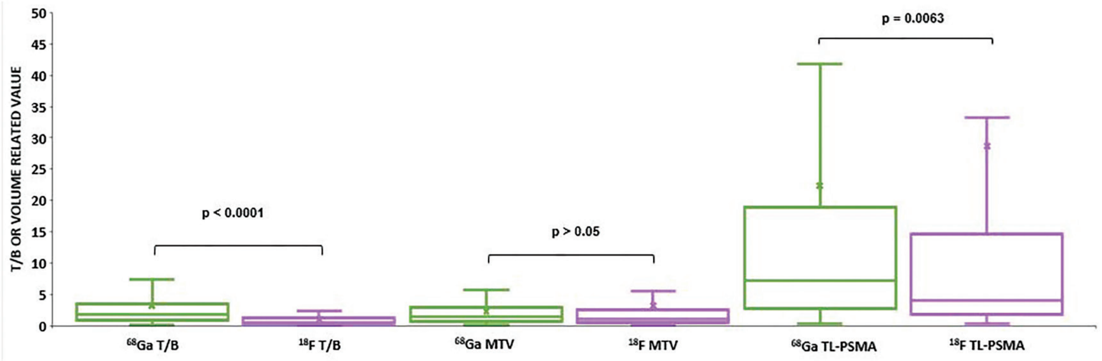

Figure 4. T/B, MTV and TL-PSMA distributions in [^{68}Ga]Ga-PSMA-11 and ^{18}F-PSMA-1007 PET scans

TL-PSMA: Total lesion prostate specific membrane antigen, PET: Positron emission tomography, T/B: Tumor-to-background, MTV: Metabolic tumor volume

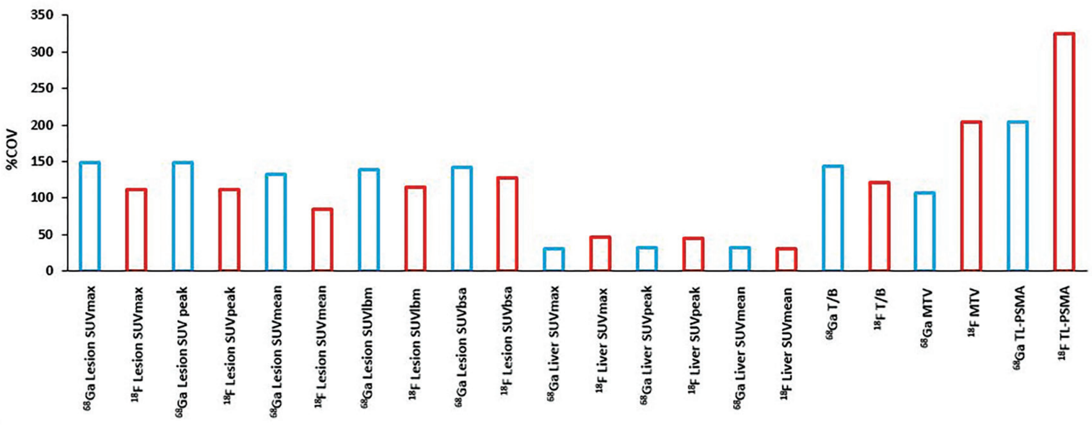

Figure 5. %COV of different parameters in [^{68}Ga]Ga-PSMA-11 and ^{18}F-PSMA-1007 PET scans

PSMA: Prostate specific membrane antigen, PET: Positron emission tomography

in cohort sizes in our study reflected the limited number of ^{68}Ga PSMA patients scanned before the introduction of our ^{18}F-PSMA service. The identical but larger number of lesions selected between tracers was intended to ensure good statistics by maximising the use of the available scan data. Lesions were selected directly from reports. It is recognised that injected activity regimes and uptake times differed between tracers, but each was optimised for service delivery and, accordingly, their differences were significant. Nevertheless, these logistical issues do not impact the efficacy of this study, as the same protocols were used throughout for each tracer and the study was performed on a single machine. Indeed, many centres routinely exchange these imaging agents to optimise service delivery when tracer supply is compromised, taking these considerations into account.

Despite the potential for interchangeability of [^{68}Ga]Ga-PSMA-11 and ^{18}F-PSMA-1007 imaging agents in clinical practice (17), relatively few studies have conducted direct, matched comparisons (18,19). Furthermore, publications often compare different clinical metrics of efficacy (20), including qualitative interpretations. We characterise PSMA uptake of [^{68}Ga]Ga-PSMA-11 and ^{18}F-PSMA-1007, focusing on quantitative SUV, T/B, and volume-surrogate differences when these tracers are interchanged due to supply issues.

Suspected lesion SUV

In this study, significant differences were observed between the two tracers in SUV_{max}, SUV_{peak}, SUV_{mean}, SUV_{lbm}, and SUV_{bsa}, with [^{68}Ga]Ga-PSMA-11 showing higher values (Figures 1, 2). However, in a different consecutive-scan PSMA study using ^{18}F-PSMA-1007 and [^{68}Ga]Ga-PSMA-11 (21) with 46 patients, no significant differences were seen in median SUV_{max} or SUV_{peak} for suspected prostate, lymph nodes, or metastatic bone disease. Similarly, no significant differences were observed in the median SUV_{max} between radiopharmaceuticals in another biopsy-proven study of

40 patients (22). Alternatively, in a separate study (17) of 16 patients, the median SUV$_{max}$ of primary prostate lesions was greater for ^{18}F-PSMA-1007 than for [^{68}Ga]Ga-PSMA-11 (p=0.002).

Differences in results between studies may highlight variability in study design, patient recruitment, disease stage, acquisition protocols, reversibility of kinetics in organs/lesions (23), and various analysis techniques. Therefore, these issues should be considered when comparing studies and drawing conclusions.

Liver SUV

Our results showed that the ^{18}F-PSMA-1007 SUV$_{mean}$ of normal liver background tissue was significantly higher than the corresponding value for [^{68}Ga]Ga-PSMA-11 (Figure 3), and this outcome agreed with other studies (24). As such, interchanging imaging agents would affect T/B ratios when the liver is chosen as the background. Conversely, differences are predictable, and it may be possible to derive a correction factor between interchanged radiopharmaceuticals if patient selection T/B criteria are met.

T/B

Our results (Figure 4) showed that [^{68}Ga]Ga-PSMA-11 exhibited significantly higher mean and median lesion-to-liver ratio values compared with [^{18}F]PSMA-1007, resulting in a [^{68}Ga]Ga-PSMA-11 mean T/B approximately 3 times that of ^{18}F-PSMA-1007.

However, others have noted that when the spleen (21,24,25) is used for background, ^{18}F-PSMA-1007 uptake is much higher than liver ^{68}Ga uptake, and the range is greater for ^{18}F-PSMA-1007 and [^{68}Ga]Ga-PSMA-11 compared with hepatic PSMA uptake. Another study (17) reported that background median SUV$_{max}$ was greater for ^{18}F-PSMA-1007 than for [^{68}Ga]Ga-PSMA-11 in the gluteus maximus (p=0.001) and in the blood pool (p=0.001). They showed no significant differences in any T/B ratios between imaging agents. Similarly, consideration of these issues is recommended when comparing studies and drawing conclusions, especially regarding patient selection criteria in trials.

This challenge also applies to the VISION prostate cancer trial, in which patients with metastatic castration-resistant prostate cancer received ^{177}Lu-PSMA-617 therapy. One eligibility criterion was a PSMA-positive [^{68}Ga]Ga-PSMA-11 PET/CT scan, defined by a lesion-to-liver uptake ratio >1. In our study, this suggested 150 of the 200 [^{68}Ga]Ga-PSMA-11patients (i.e. 75%) would be eligible ideally if all other criteria were met. Hypothetically, if the VISION study [^{68}Ga]Ga-PSMA-11 patient-selection criterion (T/B >1) were applied to our ^{18}F-PSMA-1007 T/B data, this would imply that 62 of the 200 ^{18}F-PSMA-1007 therapy patients (31%) would be eligible. This represents a 59% difference between the tracers at the same [^{68}Ga]Ga-PSMA-11 T/B ratio threshold. However, it is acknowledged that different biodistributions predominate, and that the refined VISION trial therapy eligibility conditions differed from the broader standard-of-care requirements under which scans were acquired here. These differences highlight the need for careful consideration and caution when tracers are interchanged, for example, due to supply issues.

Furthermore, in our study, we observed significant differences in lesion SUV, liver SUV, T/B, and TL-PSMA between tracers, with mean ± SD values presented in Table 1. However, one must exercise caution when making direct comparisons between tracers using such metrics because bias may influence the results. Knowledge of all influencing factors is essential for a fully valid assessment of clinical efficacy, including tumour stage, recurrence, PSA, injected activity, acquisition protocols, image reconstruction techniques, sample size, and treatments, among others. Reviews in this area (26) have shown that [^{68}Ga]Ga-PSMA-11 exhibits high urinary tract excretion and may complicate the diagnosis of small lesions near the prostate bed or bladder. While ^{18}F-PSMA-1007 is dominated by hepatobiliary excretion with potential for improved ability to identify lesions in the pelvic region. Moreover, others have shown that the sensitivity of [^{68}Ga]Ga-PSMA-11 may be slightly lower than that of [^{18}F]PSMA-1007 for detecting small lesions or at very low PSA levels. [^{68}Ga]Ga-PSMA-11 may benefit from a lower false-positive rate in bone and ganglia compared with [^{18}F]PSMA-1007.

Table 1. Mean with standard deviation of some parameters investigated which demonstrated significant difference

	Mean ± SD	Tracer
Lesion	14.23±21.14	[^{68}Ga]Ga-PSMA-11
SUV$_{max}$	10.2±11.37	^{18}F-PSMA-1007
Lesion	7.44±9.87	[^{68}Ga]Ga-PSMA-11
SUV$_{mean}$	5.51±4.68	^{18}F-PSMA-1007
Liver	5.02±1.59	[^{68}Ga]Ga-PSMA-11
SUV$_{mean}$	11.57±3.53	^{18}F-PSMA-1007
T/B	3.24±4.65	[^{68}Ga]Ga-PSMA-11
	1.01±1.22	^{18}F-PSMA-1007
TLG	22.31±45.7	[^{68}Ga]Ga-PSMA-11
	28.75±93.26	^{18}F-PSMA-1007

SUV$_{max}$: Maximum standard uptake values, SUV$_{mean}$: Maximum standard uptake values, T/B: Tumor-to-background, TLG: Total lesion glycolysis, SD: Standard deviation, PSMA: Prostate specific membrane antigen

Although differences in results are seen in many published studies, and some are contradictory, the consensus is that both tracers exhibit comparable diagnostic performance in the clinical setting. Local validation of equivalence in tracer exchange is highly recommended to ensure that any departure from expectations is understood. Caution is also advised in clinical trials, particularly if patient recruitment is based on retrospective standard-of-care scans involving, for example, the lesion T/B ratio.

MTV and TL-PSMA

In this study, no significant difference was recorded in MTV between tracers. Estimation of MTV arises from a convolution of factors, including the software algorithm used to derive it, lesion SUV_{max}, lesion homogeneity or heterogeneity, and neighbouring tissue uptake. With this understanding, the MTV was not statistically significant in our case.

The TL-PSMA is estimated as the product of MTV and lesion SUV_{mean}. In our case, the lesion SUV_{mean} was significantly different between tracers. A Higher lesion SUV_{mean} associated with [^{68}Ga]Ga-PSMA-11, compared with ^{18}F-PSMA-1007, likely contributed to this result. Supporting this, another 42-patient study found that a significant difference in TL-PSMA between tracers enabled the prediction of a high Gleason score in favour of ^{18}F-PSMA-1007 (27).

%COV

We presented diverse %COV results across the quantitative parameters investigated, implying the absence of overall superiority of either PSMA imaging agent. In all cases, the %COV for background liver revealed that ^{18}F-PSMA-1007 was higher than [^{68}Ga]Ga-PSMA-11, while for suspected lesions [^{68}Ga]Ga-PSMA-11 was higher than ^{18}F-PSMA-1007; across parameters studied, the %COV for suspected lesions was higher than that for liver. These findings also confirm results reported by others (24).

In summary, for our entire study, we characterised ^{18}F-PSMA-1007 and [^{68}Ga]Ga-PSMA-11 PET PSMA-suspected lesion SUV, background liver SUV, T/B ratios, and %COV at our centre, and demonstrated that quantitative PET measurements are of the same order of magnitude, while quantitative differences are generally consistent and predictable. Our results, obtained using these imaging agents, support their interchangeability during supply shortages and are consistent with other studies, e.g. (4). We also provide further support for the existing evidence base that supports the national regulatory approval of PET PSMA imaging agents, such as ^{18}F-PSMA-1007, in France in 2021 (28). Indeed, NHS England in 2025 recognised this necessity with commissioning policy approval for PSMA PET e.g. [^{68}Ga]Ga-PSMA-11 and ^{18}F-PSMA-1007 in prostate cancer to ameliorate tracer availability challenges (29).

However, important caveats must be considered when exchanging tracers, particularly in applications such as PSMA radioligand therapy (30,31), including more recent [^{161}Tb]Tb-PSMA (32) and [^{225}Ac]Ac-PSMA (33), where patient therapy selection using T/B ratios may be influenced by individual variations in radiopharmaceutical biodistribution, tissue uptake, and, particularly, background selection.

Study Limitations

This was a single-centre retrospective audit in which all suspicious lesions were identified by reporting radiologists as part of standard-of-care practice. We included all suspected prostate cancer referrals and analysed clinically reported suspected lesions to provide a more realistic system-level quantitative characterization, rather than identifying specific tumour types or sites for analysis, because of the possibility of reduced statistical power. Similarly, PSA levels were not included in reports, and were therefore unavailable for this audit. However, the interchange of tracers is vital for many centres to maintain delivery of prostate cancer imaging services throughout the patient pathway, irrespective of PSA levels, because national demand for diagnosis remains very high. Other constraints in this study include the lack of histological confirmation; therefore, we refer to suspected lesions. Patient cohorts received one radiopharmaceutical but not the other, limiting the ability to make a fully matched comparison. Although hepatic lesions were excluded from the analysis, residual bias may remain in cases where clinicians could not visually identify such lesions. However, scans were interpreted by trained radiologists, and experienced PET physicists conducted data analysis to ensure the validity of the findings.

Overall, we believe that we have satisfied the quantitative case for interchange between [^{68}Ga]Ga-PSMA-11 and ^{18}F-PSMA-1007 tracers for routine use in referrals for suspected prostate cancer, and we support national recommendations that advocate PET PSMA.

Conclusion

We characterised significant differences in [^{68}Ga]Ga-PSMA-11 and ^{18}F-PSMA-1007 PET PSMA suspected prostate cancer patients for suspected lesion SUV_{max} (p=0.0004), SUV_{peak} (p=0.0017), SUV_{mean} (p=0.0007), SUV_{lbm} (p=0.0002) and SUV_{bsa} (p=0.0005) with higher [^{68}Ga]Ga-PSMA-11 values. Similarly, for background liver, we confirmed higher SUV_{max} (p<0.0001), SUV_{peak} (p<0.0001), and SUV_{mean}

($p<0.0001$) with ^{18}F-PSMA-1007. We also identified significant differences in T/B ($p<0.0001$) and in TL-PSMA ($p=0.0063$). Our results favour adopting these PSMA tracers for routine clinical use in PET for prostate cancer and further support the new NHS England commissioning policy.

Ethics

Ethics Committee Approval: This study was conducted as an anonymised audit and as such ethics was not required.

Informed Consent: This study was conducted as an anonymised audit and as such informed consent was not required.

Footnotes

Authorship Contributions

Concept: B.S., G.L., S.S., W.L.W., Design: B.S., G.L., S.S., W.L.W., Data Collection or Processing: B.S., G.L., S.S., W.L.W., Analysis or Interpretation: B.S., G.L., S.S., W.L.W., Literature Search: B.S., G.L., S.S., W.L.W., Writing: B.S., G.L., S.S., W.L.W.z

Conflict of Interest: No conflict of interest was declared by the authors.

Financial Disclosure: The authors declared that this study has received no financial support.

References

1. Tan EH, Burn E, Barclay NL, Delmestri A, Man WY, Golozar A, Serrano ÀR, Duarte-Salles T, Cornford P, Prieto Alhambra D, Newby D; OPTIMA Consortium. Incidence, prevalence, and survival of prostate cancer in the UK. JAMA Netw Open. 2024;7:e2434622.
2. Shen K, Liu B, Zhou X, Ji Y, Chen L, Wang Q, Xue W. The evolving role of ^{18}F-FDG PET/CT in diagnosis and prognosis prediction in progressive prostate cancer. Front Oncol. 2021;11:683793.
3. Ilhan H, Royce T, Qiu X, Zamboglou C. Editorial: exploring the potential of PSMA-PET imaging on personalized prostate cancer treatment. Front Oncol. 2022;12:832747.
4. Huang S, Ong S, McKenzie D, Mirabelli A, Chen DC, Chengodu T, Murphy DG, Hofman MS, Lawrentschuk N, Perera M. Comparison of ^{18}F-based PSMA radiotracers with [^{68}Ga]Ga-PSMA-11 in PET/CT imaging of prostate cancer-a systematic review and meta-analysis. Prostate Cancer Prostatic Dis. 2024;27:654-664.
5. Giunta EF, Brighi N, Gurioli G, Matteucci F, Paganelli G, De Giorgi U. ^{177}Lu-PSMA therapy in metastatic prostate cancer: an updated review of prognostic and predictive biomarkers. Cancer Treat Rev. 2024;125:102699.
6. Rowe SP, Buck A, Bundschuh RA, Lapa C, Serfling SE, Derlin T, Higuchi T, Gorin MA, Pomper MG, Werner RA. [^{18}F]DCFPyL PET/CT for imaging of prostate cancer. Nuklearmedizin. 2022;61:240-246.
7. Vázquez SM, Endepols H, Fischer T, Tawadros SG, Hohberg M, Zimmermanns B, Dietlein F, Neumaier B, Drzezga A, Dietlein M, Schomäcker K. Translational development of a Zr-89-labeled inhibitor of prostate-specific membrane antigen for PET imaging in prostate cancer. Mol Imaging Biol. 2022;24:115-125.
8. Naik M, Khan SR, Lewington V, Challapalli A, Eccles A, Barwick TD. Imaging and therapy in prostate cancer using prostate specific membrane antigen radioligands. Br J Radiol. 2024;97:1391-1404.
9. Rosar F, Burgard C, David S, Marlowe RJ, Bartholomä M, Maus S, Petto S, Khreish F, Schaefer-Schuler A, Ezziddin S. Dual FDG/PSMA PET imaging to predict lesion-based progression of mCRPC during PSMA-RLT. Sci Rep. 2024;14:11271.
10. Wang Q, Ketteler S, Bagheri S, Ebrahimifard A, Luster M, Librizzi D, Yousefi BH. Diagnostic efficacy of [^{99m}Tc]Tc-PSMA SPECT/CT for prostate cancer: a meta-analysis. BMC Cancer. 2024;24:982.
11. Aksu A, Çapa Kaya G. Is SUV Corrected for lean body mass superior to SUV of body weight in ^{68}Ga-PSMA PET/CT? Mol Imaging Radionucl Ther. 2021;30:144-149.
12. Bela Andela S, Amthauer H, Furth C, Rogasch JM, Beck M, Mehrhof F, Ghadjar P, van den Hoff J, Klatte T, Tahbaz R, Zips D, Hofheinz F, Zschaeck S. Quantitative PSMA-PET parameters in localized prostate cancer: prognostic and potential predictive value. Radiat Oncol. 2024;19:97.
13. Sartor O, de Bono J, Chi KN, Fizazi K, Herrmann K, Rahbar K, Tagawa ST, Nordquist LT, Vaishampayan N, El-Haddad G, Park CH, Beer TM, Armour A, Pérez-Contreras WJ, DeSilvio M, Kpamegan E, Gericke G, Messmann RA, Morris MJ, Krause BJ; VISION investigators. lutetium-177-PSMA-617 for metastatic castration-resistant prostate cancer. N Engl J Med. 2021;385:1091-1103.
14. Kuo PH, Benson T, Messmann R, Groaning M. Why we did what we did: PSMA PET/CT selection criteria for the VISION Trial. J Nucl Med. 2022;63:816-818.
15. Cook GJR, Wong WL, Sanghera B, Mangar S, Challapalli A, Bahl A, Bassett P, Leaning D, Schmidkonz C. Eligibility for ^{177}Lu-PSMA therapy depends on the choice of companion diagnostic tracer: a comparison of ^{68}Ga-PSMA-11 and ^{99m}Tc-MIP-1404 in metastatic castration-resistant prostate cancer. J Nucl Med. 2023;64:227-231.
16. Ahmadzadehfar H, Seifert R, Afshar-Oromieh A, Kratochwil C, Rahbar K. Prostate cancer theranostics with ^{177}Lu-PSMA. Semin Nucl Med. 2024;54:581-590.
17. Kuten J, Fahoum I, Savin Z, Shamni O, Gitstein G, Hershkovitz D, Mabjeesh NJ, Yossepowitch O, Mishani E, Even-Sapir E. Head-to-head comparison of ^{68}Ga-PSMA-11 with ^{18}F-PSMA-1007 PET/CT in staging prostate cancer using histopathology and immunohistochemical analysis as a reference standard. J Nucl Med. 2020;61:527-532.
18. Evangelista L, Maurer T, van der Poel H, Alongi F, Kunikowska J, Laudicella R, Fanti S, Hofman MS. [^{68}Ga]Ga-PSMA versus [^{18}F]PSMA positron emission tomography/computed tomography in the staging of primary and recurrent prostate cancer. A systematic review of the literature. Eur Urol Oncol. 2022;5:273-282.
19. De Man K, Van Laeken N, Schelfhout V, Fendler WP, Lambert B, Kersemans K, Piron S, Lumen N, Decaestecker K, Fonteyne V, Delrue L, De Vos F, Ost P. ^{18}F-PSMA-11 versus ^{68}Ga-PSMA-11 positron emission tomography/computed tomography for staging and biochemical recurrence of prostate cancer: a prospective double-blind randomised cross-over trial. Eur Urol. 2022;82:501-509.
20. Hoffmann MA, Müller-Hübenthal J, Rosar F, Fischer N, von Eyben FE, Buchholz HG, Wieler HJ, Schreckenberger M. Primary staging of prostate cancer patients with [^{18}F]PSMA-1007 PET/CT compared with [^{68}Ga]Ga-PSMA-11 PET/CT. J Clin Med. 2022;11:5064.
21. Hoberück S, Löck S, Borkowetz A, Sommer U, Winzer R, Zöphel K, Fedders D, Michler E, Kotzerke J, Kopka K, Hölscher T, Braune A. Intraindividual comparison of [^{68} Ga]-Ga-PSMA-11 and [^{18}F]-F-PSMA-1007 in prostate cancer patients: a retrospective single-center analysis. EJNMMI Res. 2021;11:109.
22. Chandekar KR, Singh H, Kumar R, Kumar S, Kakkar N, Mittal BR, Singh SK. Comparison of 18 F-PSMA-1007 PET/CT with 68 Ga-PSMA-11 PET/CT for initial staging in intermediate- and high-risk prostate cancer. Clin Nucl Med. 2023;48:e1-e8.
23. Dias AH, Jochumsen MR, Zacho HD, Munk OL, Gormsen LC. Multiparametric dynamic whole-body PSMA PET/CT using [^{68}Ga]Ga-PSMA-11 and [^{18}F]PSMA-1007. EJNMMI Res. 2023;13:31.

24. Popescu CE, Zhang B, Sartoretti T, Spielhofer N, Skawran S, Heimer J, Messerli M, Sauter A, Huellner MW, Kaufmann PA, Burger IA, Maurer A. Evaluating the biodistribution for [^{68}Ga]Ga-PSMA-11 and [^{18}F]F-PSMA-1007 PET/CT with an inter- and intrapatient based analysis. EJNMMI Res. 2024;14:36.

25. Seifert R, Telli T, Hadaschik B, Fendler WP, Kuo PH, Herrmann K. Is ^{18}F-FDG PET needed to assess ^{177}Lu-PSMA therapy eligibility? A VISION-like, single-center analysis. J Nucl Med. 2023;64:731-737.

26. Abdi N, Alsulami M, Ghaznavi H. Comparing the diagnostic performance of [^{18}F]PSMA-1007 with [^{68}Ga]Ga-PSMA-11 in PET/CT imaging and staging of recurrent prostate cancer. Med Adv. 2025;3:9-19.

27. Pizzuto DA, Guerreri M, Zamboglou C, Boldrini L, Gatta R, Ruggierro M, De Summa M, Caldarella C, Annunziata S. The clinical predictive value of radiomic features from [^{68}Ga]Ga-PSMA-11 and [^{18}F]F-PSMA-1007 PET in patients with prostate cancer: a preliminary comparative study. Clin Transl Imaging 2024;12:629-638.

28. (ANSM) Andsdmedpds. Protocole D'utilisation therapeutique et de Recueil D'informations ABX-PSMA-1007, 1300 MBq/mL solution injectable, substance active: [^{18}F]PSMA-1007. 2010. Available from: http://agence-prd.ansm.sante.fr/php/ecodex/extrait.php?specid=64034289.

29. Public Health Evidence Report 2307. Prostate-specific membrane antigen (PSMA) radiotracers in positron emission tomography – computed tomography (PETCT) imaging for individuals with high-risk primary or recurrent prostate cancer (adults). (2025, February). NHS England.

30. Kind F, Eder AC, Jilg CA, Hartrampf PE, Meyer PT, Ruf J, Michalski K. Prognostic value of tumor volume assessment on PSMA PET After ^{177}Lu-PSMA radioligand therapy evaluated by PSMA PET/ct consensus statement and RECIP 1.0. J Nucl Med. 2023;64:605-610.

31. Fendler WP, Eiber M, Beheshti M, Bomanji J, Calais J, Ceci F, Cho SY, Fanti S, Giesel FL, Goffin K, Haberkorn U, Jacene H, Koo PJ, Kopka K, Krause BJ, Lindenberg L, Marcus C, Mottaghy FM, Oprea-Lager DE, Osborne JR, Piert M, Rowe SP, Schöder H, Wan S, Wester HJ, Hope TA, Herrmann K. PSMA PET/CT: joint EANM procedure guideline/SNMMI procedure standard for prostate cancer imaging 2.0. Eur J Nucl Med Mol Imaging. 2023;50:1466-1486.

32. Abdlkadir AS, Rosar F, Jalilian A, Moghrabi S, Al-Balooshi B, Rabei O, Kairemo K, Al-Ibraheem A. Harnessing terbium radioisotopes for clinical advancements: a systematic review. Nucl Med Mol Imaging. 2025;59:50-61.

33. Sathekge MM, Lawal IO, Bal C, Bruchertseifer F, Ballal S, Cardaci G, Davis C, Eiber M, Hekimsoy T, Knoesen O, Kratochwil C, Lenzo NP, Mahapane J, Maserumule LC, Mdlophane AH, Mokoala KMG, Ndlovu H, Pant V, Rathke H, Reed J, Sen IB, Singh A, Sood A, Tauber R, Thakral P, Yadav MP, Morgenstern A. Actinium-225-PSMA radioligand therapy of metastatic castration-resistant prostate cancer (WARMTH Act): a multicentre, retrospective study. Lancet Oncol. 2024;25:175-183.

Interesting Image

Mol Imaging Radionucl Ther 2026;35(1):44-46 ***DOI:****10.4274/mirt.galenos.2025.78736*

Aortic Calcifications Mimicking Lymph Nodes on ^{18}F-PSMA1007 PET

^{18}F-PSMA1007 PET'te Lenf Düğümlerini Taklit Eden Aort Kalsifikasyonları

Salah Nabih Oueriagli, Omar Ait Sahel, Ikram Zahfir, Meryem Aboussabr, Yassir Benameur,
Abderrahim Doudouh

Mohammed V Military Teaching Hospital, Clinic of Nuclear Medicine, Rabat, Morocco

Abstract

An 82-year-old patient with high-risk prostate adenocarcinoma, previously treated with radiotherapy and hormone therapy, presented with biochemical recurrence, as evidenced by a prostate-specific antigen level of 10 ng/mL. A positron emission tomography/computed tomography (PET/CT) scan using ^{18}F-prostate-specific membrane antigen (PSMA) 1007 revealed significant uptake at the prostate apex and multiple hypermetabolic osseous lesions in the sternum and L3, suggestive of local recurrence and metastasis. However, several hypermetabolic foci in the abdominopelvic region raised suspicion for potential involvement of the lumbar-aortic lymph nodes due to their moderate to intense uptake. After further investigation, these findings were attributed to active aortic calcifications. This case highlights a rare cause of false-positive results in ^{18}F-PSMA 1007 PET/CT imaging and underscores the need for additional evaluations, such as abdominopelvic magnetic resonance imaging and renal and phosphocalcic assessments, when such results are suspected.

Keywords: Aortic calcifications, lymph nodes, ^{18}F-PSMA1007

Öz

Daha önce radyoterapi ve hormon tedavisi görmüş, yüksek riskli prostat adenokarsinomu olan 82 yaşındaki bir hastada, 10 ng/mL'lik prostat spesifik antijen seviyesiyle kanıtlandığı üzere biyokimyasal nüks gözlendi. ^{18}F-prostat-spesifik membran antijeni (PSMA) 1007 kullanılarak yapılan pozitron emisyon tomografisi/bilgisayarlı tomografi (PET/BT) taramasında, prostat apeksinde belirgin tutulum ve sternum ile L3'te lokal nüks ve metastaz düşündüren çok sayıda hipermetabolik kemik lezyonu görüldü. Ancak, abdominopelvik bölgedeki birkaç hipermetabolik odak, orta ila yoğun tutulumları nedeniyle lomber aort lenf düğümlerinin de olası tutulumu şüphesini uyandırdı. Daha ileri incelemeler sonucunda, bu bulgular aktif aort kalsifikasyonlarına bağlandı. Bu olgu, ^{18}F-PSMA 1007 PET/BT görüntülemesinde yanlış pozitif sonuçların nadir görülen bir nedenini vurgulamakta ve bu tür sonuçlardan şüphelenildiğinde abdominopelvik manyetik rezonans görüntüleme ve renal ve fosfokalsi değerlendirmeleri gibi ek değerlendirmelerin gerekliliğini vurgulamaktadır.

Anahtar Kelimeler: Aort kalsifikasyonları, lenf düğümleri, ^{18}F-PSMA1007

Address for Correspondence: Salah Nabih Oueriagli, Mohammed V Military Teaching Hospital, Clinic of Nuclear Medicine, Rabat, Morocco
E-mail: salah.nabihoueriagli@gmail.com **ORCID ID:** orcid.org/0000-0001-7824-3158

Received: 22.04.2025 **Accepted:** 04.07.2025 **Epub:** 01.08.2025 **Publication Date:** 03.02.2026

Cite this article as: Oueriagli SN, Ait Sahel O, Zahfir I, Aboussabr M, Benameur Y, Doudouh A. Aortic calcifications mimicking lymph nodes on ^{18}F-PSMA1007 PET. Mol Imaging Radionucl Ther. 2026;35(1):44-46.

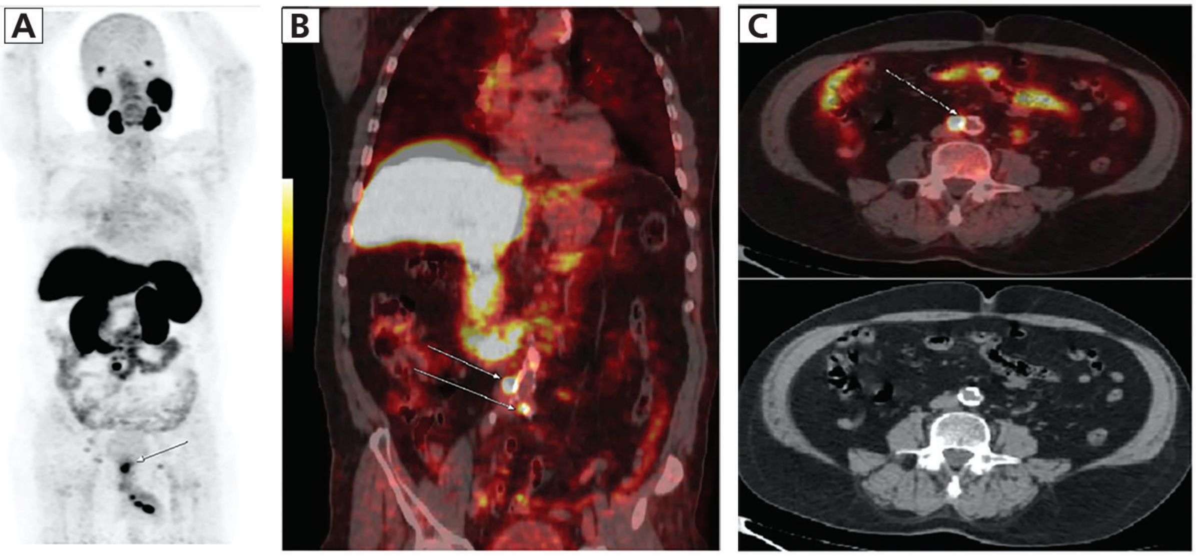

Figure 1. (A) Maximum intensity projection (MIP) of ^{18}F-prostate-specific membrane antigen (PSMA) 1007 positron emission tomography/computed tomography (PET/CT) showing significant uptake at the prostate apex [maximum standardized uptake value (SUV_{max})=12.9], indicating local recurrence (Figure 1). Noted: several hypermetabolic foci in the abdominopelvic region. (B) Fusion image in coronal section showing multiple hypermetabolic foci in the abdominopelvic region (SUV_{max}=3.3-19.5 arrows). These uptakes were attributed to active aortic calcifications. (C) Fusion image in axial section showing an hypermetabolic foci in the lomboaortic bifurcation (SUV_{max}=19.5 arrow). This uptake was also attributed to active aortic calcification. Noted: CT image in axial section showing no suspicious lymphadenopathy.

An 82-year-old man was diagnosed with high-risk prostate cancer (PCa) in 2020 and treated with radiotherapy and hormone therapy. In 2024 the patient had a biochemical recurrence with a prostate-specific antigen (PSA) measured at 10 ng/mL. A PET/CT scan with ^{18}F-PSMA 1007 showed significant uptake at the prostate apex (SUV_{max}=12.9), indicating local recurrence (Figure A arrow). In addition, multiple hypermetabolic osseous lesions were identified in the sternum (SUV_{max}=4.2) and L3 (SUV_{max}=4.7), suggesting osseous metastasis. However, several hypermetabolic foci were also noted on the MIP in the abdominopelvic region (Figure A) raising initial concerns about potential involvement of lumbar-aortic lymph nodes due to the moderate to intensive uptake. These findings were attributed to active aortic calcifications (SUV_{max}=3.3-19.5) (Figures B and C arrows). This aspect was assessed by an abdominopelvic magnetic resonance imaging (MRI), which did not reveal any suspicious lymphadenopathy in the lumbo-aortic region. Additionally, an assessment of calcium-phosphorus balance showed a slightly elevated calcium at 110 mg/dL (normal value: 90-105 mg/dL), while renal function remained normal.

The application of ^{18}F-PSMA-1007 PET/CT in imaging of PCa has significantly improved the detection of PSA relapse and metastasis, especially in patients with high-risk disease (1,2). However, false-positive findings may occur in several cases. Indeed, PSMA is highly expressed in the neovasculature of tumors, both benign and malignant. It plays a regulatory role in both angiogenesis and the expression of vascular growth factors, which are crucial for tumor growth and metastasis (3). This expression is absent in endothelial cells of normal tissues but present in endothelial cells of tumors, leading to PSMA ligand uptake. This allows for the detection of tumor neovasculature in lesions, which can be problematic in non-prostatic tumors, where false-positive findings may occur due to enhanced blood flow and angiogenesis associated with tumor growth. Additionally, inflammation and infection can lead to PSMA expression in immune cells, although the precise mechanisms are not fully understood. Inflammatory conditions, particularly those associated with tissue remodeling and neovascularization, can increase the availability of PSMA ligands at the inflamed site (4). Increased vascular permeability and regional blood flow at sites of infection or inflammation can facilitate PSMA ligand uptake, resulting in false-positive findings on PET scans (5). Galiza Barbosa (5) demonstrated that increased blood flow in inflammatory tissues can lead to misinterpretation of PSMA-PET scans. The uptake of PSMA ligands by calcified vascular structures, such as those in the aorta, can mimic the appearance of malignant lesions on PET scans. Active aortic calcifications can result in elevated SUV_{max} values, as seen in our patient, leading to a mistaken impression of metastatic disease (4). Such findings can be particularly misleading in elderly patients, who are more likely to have atherosclerotic changes and vascular calcifications. Islam et al. (6) further reinforce the importance of recognizing this limitation in PSMA PET/CT imaging. They recommend integrating other imaging modalities, such as CT or MRI, to better characterize ambiguous findings on PET/CT scans. By combining these modalities, clinicians can achieve a more accurate diagnosis, minimizing the risk of false-positive interpretations that could lead to unnecessary biopsies or other invasive procedures (7).

Ethics

Informed Consent: The institutional review board of our institute “Med V Military Teaching Hospital”, approved this publication, and the requirement to obtain informed consent was waived.

Footnotes

Authorship Contributions

Surgical and Medical Practices: S.N.O., Concept: S.N.O., O.A.S., A.D., Design: S.N.O., O.A.S., I.Z., Data Collection or Processing: S.N.O., O.A.S., I.Z., M.A., Analysis or Interpretation: S.N.O., I.Z., M.A., Y.B., A.D., Literature Search: S.N.O., M.A., Writing: S.N.O.

Conflict of Interest: No conflicts of interest were declared by the authors.

Financial Disclosure: The authors declare that this study has received no financial support.

References

1. Afshar-Oromieh A, Babich JW, Kratochwil C, Giesel FL, Eisenhut M, Kopka K, Haberkorn U. The rise of PSMA ligands for diagnosis and therapy of prostate cancer. J Nucl Med. 2016;57:79S-89S.
2. Yordanova A. The role of PSMA PET/CT in prostate cancer: imaging and beyond. Cancer Letters. 2016;382:205-213.
3. Orevi M, Ben-Haim S, Abourbeh G, Chicheportiche A, Mishani E, Yutkin V, Gofrit ON. False positive findings of [^{18}F]PSMA-1007 PET/CT in patients after radical prostatectomy with undetectable serum PSA Levels. Front Surg. 2022;9:943760.
4. Moukaddam H, El Saheb G, Omran N, El Ghawi N, Abi Ghanem A, Haidar M. Case report: positive pitfalls of PSMA PET/CT: diagnostic challenges in degenerative bone lesions including MODIC type 1. Front Nucl Med. 2024;4:1451848.
5. Galiza Barbosa F, Queiroz MA, Nunes RF, Bezerra ROF, Dalaqua M, Gustavo Rocha Resende R, Danil Faria Barbosa Lima E, Kobayashi M, Marins T, Santucci DF, Baroni RH. Nonprostatic diseases on PSMA PET imaging: a spectrum of benign and malignant findings. Cancer Imaging. 2020;20:23.
6. Islam R, Desai S, Moran M, Golombos DM. The role of PSMA PET imaging in prostate cancer: current applications and future directions. Curr Urol Rep. 2025;26:46.
7. Zaman MU, Fatima N, Zaman A, Sajid M, Zaman U, Zaman S. Diagnostic challenges in prostate cancer and ^{68}Ga-PSMA PET imaging: a game changer? Asian Pac J Cancer Prev. 2017;18:2625-2628.

Interesting Image

Mol Imaging Radionucl Ther 2026;35(1):47-50 ***DOI:****10.4274/mirt.galenos.2025.77698*

Unusual Soft Tissue and Muscle Metastases in Papillary Thyroid Carcinoma: Insights from ^{131}I Scintigraphy and ^{18}F-FDG PET/CT

Papiller Tiroid Karsinomunda Olağandışı Yumuşak Doku ve Kas Metastazları: ^{131}I Sintigrafi ve ^{18}F-FDG PET/BT'den Elde Edilen Bulgular

Mohd Fazrin Mohd Rohani, Siti Zarina Amir Hassan

Hospital Kuala Lumpur, Clinic of Nuclear Medicine, Kuala Lumpur, Malaysia

Abstract

Distant metastases from well-differentiated thyroid carcinoma typically involve the lungs and bones. We report a rare case of metastatic papillary thyroid carcinoma presenting as soft tissue lesion, detected by Iodine-131 whole-body scintigraphy in a 44-year-old asymptomatic male. The patient had previously undergone a total thyroidectomy and bilateral modified radical neck dissection, receiving radioiodine for pT3bN1bMx multifocal classical papillary thyroid carcinoma. Further evaluation with ^{18}F-fluorodeoxyglucose positron emission tomography/computed tomography revealed additional sites of soft tissue and muscle metastasis, along with extensive nodal, lung, and skeletal involvement. These findings indicated advanced disease with a poor prognosis, necessitating a change in the treatment plan.

Keywords: Iodine-131, thyroid cancer, ^{18}F-fluorodeoxyglucose positron emission tomography/computed tomography, soft tissue metastasis, muscle metastasis

Öz

İyi farklılaşmış tiroid karsinomundan kaynaklanan uzak metastazlar tipik olarak akciğerleri ve kemikleri etkiler. Kırk dört yaşındaki asemptomatik bir erkekte İyot-131 tüm vücut sintigrafisi ile tespit edilen, yumuşak doku lezyonu olarak ortaya çıkan nadir bir metastatik papiller tiroid karsinomu olgusu sunuyoruz. Hasta daha önce total tiroidektomi ve bilateral modifiye radikal boyun diseksiyonu geçirmiş ve pT3bN1bMx multifokal klasik papiller tiroid karsinomu için radyoiyot tedavisi almıştı. ^{18}F-florodeoksiglukoz pozitron emisyon tomografisi/bilgisayarlı tomografi ile yapılan ileri değerlendirme, yaygın lenf nodu, akciğer ve iskelet tutulumu ile birlikte ek yumuşak doku ve kas metastazı bölgeleri ortaya çıkardı. Bu bulgular, kötü prognozlu ilerlemiş bir hastalığı işaret ediyordu ve tedavi planında değişiklik yapılmasını gerektiriyordu.

Anahtar Kelimeler: İyot-131, tiroid kanseri, ^{18}F-florodeoksiglukoz pozitron emisyon tomografisi/bilgisayarlı tomografi, yumuşak doku metastazı, kas metastazı

Address for Correspondence: Mohd Fazrin Mohd Rohani, Hospital Kuala Lumpur, Clinic of Nuclear Medicine, Kuala Lumpur, Malaysia
E-mail: fazrinrohani@gmail.com **ORCID ID:** orcid.org/0000-0002-8450-0170

Received: 05.04.2025 **Accepted:** 27.07.2025 **Epub:** 11.11.2025 **Publication Date:** 03.02.2026

Cite this article as: Mohd Rohani MF, Amir Hassan SZ. Unusual soft tissue and muscle metastases in papillary thyroid carcinoma: insights from ^{131}I cintigraphy and ^{18}F-FDG PET/CT. Mol Imaging Radionucl Ther. 2026;35(1):47-50.

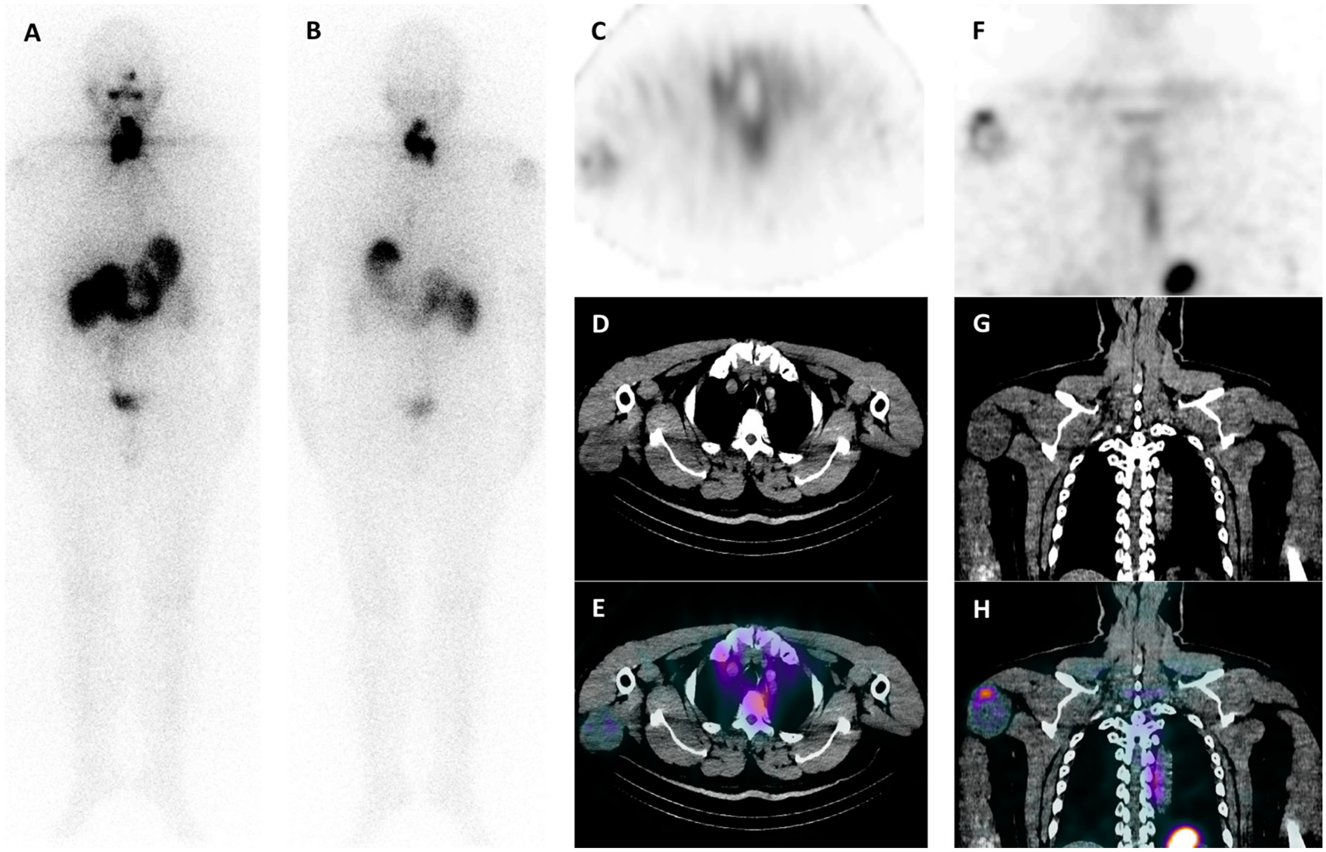

Figure 1. A 44-year-old man received 120 mCi (4440 MBq) of Iodine-131 (^{131}I), 12 weeks after total thyroidectomy and bilateral modified radical neck dissection, for pT3bN1bMx multifocal classical papillary thyroid carcinoma. Histopathology showed extensive lymph node metastases, capsular and vascular invasion, extrathyroidal extension, and lymphovascular permeation of the isthmus. Preoperative contrast-enhanced computed tomography of the neck revealed numerous enlarged bilateral cervical lymph nodes and a right thyroid lesion, without lung or bone metastases. The 120 mCi activity was selected empirically, following institutional protocols and American Thyroid Association guidelines for high-risk differentiated thyroid carcinoma with extensive nodal involvement and possible distant spread. Post-therapy ^{131}I whole-body scintigraphy (A and B) demonstrated multiple foci of increased tracer uptake in the neck and a faint focus in the right posterior shoulder. A subsequent single photon emission computed tomography/ computed tomography of the chest (C, D, and E axial view; F, G, and H coronal view) identified an ^{131}I subcutaneous soft tissue lesion in the right posterior shoulder measuring 4.1x5.9x6.0 cm (AP x W x CC), with no distinct separation from the right triceps muscle. The stimulated (thyroid stimulating hormone >100 mIU/L) serum thyroglobulin (Tg) level prior to ^{131}I therapy was elevated (>5000 ng/mL; normal range 3.5-77 ng/mL), despite a positive anti-Tg antibody, (247.5 IU/mL; normal <115 IU/mL). Biopsy of the shoulder lesion confirmed metastatic papillary thyroid carcinoma.

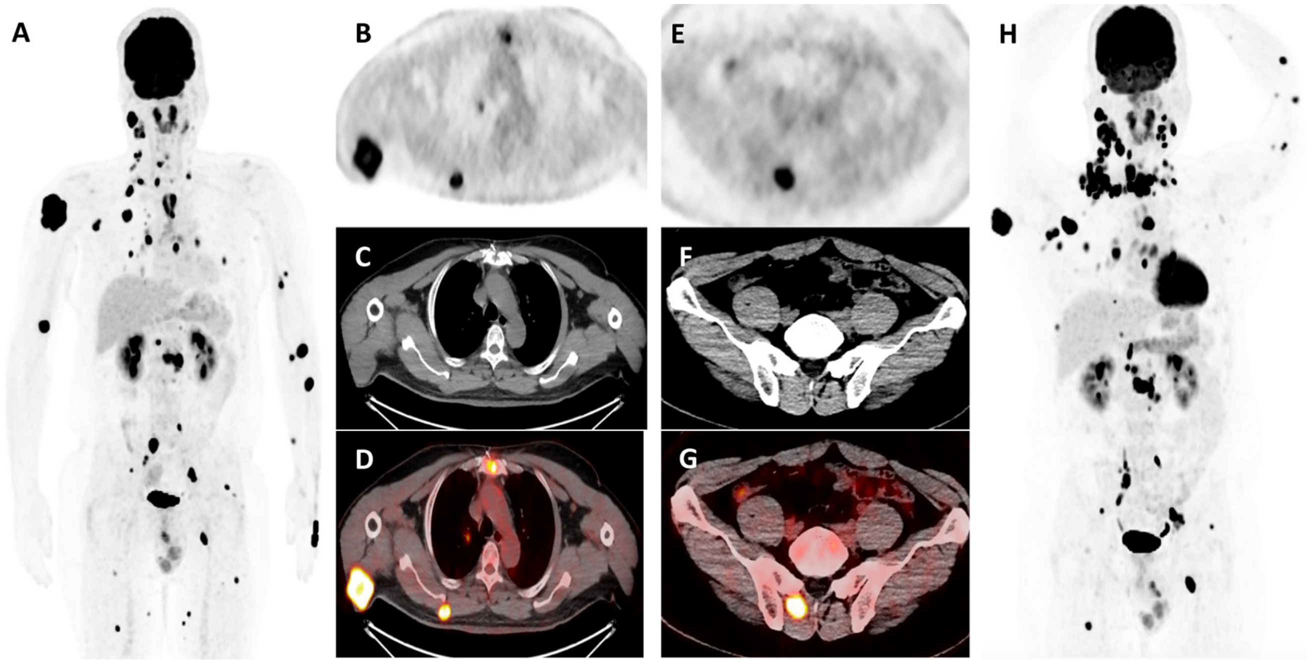

Figure 2. Subsequent ^{18}F-fluorodeoxyglucose positron emission tomography/computed tomography (^{18}F-FDG PET/CT) (A) revealed ^{18}F-FDG-avid malignancy in the thyroid bed with extensive nodal metastases in the neck, chest, and abdomen. Additionally, metastases were identified in the lungs, bones, and soft tissues of the bilateral upper limbs, prominently in the right posterior shoulder (B, C, and D axial view). There was also involvement in muscles, including the right trapezius, right intercostal, bilateral paraspinal, bilateral thigh, and left gluteus, with prominent involvement in the right paraspinal muscle (E, F, and G axial view). Following these findings, radioiodine therapy was discontinued, and the patient began treatment with the tyrosine kinase inhibitor (TKI) lenvatinib. After eight months on lenvatinib, a follow-up ^{18}F-FDG PET/CT demonstrated disease progression, with multiple new ^{18}F-FDG-avid lesions despite some regression in previously noted sites. The initial suppressed serum thyroglobulin (Tg) level was 34.8 ng/mL (thyroid stimulating hormone of 0.19 mIU/L), increasing to 96.8 ng/mL, before TKI initiation, indicating disease progression. Following TKI therapy, suppressed Tg levels decreased to 0.36 ng/mL on later follow-up before rising again to 268.0 ng/mL, suggesting ongoing disease activity.

Distant metastases in differentiated thyroid carcinoma occur in approximately 5% to 10% of cases, typically affecting the lungs and bones (1). Less common sites of dissemination, such as the liver, brain, soft tissue, and muscle, often indicate dedifferentiation of the disease and may arise years after the initial diagnosis (2,3). Soft tissue and muscle metastases from papillary thyroid carcinoma are rare and frequently identified incidentally on imaging due to the asymptomatic nature of most cases (2,4). These metastases generally signify advanced and widely disseminated disease, as in this case (2,4). However, there are reports of solitary soft tissue and muscle metastases in some patients (3,5,6). Soft tissue and skeletal muscle are considered unfavorable environments for tumor proliferation due to factors such as anti-tumor cytokines (e.g., interleukin adenosine and leukemia inhibitory factor); the removal of lactic acid; mechanical disruption of tumor cells; inappropriate pH levels; variable blood flow; and continuous muscle motion (1,2,4,7,8). Nevertheless, soft tissue and muscle metastasis can occur via multiple mechanisms, including intramuscular lymphatic spread, hematogenous dissemination, and perineural transmission (7). In this context, ^{18}F-FDG PET/CT is crucial when serum Tg levels are disproportionately high and do not correlate with Iodine-131 (^{131}I) whole-body scan findings (9). It helps identify iodine-refractory or dedifferentiated lesions, revealing occult metastases not seen on ^{131}I imaging (9,10). In this case, the detection of soft tissue metastasis on ^{131}I whole-body scintigraphy, along with extensive hypermetabolic ^{18}F-FDG-avid lesions in unexpected sites, indicated a poor prognosis and shorter survival (1,2,8,9,10), necessitating a change in treatment strategy.

Ethics

Informed Consent: The patient provided written informed consent.

Footnotes

Authorship Contributions

Surgical and Medical Practices: M.F.M.R., S.Z.A.H., Concept: M.F.M.R., S.Z.A.H., Design: M.F.M.R., S.Z.A.H., Data Collection or Processing: M.F.M.R., S.Z.A.H., Analysis or Interpretation: M.F.M.R., S.Z.A.H., Literature Search: M.F.M.R., S.Z.A.H., Writing: M.F.M.R., S.Z.A.H.

Conflict of Interest: No conflicts of interest were declared by the authors.

Financial Disclosure: The authors declare that this study has received no financial support.

References

1. Hitu L, Cainap C, Apostu D, Gabora K, Bonci EA, Badan M, Mester A, Piciu A. Skeletal muscle metastasis in papillary thyroid microcarcinoma evaluated by F18-FDG PET/CT. Diagnostics (Basel). 2020;10:100.
2. Califano I, Quildrian S, Coduti M, Rojas Bilbao E, Otero J, Califano L. Soft tissue metastases from differentiated thyroid cancer diagnosed by ^{18}F FDG PET-CT. Arq Bras Endocrinol Metabol. 2013;57:317-321.
3. Stephen J, Thomas MB, Thomas MB. A case of papillary thyroid cancer with soft tissue metastasis. Int Surg J. 2018;5:3425-3429.
4. Qiu ZL, Luo QY. Erector spinae metastases from differentiated thyroid cancer identified by I-131 SPECT/CT. Clin Nucl Med. 2009;34:137-140.
5. Ceriani L, Treglia G, Paone G, Bongiovanni M, Franscella S, Giovanella L. Unusual muscular metastases from papillary thyroid carcinoma detected by fluorine-18-fluorodeoxyglucose PET/MRI. J Clin Endocrinol Metab. 2013;98:2208-2209.
6. Tunio MA, Alasiri M, Riaz K, Alshakwer W, Alarifi M. Skeletal muscle metastasis as an initial presentation of follicular thyroid carcinoma: a case report and a review of the literature. Case Rep Endocrinol. 2013;2013:192573. Epub 2013 Mar 28.
7. Shin T, Hoang TD, Shane SP, Mai VQ, Shakir MKM. Multi-focal metastatic papillary thyroid cancer to skeletal muscle with BRAFV600E mutation. Trends Med. 2020;20:2-3.
8. Sarma M, Sonik B, Subramanyam P, Sundaram PS. Isolated skeletal muscle metastatic deposit in a patient with micropapillary carcinoma thyroid identified by ^{18}F FDG PET CT. J Egypt Natl Canc Inst. 2015;27:47-50.
9. Herbowski L. Skeletal muscle metastases from papillary and follicular thyroid carcinomas: an extensive review of the literature. Oncol Lett. 2018;15:7083-7089.
10. Stergioula A, Pantelis E, Kormas T, Agrogiannis G. Case report: skeletal muscle metastasis from follicular thyroid carcinoma presenting as synovial sarcoma. Front Oncol. 2023;13:994729.

Interesting Image

Mol Imaging Radionucl Ther 2026;35(1):51-54 ***DOI:****10.4274/mirt.galenos.2025.58265*

Truncation Artifact Presenting as Cropped Projections and Wedge Defect in Sinogram During Single-Photon Emission Computed Tomography

Tek Foton Emisyonlu Bilgisayarlı Tomografi Sırasında Sinogramda Kırpılmış Projeksiyonlar ve Kama Kusuru Olarak Ortaya Çıkan Trunkasyon Artefaktı

Mohsen Qutbi[1], Reyhane Ahmadi[2], Amirmohammad Alinejad[1]

[1]*Shahid Beheshti University of Medical Sciences Faculty of Medicine, Department of Nuclear Medicine, Tehran, Iran*
[2]*Hamadan University of Medical Sciences Faculty of Medicine, Farshchian Heart Center, Department of Nuclear Medicine and Molecular Imaging, Hamadan, Iran*

Abstract

Truncation artifact during single-photon emission computed tomography occurs when some part of body, such as left ventricle in myocardial perfusion imaging, lies outside the field-of-view during image acquisition. Improper adjustment of axis of rotation of detectors regarding the patient on the scanning table is the main cause. Large or slim patient body habitus is reported as source of this artifact. However, there may be other sources including that in our case, in which the artifact was present in prone position but not in supine imaging. The appearance was one-sided incremental cropping of projections of one of detectors and a wedge-shaped or triangular defect in the corresponding sinogram. This finding may suggest a possible mechanical instability of the gantry during motion over the patient's left side in prone imaging.

Keywords: Truncation artifact, single-photon emission computed tomography, myocardial perfusion imaging

Öz

Tek foton emisyonlu bilgisayarlı tomografi sırasında trunkasyon artefaktı, miyokard perfüzyon görüntülemesinde sol ventrikül gibi vücudun bir bölümünün görüntü alımı sırasında görüş alanının dışında kalması durumunda ortaya çıkar. Tarama masasında hastaya göre dedektörlerin dönüş ekseninin yanlış ayarlanması ana nedendir. Bu artefaktın kaynağı olarak hastanın vücut yapısının büyük veya ince olması bildirilmektedir. Ancak, bizim olgumuzda olduğu gibi, artefaktın yüzüstü pozisyonda mevcut olduğu ancak sırtüstü görüntülemede mevcut olmadığı başka kaynaklar da olabilir. Görünüm, dedektörlerden birinin projeksiyonlarının tek taraflı artımlı kırpılması ve ilgili sinogramda kama şeklinde veya üçgen bir defektti. Bu bulgu, yüzüstü görüntülemede hastanın sol tarafı üzerinde hareket ederken gantrinin olası bir mekanik instabilitesini düşündürebilir.

Anahtar kelimeler: Trunkasyon artefaktı, tek foton emisyonlu bilgisayarlı tomografi, miyokard perfüzyon görüntüleme

---

Address for Correspondence: Mohsen Qutbi, Shahid Beheshti University of Medical Sciences Faculty of Medicine, Department of Nuclear Medicine, Tehran, Iran
E-mail: mohsen.qutbi@gmail.com **ORCID ID:** orcid.org/0000-0002-8347-605X

Received: 30.08.2024 **Accepted:** 03.08.2025 **Epub:** 11.11.2025 **Publication Date:** 03.02.2026

Cite this article as: Qutbi M, Ahmadi R, Alinejad A. Truncation artifact presenting as cropped projections and wedge defect in sinogram during single-photon emission computed tomography. Mol Imaging Radionucl Ther. 2026;35(1):51-54.

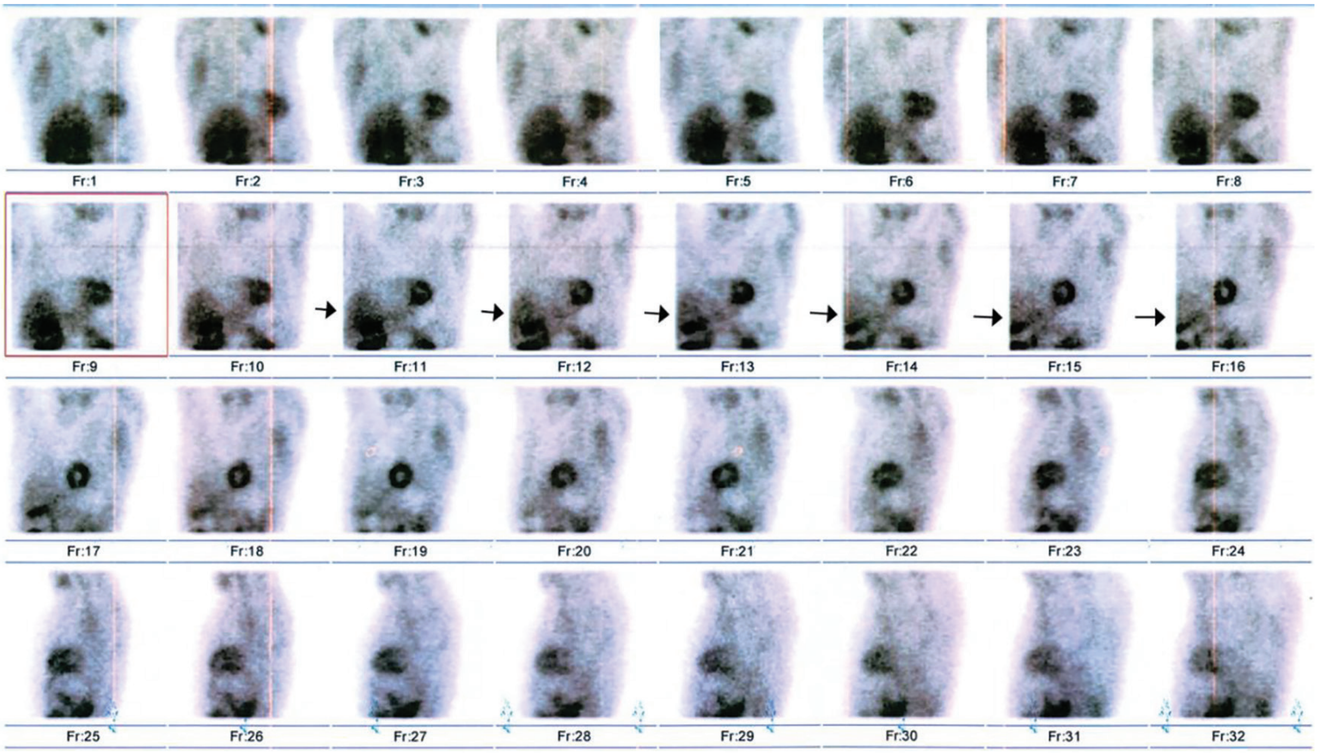

Figure 1. A 50-year-old man presented for myocardial perfusion single-photon emission computed tomography imaging. Scans are conducted during the stress and rest phases using a dual-headed gamma camera (Siemens Symbia T series) configured at a 90° angle. For resolving the diaphragmatic attenuation effect, prone imaging is performed. On prone imaging, left margin of projections 9 to 16 in the cinematic raw images, which include 32 projections in total and 16 projections for each detector, seems to be cropped incrementally in width.

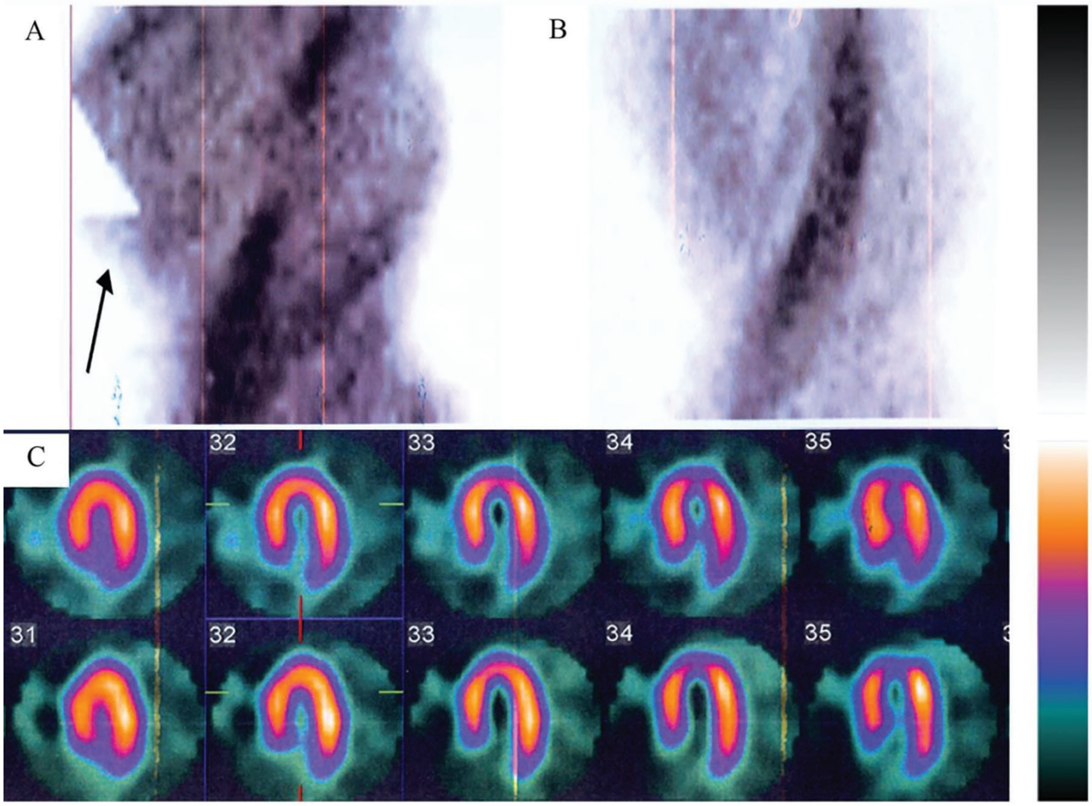

Figure 2. Inspecting the related sinograms, a wedge-shaped or triangular zone of absent activity was observed in the left margin of the sinogram of prone stress phase, (as shown by arrow in A) affecting several successive projections. The width of the defect is gradually increasing projection-by-projection until the end of the acquisition arc of detector 1, and, thereafter, abrupt resumption is seen at the beginning of the acquisition arc of detector 2. The tip of the triangular defect does not reach the sinusoidal band of left ventricle (LV) in the sinogram. Fortunately, the liver was resected, and LV remained unaffected. The sinogram of the rest phase is intact, (B). The tomographic slices (C) reconstructed from the horizontal long-axis of the prone and rest phases, using the iterative maximum likelihood expectation maximization method, from this projection dataset were free from this artifact. In rest and stress images performed in the supine position, no similar defect was observed in the sinogram and corresponding tomographic slices. The same finding was observed in other patients' scans, mostly was acquired in prone position, and rarely in supine position (the latter in heavy patients). All routine quality control tests, including the center of rotation test, were acceptable. Truncation artifacts are one of several artifacts affecting single photon emission computed tomography imaging. When the LV is truncated, perfusion defects can occur. In rotating or cinematic images, this problem is easily recognizable, where in some successive projections, LV is abutting the border of projection or being cut. The solution to this problem is easy. When it is noticed, the operator should reposition the axis of rotation of the gantry (detector heads) to the longitudinal or z-axis of the patient. Another source may be encountered when imaging is performed using the option of auto-body contouring. In patients with small body size, some interference occurs between the two detectors because each detector tries to approach the patient. Using bags of saline or covering the patient with folded blankets may rectify this problem; otherwise, another orbit (circular or elliptical) should be applied (1,2,3,4,5). In our case, none of the above sources was the culprit for this artifact. As mentioned, it arises mostly in prone imaging, where the detectors are positioned below the scanning table and disappears when imaging is done in the supine position. In the prone patient position, detectors are rotating around the patient while ascending above the scanning table. One plausible explanation is that because of mechanical instability, the lower positioned detector bears the weight of another detector and thus prevents proper positioning. This is responsible for the graded or incremental truncation of projections, creating a wedge-shaped appearance. The problem remained unresolved after repeated examination by the service engineers accredited by the vendor. This problem can be of interest to engineers and technicians. Fortunately, in this case, the heart was not affected, and the need for repeating or discarding the prone imaging was obviated.

Ethics

Informed Consent: An informed written consent was obtained from the patient both for performing the scanning and also for use and anonymous publishing of the images.

Footnotes

Authorship Contributions

Concept: M.Q., R.A., Design: M.Q., R.A., A.A., Data Collection or Processing: R.A., Analysis or Interpretation: M.Q., R.A., A.A., Literature Search: R.A., A.A., Writing: M.Q., R.A., A.A.

Conflict of Interest: No conflicts of interest were declared by the authors.

Financial Disclosure: The authors declare that this study has received no financial support.

References

1. Wosnitzer B, Gadiraju R, Depuey G. The truncation artifact. J Nucl Cardiol. 2011;18:187-191.
2. Matsumoto N, Suzuki Y, Yoda S, Hirayama A. The truncation artefact in patients with a high body mass index on myocardial perfusion SPECT. BMJ Case Rep. 2014;2014.
3. McGowan SE, Greaves CD, Evans S. An investigation into truncation artefacts experienced in cardiac imaging using a dedicated cardiac SPECT gamma camera with transmission attenuation correction. Nucl Med Commun. 2012;33:1287-1291.
4. Tsougos I, Alexiou S, Theodorou K, Valotassiou V, Georgoulias P. The prevalence of a false-positive myocardial perfusion stress SPET test in a skinny patient, induced by projection truncation. Hell J Nucl Med. 2015;18:79-80.
5. Yapici O, Baris S, Alic T, Basoglu T. Auto-contouring at 90 degrees dual head fitting angle: a potential cause of a myocardial perfusion SPET artifact in slim patients. Hell J Nucl Med. 2009;12:289-290.

Interesting Image

Mol Imaging Radionucl Ther 2026;35(1):55-57 ***DOI:****10.4274/mirt.galenos.2025.54036*

Isolated Unilateral Ovarian Metastasis from Breast Cancer Demonstrated by ^{18}F-FDG PET/CT

^{18}F-FDG PET/BT ile Gösterilen Meme Kanserinden Kaynaklanan İzole Tek Taraflı Over Metastazı

Nur Aydınbelge Dizdar, Ebru Tatcı, Derya Çayır, Özlem Özmen

University of Health Sciences Türkiye, Ankara Etlik City Hospital, Clinic of Nuclear Medicine, Ankara, Türkiye

Abstract

A 49-year-old premenopausal woman with a history of left modified radical mastectomy and axillary lymph node dissection for invasive lobular carcinoma three years ago, underwent ^{18}F-fluorodeoxyglucose positron emission tomography/computed tomography (^{18}F-FDG PET/CT) due to gradually increasing CA15-9 and CEA levels during routine follow-up. Compared with previous ^{18}F-FDG PET/CT images, the left ovary in the current images showed increased size and radiotracer uptake. Subsequently, total abdominal hysterectomy and bilateral salpingo-oophorectomy were performed, and histopathological evaluation confirmed unilateral metastasis in the left ovary due to primary breast cancer. Although rare, possible isolated ovarian metastasis should be considered in patients with breast cancer who have increased size and radiotracer uptake in ovarian tissue on follow-up ^{18}F-FDG PET/CT scans.

Keywords: Breast carcinoma, ^{18}F-FDG PET/CT, unilateral ovarian metastasis, isolated ovarian metastasis, ovarian uptake

Öz

İnvaziv lobüler karsinom nedeniyle üç yıl önce sol modifiye radikal mastektomi ve aksiller lenf nodu diseksiyonu olan 49 yaşındaki premenopozal kadın hastaya rutin takipleri sırasında giderek artan CA15-9 ve CEA düzeyleri nedeniyle ^{18}F-florodeoksiglukoz pozitron emisyon tomografisi/bilgisayarlı tomografinin (^{18}F-FDG PET/BT) çekildi. Önceki ^{18}F-FDG PET/BT görüntüleri ile karşılaştırıldığında, sol overin boyutunda ve radyoaktivite tutulumunda artış görüldü. Daha sonra total abdominal histerektomi ve bilateral salpingo-ooferektomi uygulandı ve histopatolojik değerlendirme sadece sol overde primer meme kanserine bağlı tek taraflı metastazı doğruladı. Nadir görülmekle birlikte, takip ^{18}F-FDG PET/BT taramalarında over dokusunun boyutunda ve radyotracer tutulumu artış olan meme kanseri hastalarında olası izole over metastazı ihtimali göz önünde bulundurulmalıdır.

Anahtar Kelimeler: Meme karsinomu, ^{18}F-FDG PET/BT, tek taraflı over metastazı, izole over metastazı, over tutulumu

---

Address for Correspondence: Nur Aydınbelge Dizdar, University of Health Sciences Türkiye, Ankara Etlik City Hospital, Clinic of Nuclear Medicine, Ankara, Türkiye
E-mail: fnuraydinbelge@gmail.com **ORCID ID:** orcid.org/0000-0002-9657-6906

Received: 07.04.2025 **Accepted:** 17.08.2025 **Epub:** 11.11.2025 **Publication Date:** 03.02.2026

Cite this article as: Aydınbelge Dizdar N, Tatcı E, Çayır D, Özmen Ö. Isolated unilateral ovarian metastasis from breast cancer demonstrated by ^{18}F-FDG PET/CT. Mol Imaging Radionucl Ther. 2026;35(1):55-57.

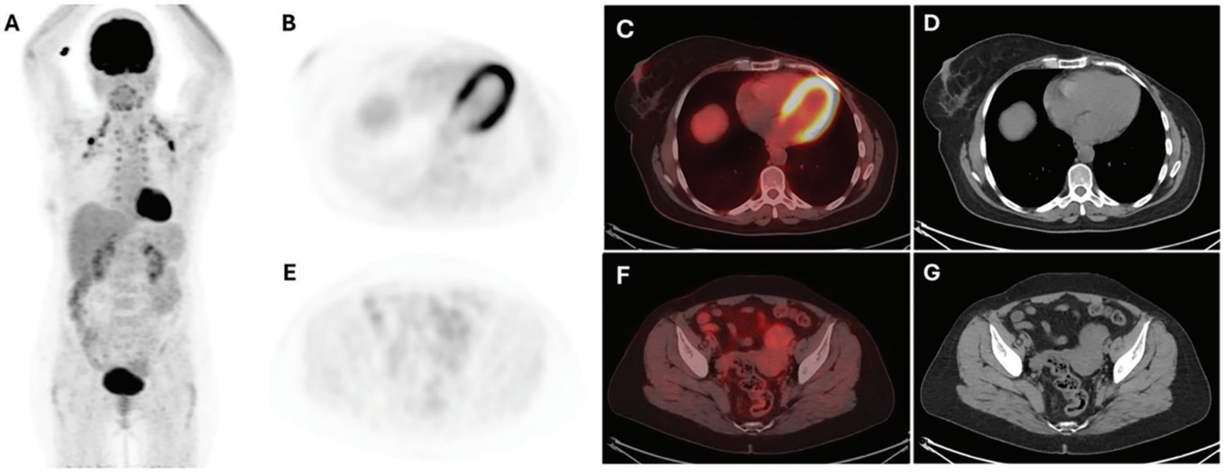

Figure 1. A 49-year-old premenopausal woman with a history of left modified radical mastectomy and left axillary lymph node dissection for invasive lobular carcinoma after neoadjuvant chemotherapy has been treated with tamoxifen and adjuvant external radiotherapy. ^{18}F-fluorodeoxyglucose positron emission tomography (PET)/computed tomography (CT) did not reveal pathologically increased radiotracer uptake, except for the radiotracer uptake in brown fat tissue observed in maximum intensity projection. The axial slices of the PET study (B), fused PET/CT (C), and CT (D) of the thoracic region showed no pathological activity involvement, which may be compatible with local recurrence of the primary malignant disease and/or metastatic processes. In the axial slices of the PET study (E), fused PET/CT (F), and CT (G), of the pelvic region, low radiotracer uptake soft tissue densities were observed in the left ovary region (maximum standard uptake values: 2.63). The endometrial curettage and smear test were reported to be incompatible with malignancy and metastatic disease. During two years of follow-up under-treatment, serum CA15-9 and CEA levels remained stable.

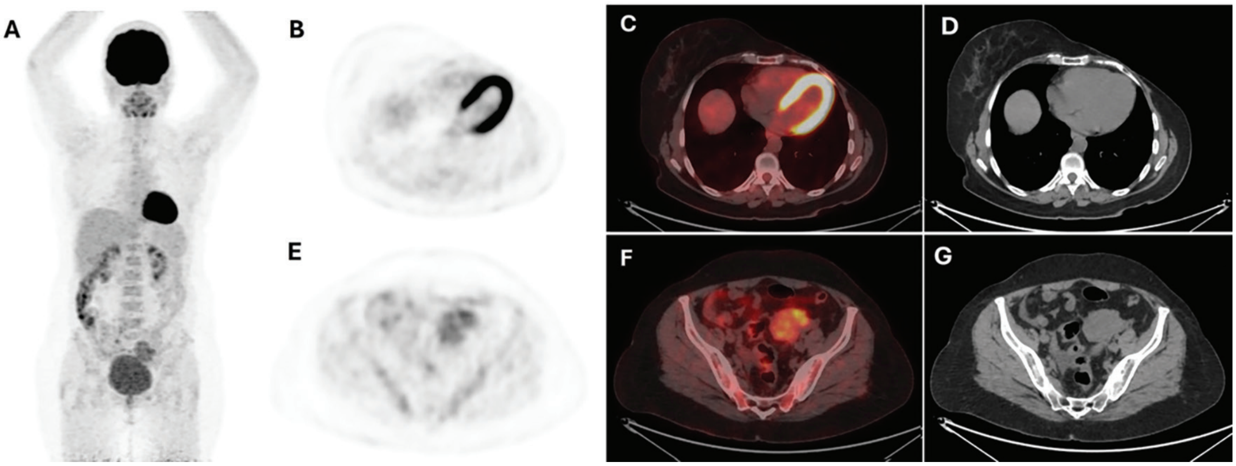

Figure 2. Afterwards, ^{18}F-fluorodeoxyglucose positron emission tomography/computed tomography (^{18}F-FDG PET/CT) was performed due to the progressive increase in serum CA15-9 and CEA levels within a 6-month period (A-D). It demonstrated that only the left ovary showed an increased size and radiotracer uptake (maximum standard uptake values: 5.1) compared to previous ^{18}F-FDG PET/CT images in the axial section of the PET study (E), fused PET/CT (F), and CT (G) of the pelvic region. Subsequently, the patient underwent total abdominal hysterectomy and bilateral salpingo-oophorectomy and the histopathological assessment revealed unilateral metastasis in the left ovary due to primary breast cancer (BC).

BC can frequently metastasize to bones, lungs, liver, and brain. However, invasive lobular carcinoma (ILC) has a greater tendency to metastasize to disseminated sites including the gastrointestinal (GI) tract, peritoneum, gynecological organs, skin, and adrenal glands (1). Among gynecologic organs, ovaries are the most frequently site of metastasis of BC (2). Tumors may metastasize to the ovaries through various routes, including direct, hematogenous, and lymphatic spread, as well as transcoelomic dissemination (3). Several studies have shown that GI tract (gastric, colon and rectum) tumors are the most common primary neoplasm metastasizing to the ovary, followed by uterine, BC, pancreatic cancer, lymphoma, malignant melanoma and others (3,4).

Ovarian metastasis from BC is more frequently seen in younger and premenopausal women. They are asymptomatic until they reach a certain size, so they are frequently associated with other poor prognostic factors such as the presence of other metastatic sites, large primary breast lesion size, inflammatory BC, lymph node involvement, advanced stage (stage III-IV), and bilateralism (5). Therefore, it is frequently associated with worse prognosis and outcomes, and a shorter 5-year survival rate (6). Isolated unilateral ovarian metastasis from ILC is extremely rare. Furthermore, ILC shows low FDG uptake, so ^{18}F-FDG PET/CT may have a lower impact on systemic staging for ILC than for invasive ductal carcinoma (7). However, in this case, ^{18}F-FDG PET/CT detected an isolated ovarian radiotracer uptake, raising suspicion of metastasis. This case report demonstrated that the presence of increased size and FDG uptake, merely in the isolated unilateral ovary, should be considered a potential indication of metastatic spread of BC.

Ethics

Informed Consent: The informed consent was obtained from the patient.

Footnotes

Authorship Contributions

Surgical and Medical Practices: N.A.D., Concept: E.T., Design: D.Ç., Data Collection or Processing: Ö.Ö., Analysis or Interpretation: D.Ç., Ö.Ö., Literature Search: E.T., Writing: N.A.D.

Conflict of Interest: No conflicts of interest were declared by the authors.

Financial Disclosure: The authors declare that this study has received no financial support.

References

1. DiPiro PJ, Tirumani SH, Cruz GP, Ramaiya NH, Lester SC, Shinagare AB. Lobular breast cancer: patterns of intraabdominal metastatic spread on imaging and prognostic significance. Abdom Radiol (NY). 2019;44:362-369.
2. Kutasovic JR, McCart Reed AE, Males R, Sim S, Saunus JM, Dalley A, McEvoy CR, Dedina L, Miller G, Peyton S, Reid L, Lal S, Niland C, Ferguson K, Fellowes AP, Al-Ejeh F, Lakhani SR, Cummings MC, Simpson PT. Breast cancer metastasis to gynaecological organs: a clinico-pathological and molecular profiling study. J Pathol Clin Res. 2019;5:25-39.
3. Kubeček O, Laco J, Špaček J, Petera J, Kopecký J, Kubečková A, Filip S. The pathogenesis, diagnosis, and management of metastatic tumors to the ovary: a comprehensive review. Clin Exp Metastasis. 2017;34:295-307.
4. Roseland ME, Millet JD, Wasnik AP. Imaging of metastatic disease to the ovary/adnexa. Magn Reson Imaging Clin N Am. 2023;31:93-107.
5. Tian W, Zhou Y, Wu M, Yao Y, Deng Y. Ovarian metastasis from breast cancer: a comprehensive review. Clin Transl Oncol. 2019;21:819-827.
6. Pimentel C, Becquet M, Lavoue V, Henno S, Leveque J, Ouldamer L. Ovarian metastases from breast cancer: a series of 28 cases. Anticancer Res. 2016;36:4195-4200.
7. Hogan MP, Goldman DA, Dashevsky B, Riedl CC, Gonen M, Osborne JR, Jochelson M, Hudis C, Morrow M, Ulaner GA. Comparison of ^{18}F-FDG PET/CT for systemic staging of newly diagnosed invasive lobular carcinoma versus invasive ductal carcinoma. J Nucl Med. 2015;56:1674-1680.

Interesting Image

Mol Imaging Radionucl Ther 2026;35(1):58-60 ***DOI:****10.4274/mirt.galenos.2025.83713*

^{99m}Tc-MDP Bone Scintigraphy in a Case of X-Linked Spondyloepiphyseal Dysplasia Tarda

X'e Bağlı Spondiloepifizyal Displazi Tarda Olgusunda ^{99m}Tc-MDP Kemik Sintigrafisi

Ikram Zahfir, Salah Oueriagli Nabih, Meryem Aboussabr, Yassir Benameur, Omar Ait Sahel,
Abderrahim Doudouh

Mohammed V Military Teaching Hospital, Clinic of Medicine and Pharmacy, Mohammed V University of Rabat Faculty of Medicine, Department of Nuclear Medicine, Rabat, Morocco

Abstract

Spondyloepiphyseal dysplasia tarda (SEDT) is a rare X-linked skeletal disorder affecting the spine and long bones, leading to short stature, spinal deformities, and joint stiffness. It is caused by genetic mutations, and primarily affects males. Diagnosis is confirmed by imaging and genetic testing. We report the case of a 33 years old patient with a history of X-linked SEDT, who presented with pain in the lower limbs and pelvis, accompanied by limited mobility. Bone scan with ^{99m}Tc-methylene diphosphonate (MDP) revealed a polyostotic SEDT involvement, periarticular ossifications, and bony bridges in the active phase. The authors highlight the role of bone scan with ^{99m}Tc-MDP in diagnosing this rare disease.

Keywords: Bone scan, ^{99m}Tc-MDP, spondyloepiphyseal dysplasia tarda, polyostotic involvement

Öz

Spondiloepifizyal displazi tarda (SEDT), omurga ve uzun kemikleri etkileyen, kısa boy, omurga deformiteleri ve eklem sertliğine yol açan nadir bir X'e bağlı geçiş gösteren iskelet hastalığıdır. Genetik mutasyonlardan kaynaklanır ve öncelikli olarak erkekleri etkiler. Tanı, görüntüleme ve genetik testlerle doğrulanır. Alt ekstremitelerde ve pelviste ağrı ve hareket kısıtlılığı ile başvuran, X'e bağlı SEDT öyküsü olan 33 yaşında bir hastayı bildiriyoruz. ^{99m}Tc-metilen difosfonat (MDP) ile yapılan kemik taraması, poliostotik SEDT tutulumunu, periartiküler ossifikasyonları ve aktif fazda kemik köprüleri gösterdi. Yazarlar, bu nadir hastalığın tanısında ^{99m}Tc-MDP ile yapılan kemik taramasının rolünü vurgulamaktadır.

Anahtar kelimeler: Kemik taraması, ^{99m}Tc-MDP, spondiloepifizyal displazi tarda, poliostotik tutulum

---

Address for Correspondence: Ikram Zahfir, Mohammed V Military Teaching Hospital, Clinic of Medicine and Pharmacy, Mohammed V University of Rabat Faculty of Medicine, Department of Nuclear Medicine, Rabat, Morocco
E-mail: ikramzahfir@gmail.com **ORCID ID:** orcid.org/0009-0002-4822-6175

Received: 17.05.2025 **Accepted:** 31.08.2025 **Epub:** 26.11.2025 **Publication Date:** 03.02.2026

Cite this article as: Zahfir I, Nabih SO, Aboussabr M, Benameur Y, Sahel OA, Doudouh A. ^{99m}Tc-MDP bone scintigraphy in a case of X-linked spondyloepiphyseal dysplasia tarda. Mol Imaging Radionucl Ther. 2026;35(1):58-60.

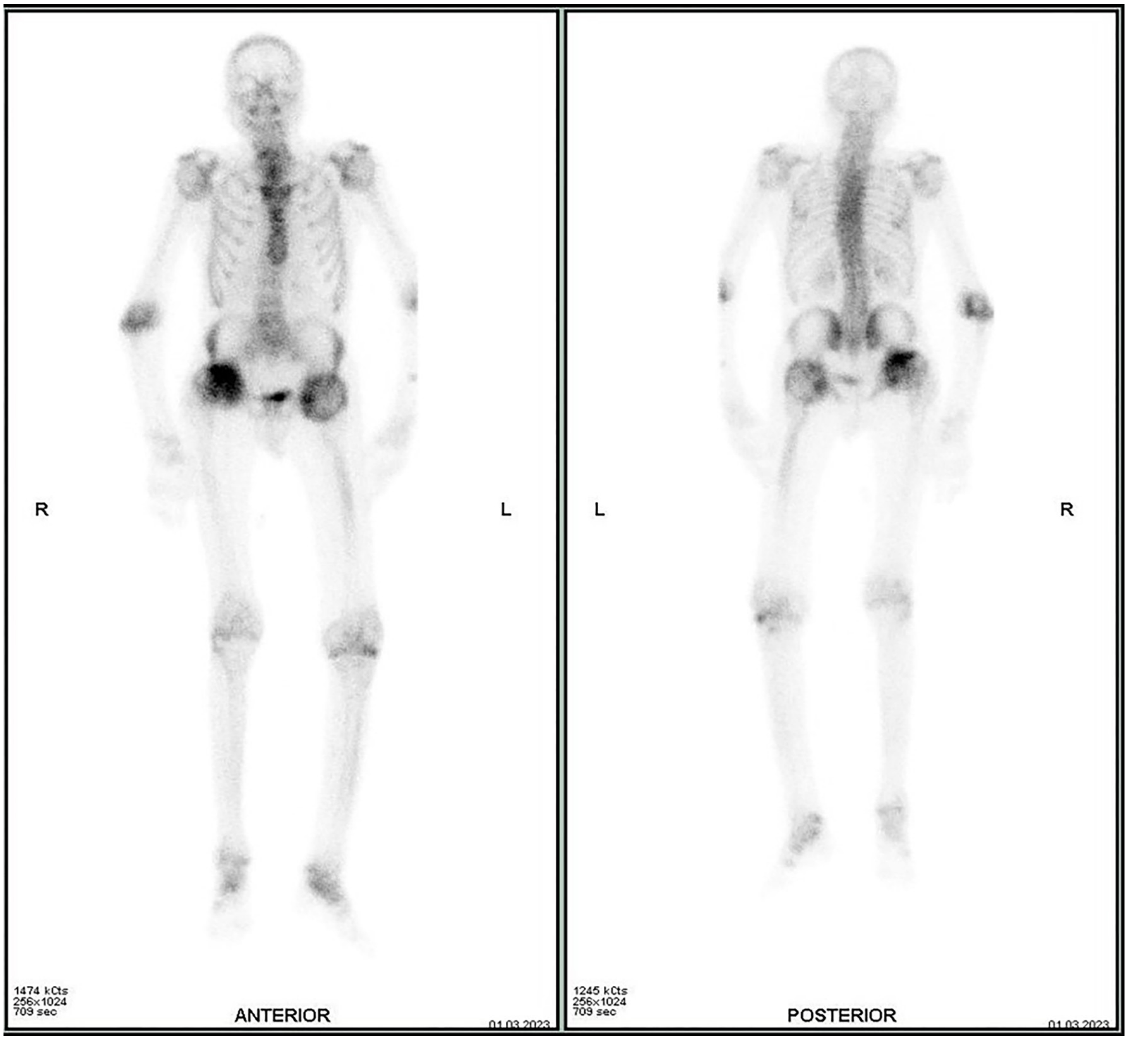

Figure 1. A 33-year-old patient with a known history of X-linked spondyloepiphyseal dysplasia tarda (SEDT) is presenting with lower limb and pelvic pain, accompanied by limited mobility. Standard radiographs showed hump-shaped deformities in the central portion of the vertebrae, narrowed intervertebral disc spaces, and moderate epiphyseal dysplasia of the long bones. These findings were associated with bony bridges in the hips and knees.

A bone scan with ^{99m}Tc-methylene diphosphonate ^{99m}Tc-(MDP), performed 3 hours after the intravenous injection of 666 MBq (18 mCi) of ^{99m}Tc-MDP, revealed heterogeneous and abnormally increased activity with deformities of the femoral heads, elbows, knees, and ankles, a short spine, and marked thoracolumbar scoliosis, consistent with polyostotic SEDT involvement. Focal and linear areas of increased uptake were seen in the knees and hips, corresponding to periarticular ossifications and bony bridges in the active phase (Figure 1).

SED is a subgroup of bone dysplasias that affects the spine and the epiphyses of long bones. It includes three major forms: congenital SED, late-onset (tarda) SED, and SED associated with progressive arthropathy (1). More recently, at least four types of SEDT, some with autosomal recessive inheritance and others with autosomal dominant inheritance, have also been described (2). The classical form of SEDT, as illustrated in this case, is a genetic disorder inherited in an X-linked recessive pattern, manifesting exclusively in males. It results from mutations in the *SEDL* gene located on Xp22.12-p22.31 and manifests around puberty with back pain, a short stature and a short trunk, while the extremities and face remain unaffected. Early onset degenerative joint disease, particularly affecting the spine and hips, usually develops in early adulthood. Radiologic abnormalities of the vertebral bodies include platyspondyly and a central hump (1,3). Bone scan is rarely indicated in SEDT; however, the skeletal involvement observed in this condition is unusual, requiring a thorough understanding of the distribution pattern of bone abnormalities for accurate interpretation and to avoid confusion with other entities, thereby ensuring appropriate management (4).

Ethics

Informed Consent: Informed consent was obtained from the patient.

Footnotes

Authorship Contributions

Surgical and Medical Practices: I.Z., Concept: I.Z., S.O.N., M.A., A.D., Data Collection or Processing: I.Z., S.O.N., A.D., Analysis or Interpretation: I.Z., M.A., Literature Search: I.Z., S.O.N., M.A., Y.B., O.A.S., A.D., Writing: I.Z., S.O.N., A.D.

Conflict of Interest: No conflicts of interest were declared by the authors.

Financial Disclosure: The authors declare that this study has received no financial support.

References

1. Kocyigit H, Arkun R, Ozkinay F, Cogulu O, Hizli N, Memis A. Spondyloepiphyseal dysplasia tarda with progressive arthropathy. Clin Rheumatol. 2000;19:238-241.
2. Panda A, Gamanagatti S, Jana M, Gupta AK. Skeletal dysplasias: a radiographic approach and review of common non-lethal skeletal dysplasias. World J Radiol. 2014;6:808-825.
3. Gedeon AK, Tiller GE, Le Merrer M, Heuertz S, Tranebjaerg L, Chitayat D, Robertson S, Glass IA, Savarirayan R, Cole WG, Rimoin DL, Kousseff BG, Ohashi H, Zabel B, Munnich A, Gecz J, Mulley JC. The molecular basis of X-linked spondyloepiphyseal dysplasia tarda. Am J Hum Genet. 2001;68:1386-1397.
4. Yang F, Xu HQ, Li CL, Yang JG. Incidental finding of Tc-99m MDP bone scintigraphy in a case of X-linked spondyloepiphyseal dysplasia tarda. Clin Nucl Med. 2012;37:193-195.

Interesting Image

Mol Imaging Radionucl Ther 2026;35(1):61-63 ***DOI:****10.4274/mirt.galenos.2025.45712*

Hepatic Vascular Shunts Mimicking Malignant Lesions on ^{18}F-FDG PET/CT Imaging: Interpretation Pitfall in the Background of Cirrhotic Liver

^{18}F-FDG PET/BT Görüntülemede Malign Lezyonları Taklit Eden Hepatik Vasküler Şantlar: Sirotik Karaciğer Zemininde Yorumlama Zorluğu

Sanchay Jain, Assim Saad Eddin, Parren McNeely, Michael Graham, Ahmad Shariftabrizi

University of Iowa Health Care Faculty of Medicine, Department of Radiology, Division of Nuclear Medicine, Iowa City, United States

Abstract

A 44-year-old female presented with recent history of ischemic strokes and hypercoagulability and chronic alcoholic cirrhosis. ^{18}F-fluorodeoxyglucose (FDG) positron emission tomography (PET)/computed tomography was performed during the workup for vasculitis. PET features of vasculitis were not identified, but liver showed multiple hepatic FDG avid foci, concerning for malignant or metastatic disease in the background of cirrhosis of liver. To characterize these lesions, liver magnetic resonance imaging was subsequently performed which revealed hepatic vascular shunts corresponding to the sites of the FDG avid foci. This case highlights potential interpretation n pitfall arising due to FDG avidity in the vascular shunts resembling malignant or metastatic lesions.

Keywords: ^{18}F-FDG PET/CT, hepatic vascular shunt, liver cirrhosis

Öz

Kırk dört yaşında bir kadın hasta, yakın zamanda geçirilmiş iskemik inme, hiperkoagülabilite ve kronik alkolik siroz öyküsü ile başvurdu. Vaskülit tetkikleri sırasında ^{18}F-florodeoksiglukoz (FDG) pozitron emisyon tomografisi (PET)/bilgisayarlı tomografi çekildi. Vaskülite dair PET bulguları saptanmadı, ancak karaciğerde siroz zemininde malign veya metastatik hastalıkla ilişkili çoklu hepatik FDG avid odakları görüldü. Bu lezyonları karakterize etmek için daha sonra karaciğer manyetik rezonans görüntülemesi çekildi ve FDG avid odaklarının bulunduğu bölgelere karşılık gelen hepatik vasküler şantlar saptandı. Bu olgu, malign veya metastatik lezyonları andıran vasküler şantlardaki FDG aviditesi nedeniyle ortaya çıkabilecek olası yorumlama zorluğunu vurgulamaktadır.

Anahtar kelimeler: ^{18}F-FDG PET/BT, hepatik vasküler şant, karaciğer sirozu

---

Address for Correspondence: Ahmad Shariftabrizi, University of Iowa Health Care Faculty of Medicine, Department of Radiology, Division of Nuclear Medicine, Iowa City, United States

E-mail: ashariftabrizi@gmail.com **ORCID ID:** orcid.org/0000-0003-2397-6914

Received: 16.02.2025 **Accepted:** 21.09.2025 **Publication Date:** 03.02.2026

Cite this article as: Jain S, Eddin AS, McNeely P, Graham M, Shariftabrizi A. Hepatic vascular shunts mimicking malignant lesions on ^{18}F-FDG PET/CT imaging: interpretation pitfall in the background of cirrhotic liver. Mol Imaging Radionucl Ther. 2026;35(1):61-63.

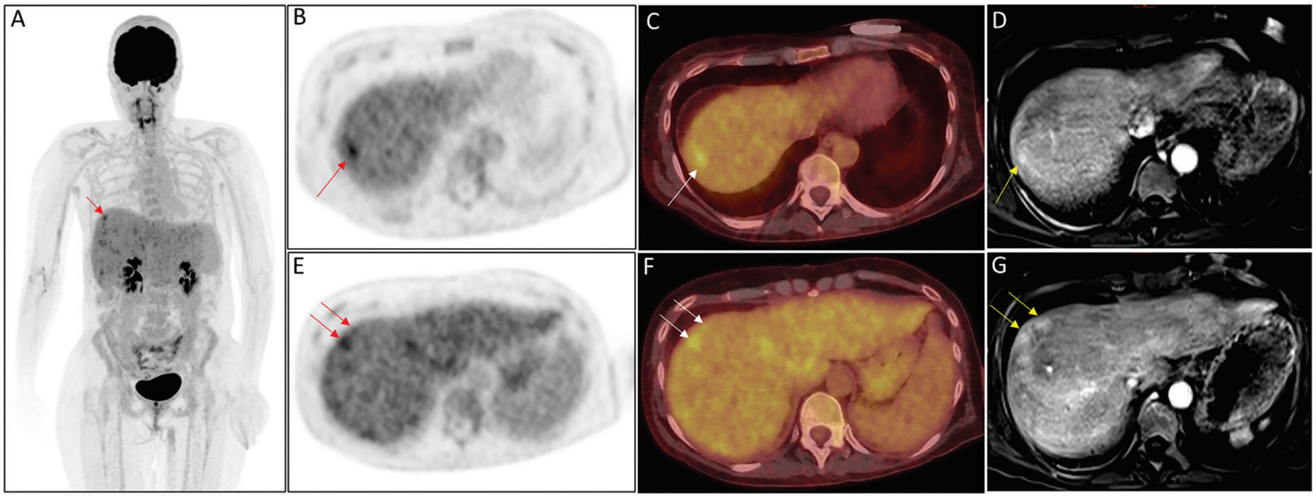

Figure 1. A 44-year-old woman presented with a history of recurrent ischemic strokes, alcoholic cirrhosis, hypercoagulability, and Raynaud's phenomenon. A diagnostic angiogram showed multifocal narrowing of the bilateral middle cerebral arteries and their branches. Her serologic workup was remarkable for positive antinuclear antibodies, and anti-ribonucleoprotein antibodies. She also had positive cell based and immunofluorescence assays for cerebrospinal fluid glial fibrillary acidic protein. A contrast enhanced computed tomography (CECT) of chest, abdomen and pelvis was obtained which revealed lobulated liver with diffuse heterogeneous enhancement and no hepatic tumors; no significant findings related to vasculitis were noted. Subsequently, a whole body ^{18}F-fluorodeoxyglucose positron emission tomography/computed tomography (^{18}F-FDG PET/CT) was performed (1,2). The maximum intensity projection image (A) shows heterogeneous FDG distribution in the liver with few intensely FDG avid foci. Transaxial PET (B, E), and fused PET/CT (C, F) images shown here demonstrate the intensely FDG avid foci in the segments 7 and 8 of the liver (arrows), in the background of heterogeneous hepatic FDG uptake. No vasculitis pattern or other FDG avid abnormal foci were noted elsewhere. Given the history of cirrhosis, hypercoagulability and the clinical presentation, these FDG avid foci raised a concern for malignant or metastatic liver disease. Magnetic resonance imaging (MRI) the liver was then performed. Axial VIBE MRI sequences shown here (D, G) revealed subcapsular enhancing foci in the venous phase at the sites corresponding to FDG avid foci in hepatic segments 7 and 8, suggestive of vascular shunts. Furthermore, no arterially enhancing hepatic foci were seen. Intrahepatic vascular shunts can arise secondary to other various etiologies and hepatocellular carcinoma, hemangiomas, cirrhosis, trauma, congenital, Budd Chiari syndrome are among the common causes (3). Cirrhosis is a known risk factor for developing hepatocellular carcinoma. In the presented case, both CECT and MRI revealed hepatic parenchymal changes and lobulated liver consistent with the history of alcoholic cirrhosis, but neither of these imaging modalities revealed hepatic tumors or metastatic lesions, nor any venous thrombosis was identified. As noted in this case, FDG avid foci in non-malignant conditions such as vascular shunts can resemble malignant or metastatic tumors, and it can be challenging to lean towards a diagnosis without further imaging (4,5). Dedicated MRI of the liver is often helpful in accurate characterization of such lesions (6,7,8).This case highlights interpretation pitfall arising due to hepatic vascular shunt resembling malignant disease on ^{18}F-FDG PET/CT in the background of cirrhotic liver, where malignancy is otherwise an important differential and utilizing multimodality imaging is advantageous in ruling out malignant disease.

Ethics

Informed Consent: Requirement for informed consent was waived by University of Iowa's Human Subject Office.

Footnotes

Authorship Contributions

Concept: P.M., M.G., A.S., Design: A.S., Data Collection or Processing: S.J., A.S.E., Analysis or Interpretation: P.M., M.G., A.S., Literature Search: S.J., A.S.E., Writing: S.J., A.S.E.

Conflict of Interest: No conflicts of interest were declared by the authors.

Financial Disclosure: The authors declare that this study has received no financial support.

References

1. Lebech AM, Gaardsting A, Loft A, Graff J, Markova E, Bertelsen AK, Madsen JL, Andersen KF, Benzon EV, Helms M, Mathiesen LR, David KP, Kronborg G, Kjaer A. Whole-body ^{18}F-FDG PET/CT is superior to CT as first-line diagnostic imaging in patients referred with serious nonspecific symptoms or signs of cancer: a randomized prospective study of 200 patients. J Nucl Med. 2017;58:1058-1064.
2. Slart RHJA; Writing group; Reviewer group; Members of EANM cardiovascular; members of EANM Infection & Inflammation; Members of Committees, SNMMI Cardiovascular; Members of Council, PET Interest Group; Members of ASNC; EANM Committee Coordinator. FDG-PET/CT(A) imaging in large vessel vasculitis and polymyalgia rheumatica: joint procedural recommendation of the EANM, SNMMI, and the PET Interest Group (PIG), and endorsed by the ASNC. Eur J Nucl Med Mol Imaging. 2018;45:1250-1269.
3. Wang Q, Koniaris LG, Milgrom DP, Patel A, Hu M, Cui E, Deng Y, Akisik F. CT and MRI imaging and interpretation of hepatic arterioportal shunts. Transl Gastroenterol Hepatol. 2019;4:34.

4. Ozaki K, Harada K, Terayama N, Kosaka N, Kimura H, Gabata T. FDG-PET/CT imaging findings of hepatic tumors and tumor-like lesions based on molecular background. Jpn J Radiol. 2020;38:697-718.
5. Tan GJ, Berlangieri SU, Lee ST, Scott AM. FDG PET/CT in the liver: lesions mimicking malignancies. Abdom Imaging. 2014;39:187-195.
6. Coenegrachts K. Magnetic resonance imaging of the liver: new imaging strategies for evaluating focal liver lesions. World J Radiol. 2009;1:72-85.
7. Bashir U, Shah S, Jeph S, O'Keeffe M, Khosa F. Magnetic resonance (MR) imaging of vascular malformations. Pol J Radiol. 2017;82:731-741.
8. Flors L, Leiva-Salinas C, Maged IM, Norton PT, Matsumoto AH, Angle JF, Hugo Bonatti M, Park AW, Ahmad EA, Bozlar U, Housseini AM, Huerta TE, Hagspiel KD. MR imaging of soft-tissue vascular malformations: diagnosis, classification, and therapy follow-up. Radiographics. 2011;31:1321-1340.

Interesting Image

Mol Imaging Radionucl Ther 2026;35(1):64-66 ***DOI:****10.4274/mirt.galenos.2025.83436*

A Rare Case of Small Cell Lung Carcinoma Diagnosed with a Breast Mass

Memede Kitle ile Tanı Konulan Nadir Bir Küçük Hücreli Akciğer Karsinomu Olgusu

Nur Aydınbelge Dizdar[1], Derya Çayır[1], Hatice Türksoy Karaca[2], Ata Türker Arıkök[2], Özlem Özmen[1]

[1]*University of Health Sciences Türkiye, Ankara Etlik City Hospital, Clinic of Nuclear Medicine, Ankara, Türkiye*
[2]*University of Health Sciences Türkiye, Ankara Etlik City Hospital, Clinic of Pathology, Ankara, Türkiye*

Abstract

A 63-year-old woman presented to the emergency department with dyspnea, chest pain, and a palpable right breast mass. Non-contrast thoracic computed tomography (CT) scan revealed suspicious lesions in the right upper lung lobe and right breast, as well as right pleural effusion. For further evaluation, ^{18}F-fluorodeoxyglucose (FDG) positron emission tomography (PET)/CT scan was performed. There was increased FDG uptake in the right breast, right lung, liver, bones, and lymph nodes. Histopathological assessment confirmed that the breast mass was a metastatic lesion originating from a primary small-cell lung carcinoma. The manifestation of primary lung carcinoma with a metastatic mass lesion in the breast region is a rare condition. The manifestation can lead to diagnostic challenges, particularly when distinguishing it from a primary breast tumor. ^{18}F-FDG PET/CT may provide valuable information for staging and surveillance, especially in patients with atypical metastatic patterns. This case highlights that unexpected metastatic sites can significantly affect treatment strategies and are frequently associated with worse prognosis.

Keywords: Small cell lung carcinoma, breast mass, breast metastasis, ^{18}F-FDG PET/CT

Öz

Nefes darlığı, göğüs ağrısı ve sağ memede ele gelen kitle şikayeti olan 63 yaşında bir kadın hasta acil servise başvurdu. Kontrastsız bilgisayarlı tomografi (BT) sağ akciğer üst lobda ve sağ memede şüpheli kitlesel lezyonlar ve sağ hemitoraksta plevral efüzyon saptandı. Daha ayrıntılı değerlendirme için ^{18}F-florodeoksiglukoz (FDG) pozitron emisyon tomografisi (PET)/BT taraması yapıldı. Sağ memede, sağ akciğerde, karaciğerde, kemiklerde ve lenf düğümlerinde FDG alımında artış vardı. Histopatolojik değerlendirme, meme kitlesinin primer küçük hücreli akciğer karsinomundan kaynaklanan metastatik bir lezyon olduğunu doğruladı. Primer akciğer karsinomu nadiren memede metastatik lezyon olarak ortaya çıkar. Bu bulgu, özellikle primer meme tümöründen ayırt edilmesinde tanıya zorluklar yaratabilir. ^{18}F-FDG PET/BT, özellikle atipik metastatik paternleri olan hastalarda evreleme ve izleme için değerli bilgiler sağlayabilir. Bu olguda, beklenmedik metastatik bölgelerin tedavi stratejilerini önemli ölçüde etkileyebileceğini ve sıklıkla daha kötü prognozla ilişkili olduğunu vurgulamaktadır.

Anahtar kelimeler: Küçük hücreli akciğer karsinomu, memede kitle, meme metastazı, ^{18}F-FDG PET/BT

Address for Correspondence: Nur Aydınbelge Dizdar, University of Health Sciences Türkiye, Ankara Etlik City Hospital, Clinic of Nuclear Medicine, Ankara, Türkiye
E-mail: fnuraydinbelge@gmail.com **ORCID ID:** orcid.org/0000-0002-9657-6906

Received: 20.07.2025 **Accepted:** 29.09.2025 **Epub:** 26.12.2025 **Publication Date:** 03.02.2026

Cite this article as: Aydınbelge Dizdar N, Çayır D, Türksoy Karaca H, Arıkök AT, Özmen Ö. A rare case of small cell lung carcinoma diagnosed with a breast mass. Mol Imaging Radionucl Ther. 2026;35(1):64-66.

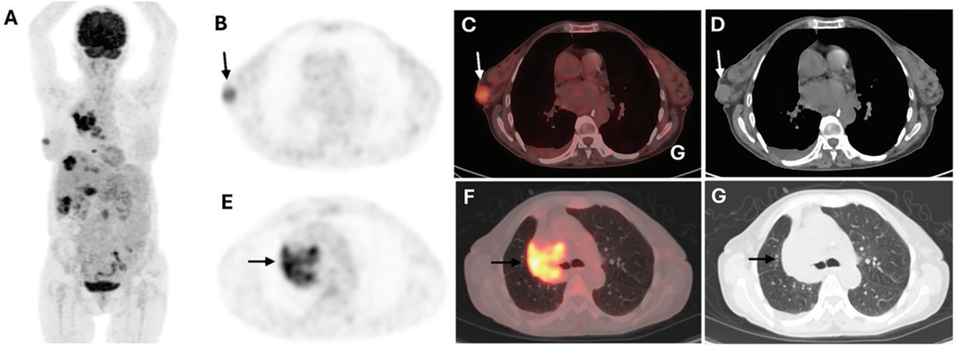

Figure 1. A 63-year-old woman with dyspnea, chest pain, and a palpable right breast mass was referred to the emergency department. Non-contrast chest computed tomography (CT) revealed a mass measuring approximately 20 mm in the upper outer quadrant of the right breast. Furthermore, it showed the right upper lobe central lung mass, enlargement of several mediastinal lymph nodes, and a right pleural effusion. Written informed consent was obtained for each procedure. Subsequently, ^{18}F-fluorodeoxyglucose (FDG) positron emission tomography (PET)/CT performed for further evaluation. The maximum intensity projection (MIP) image demonstrated multiple foci of increased FDG uptake (A, MIP image). An increased FDG uptake [maximum standard uptake (SUV_{max}), 4.2] was observed in the right breast mass (arrow) (B, PET image; C, fused PET/CT image; D, CT image). A centrally located mass in the right lung, indistinguishable from adjacent mediastinal lymph nodes, demonstrated an increased FDG uptake (SUV_{max}: 8.7) (E, PET image; F, fused PET/CT image; G, CT image). Several hypermetabolic mediastinal (SUV_{max}, 5.6) and periportal (SUV_{max}, 4.5) lymph nodes were detected. Additional FDG-avid lesions were observed in the liver, and multiple bone sites (A). These findings were consistent with widespread metastatic disease.

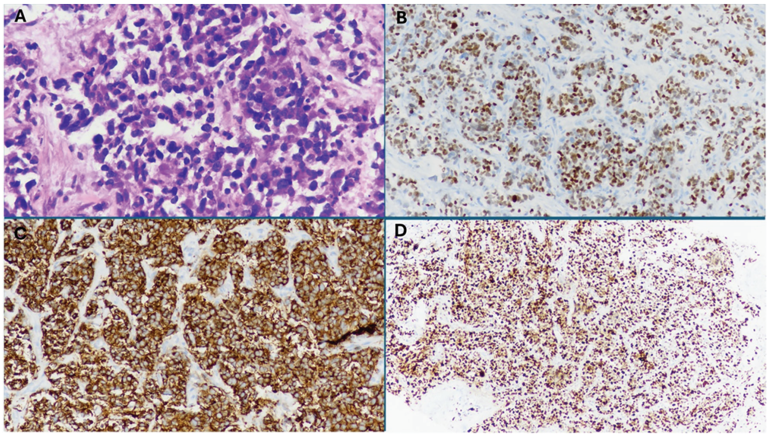

Figure 2. Afterwards, a biopsy of the right breast mass was performed. Histopathological examination with hematoxylin and eosin (H&E) showed small- to medium-sized round to oval cells with scant cytoplasm. Many cells showed finely dispersed "salt-and-pepper" chromatin with inconspicuous nucleoli and a high nuclear-to-cytoplasmic ratio (A; H&E, x400). Strong and diffuse nuclear positivity for thyroid transcription factor-1 (TTF-1) was observed in the cells (B; TTF-1, x200). The cells also showed positivity for synaptophysin (C; synaptophysin, x200) and a high proliferative index of approximately 80% with Ki-67 (D; Ki-67, x100). These findings confirmed the diagnosis of small cell lung cancer (SCLC) that had metastasized to the right breast.

The extramammary metastases to the breast are an infrequent manifestation, and their prevalence has been reported to vary between 0.1% and 5.0% (1). The most common extramammary malignancies that metastasize to the breast are lymphoma, malignant melanoma, cancers of the lung, thyroid, gallbladder, cervix, and ovary (2). Metastatic involvement of the breast from extramammary solid organ tumors represents a significant diagnostic challenge in routine clinical practice. Breast metastasis from lung cancer is an extremely rare clinical manifestation with an incidence of 0.2-1.3% (3). It has been suggested that lung cancer cells can spread to the pleura, infiltrate the axillary lymph nodes, and then reach the ipsilateral breast via retrograde lymphatic pathways (4).

Breast metastases from non-SCLC (NSCLC) have been reported more frequently than those from SCLC metastases (5). However, SCLC metastases to the breasts have occurred synchronously. It may be that SCLC is a very aggressive entity and is characterized by rapid tumor growth. Most patients have widespread metastases known as extensive-stage SCLC at the time of initial diagnosis (6). The most common metastatic sites of SCLC are mediastinal lymph nodes, liver, bone, and brain, respectively. It has been reported that the median overall survival for extensive-stage SCLC is approximately 12 months, while the 5-year survival rate for all SCLC patients remains only 6.8% (7). Furthermore, the median survival time for advanced-stage breast cancer patients with lung metastases has been reported to be approximately 21 months (8). An accurate diagnosis of breast mass is crucial in determining appropriate treatment strategies and improving patient outcomes. However, the clinical presentation of breast metastases concurrent with primary lung carcinoma is extremely rare and can complicate differential diagnosis. Consequently, in patients without a prior history of malignancy who present with a breast mass, both primary breast cancer and extramammary metastasis should be considered, as demonstrated in this case.

Ethics

Informed Consent: Informed consent was obtained from the patient.

Footnotes

Authorship Contributions

Surgical and Medical Practices: H.T.K., A.T.A., Concept: N.A.D., Ö.Ö., Design: N.A.D., D.Ç, Ö.Ö., Data Collection or Processing: D.Ç., H.T.K., A.T.K., Analysis or Interpretation: N.A.D, D.Ç., Literature Search: N.A.D., Ö.Ö., Writing: N.A.D D.Ç.

Conflict of Interest: No conflicts of interest were declared by the authors.

Financial Disclosure: The authors declare that this study has received no financial support.

References

1. Li J, Wahab R, Brown AL, Guarnieri B, Lewis K, Mahoney MC, Vijapura C. Extramammary metastases to the breast. Radiographics. 2023;43:e230036.
2. Zhou P, Chang N, Abraham SC, Albarracin CT, Huo L, Chen H, Ding Q, Resetkova E, Middleton LP, Sahin AA, Bu H, Wu Y. Metastatic nonhematopoietic neoplasms to the breast: a study of 238 cases. Hum Pathol. 2022;125:59-67.
3. Lee AH. The histological diagnosis of metastases to the breast from extramammary malignancies. J Clin Pathol. 2007;60:1333-1341.
4. Malek D, Buccheri S, Dey CB, Samli B, Plemmons J. Lung cancer metastasis to the breast mimicking inflammatory breast carcinoma on imaging. Radiol Case Rep. 2019;14:1500-1505.
5. Zhu Y, Liu WW, Wu Q, Yao JH, Zhou ZG, Yang Y. Clinical and molecular characteristics of secondary breast metastases from primary lung cancer: a study of 22 Chinese cases. Int J Clin Exp Pathol. 2020;13:1880-1885.
6. Ganti AKP, Loo BW, Bassetti M, Blakely C, Chiang A, D'Amico TA, D'Avella C, Dowlati A, Downey RJ, Edelman M, Florsheim C, Gold KA, Goldman JW, Grecula JC, Hann C, Iams W, Iyengar P, Kelly K, Khalil M, Koczywas M, Merritt RE, Mohindra N, Molina J, Moran C, Pokharel S, Puri S, Qin A, Rusthoven C, Sands J, Santana-Davila R, Shafique M, Waqar SN, Gregory KM, Hughes M. Small cell lung cancer, version 2.2022, NCCN Clinical Practice Guidelines in Oncology. J Natl Compr Canc Netw. 2021;19:1441-1464.
7. Cittolin-Santos GF, Knapp B, Ganesh B, Gao F, Waqar S, Stinchcombe TE, Govindan R, Morgensztern D. The changing landscape of small cell lung cancer. Cancer. 2024;130:2453-2461.
8. Xiao W, Zheng S, Liu P, Zou Y, Xie X, Yu P, Tang H, Xie X. Risk factors and survival outcomes in patients with breast cancer and lung metastasis: a population-based study. Cancer Med. 2018;7:922-930.

Interesting Image

Mol Imaging Radionucl Ther 2026;35(1):67-69 ***DOI:****10.4274/mirt.galenos.2025.79053*

Metastatic Prostate Cancer with Pulmonary Involvement Mimicking Pneumonia: Findings on ^{18}F-FDG PET/CT and ^{68}Ga-PSMA PET/CT

Pnömoniyi Taklit Eden Akciğer Tutulum olan Metastatik Prostat Kanseri: ^{18}F-FDG PET/BT ve ^{68}Ga-PSMA PET/BT Bulguları

Nur Aydınbelge Dizdar, Ebru Tatcı, Alev Noyaner Çınar, Büşra Bozca, Özlem Özmen

University of Health Sciences Türkiye, Ankara Etlik City Hospital, Clinic of Nuclear Medicine, Ankara, Türkiye

Abstract

A 68-year-old man with progressive exertional dyspnea after an upper respiratory tract infection underwent contrast-enhanced thorax computed tomography (CT) to exclude pulmonary thromboembolism. The radiological findings suggested pneumonia or alveolar edema. ^{18}F-Fluorodeoxyglucose positron emission tomography/CT (^{18}F-FDG PET) scan was conducted due to progressive radiological findings. It revealed increased FDG uptake in the prostate gland, mediastinal, abdominopelvic multiple lymph nodes and bilateral lung lesions. ^{68}Ga- prostate-specific membrane antigen-11 (PSMA) PET/CT scan was performed due to low FDG uptake in the lymph nodes and elevated plasma total prostate-specific antigen values. Moderate to high PSMA uptake corresponded to the localizations of FDG uptake on PET/CT. Furthermore, histopathological and immunohistochemical examinations demonstrated that the bilateral lung lesions and bilateral pleural effusion were compatible with metastases from prostate adenocarcinoma.

Keywords: Prostate cancer, ^{68}Ga-PSMA PET/CT, pulmonary lymphangitic spread, pleural metastasis, pneumonia, ^{18}F-FDG PET/CT

Öz

Üst solunum yolu enfeksiyonu sonrası giderek artan efor dispnesi olan 68 yaşındaki erkek hastaya, pulmoner tromboemboliyi dışlamak için kontrastlı toraks bilgisayarlı tomografi (BT) çekildi. Radyolojik bulgular pnömoni veya alveolar ödem olduğunu düşündürdü. Radyolojik bulguların ilerlemesi nedeniyle ^{18}F-Florodeoksiglukoz pozitron emisyon tomografisi/BT (^{18}F-FDG PET) taraması yapıldı. Prostat, mediastinal ve abdominopelvik çoklu lenf düğümlerinde ve bilateral akciğer lezyonlarında FDG alımının arttığı gözlendi. Lenf düğümlerinde düşük FDG alımı ve plasmadaki yüksek total prostat spesifik antijen değerleri nedeniyle ^{68}Ga- prostat spesifik membran antijeni-11 (PSMA) PET/BT taraması yapıldı. Orta-yüksek düzeyde PSMA tutulumu, PET/BT'de FDG tutulumu saptanan alanlarla korelasyon gösterdi. Ayrıca, histopatolojik ve immünohistokimyasal incelemeler, bilateral akciğer lezyonlarının ve bilateral plevral efüzyonun prostat adenokarsinomundan kaynaklanan metastazlarla uyumlu olduğunu gösterdi.

Anahtar Kelimeler: Prostat kanseri, ^{68}Ga-PSMA PET/BT, pulmoner lenfanjitik yayılım, plevral metastaz, pnömoni, ^{18}F-FDG PET/BT

Address for Correspondence: Nur Aydınbelge Dizdar, University of Health Sciences Türkiye, Ankara Etlik City Hospital, Clinic of Nuclear Medicine, Ankara, Türkiye
E-mail: fnuraydinbelge@gmail.com **ORCID ID:** orcid.org/0000-0002-9657-6906

Received: 02.09.2025 **Accepted:** 08.10.2025 **Epub:** 26.11.2025 **Publication Date:** 03.02.2026

Cite this article as: Aydınbelge Dizdar N, Tatcı E, Noyaner Çınar A, Bozca B, Özmen Ö. Metastatic prostate cancer mimicking pneumonia: findings on ^{18}F-FDG PET/CT and ^{68}Ga-PSMA PET/CT. Mol Imaging Radionucl Ther. 2026;35(1):67-69.

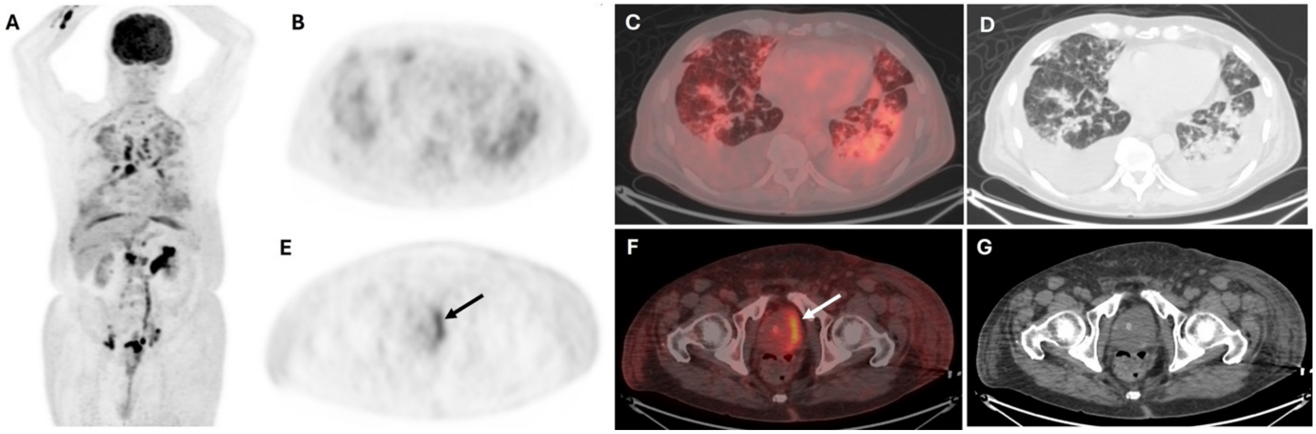

Figure 1. Following an upper respiratory tract infection, a 68-year-old man with progressive exertional dyspnea underwent contrast-enhanced thorax computed tomography (CT) to exclude pulmonary thromboembolism. It was revealed that there was bilateral moderate pleural effusion, enlarged mediastinal lymph nodes, diffuse ground-glass opacities, interlobular septal thickening, consolidations, and atelectasis in bilateral lungs. Although the patient was treated with antibiotics and corticosteroids, the progression of radiological findings was observed in follow-up thorax CT performed due to increasing dyspnea. For further assessment, ^{18}F-Fluorodeoxyglucose positron emission tomography (^{18}F-FDG PET)/CT scan was conducted. It displayed mild to high FDG uptake in multiple mediastinal and intra-abdominal lymph nodes, as well as mild FDG uptake in bilateral lung lesions (A, maximum intensity projection image; B, PET image; C, fused PET/CT image; D, CT image). Mild FDG uptake in the prostate gland (arrow) (maximum standardized uptake values: 5.2), high FDG uptake in the location between the left lateral wall of the urinary bladder and the left side of the prostate gland were incidentally observed (E, PET image; F, fused PET/CT image; G, CT image).

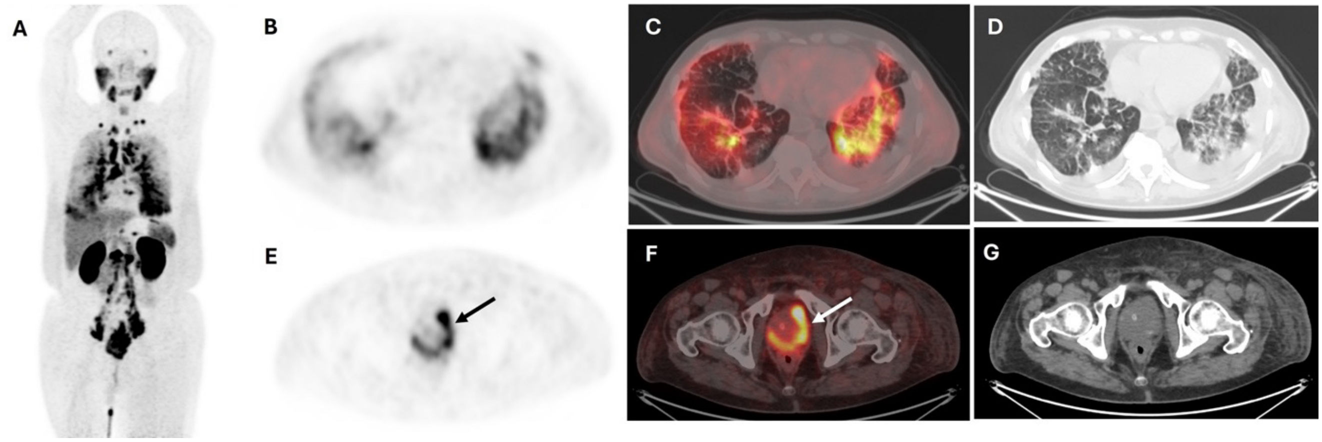

Figure 2. Due to low fluorodeoxyglucose (FDG) uptake in the lymph nodes and a markedly elevated plasma total prostate-specific antigen level of 523 µg/L (normal: <4.1 µg/L), a prostate fine-needle biopsy was performed and confirmed prostate adenocarcinoma (PCa). ^{68}Ga-prostate-specific membrane antigen-11 positron emission tomography/computed tomography (PSMA PET/CT) was conducted. It showed mild to high PSMA uptake bilateral lung lesions and multiple lymph nodes (A, maximum intensity projection image; B, PET image; C, fused PET/CT image; D, CT image). It demonstrated increased PSMA uptake (maximum standardized uptake values, 14.1) extending from the prostate gland (arrow) to the urinary bladder and rectum (E, PET image; F, fused PET/CT image; G, CT image). Afterwards, immunohistochemical and histopathological assessments of the pleural fluid and bronchioalveolar lavage were consistent with prostate cancer (PCa) metastasis.

PSMA-ligand PET/CT plays a crucial role in detecting biochemical recurrence and staging intermediate- to high-risk PCa (1). In the diagnosis and staging of primary PCa, the role of ^{18}F-FDG PET/CT is considerably limited (2,3). Therefore, integrating PSMA-ligand PET/CT and ^{18}F-FDG PET/CT can provide a more comprehensive assessment of metastatic disease, particularly in atypical presentations.

PCa may metastasize the lungs, most commonly presenting with nodular involvement. Pulmonary lymphangitic spread (PLC) with ground-glass opacities, bilateral malignant pleural effusions, and thickenings in PCa are exceedingly rare (4,5,6). Pulmonary metastases from PCa may be overlooked on conventional imaging, particularly in patients with non-specific respiratory symptoms. Furthermore, both pulmonary metastases from PCa and certain benign or malignant lung diseases may demonstrate increased uptake of FDG and PSMA radiotracers (7).

In this case, ^{18}F-FDG PET/CT revealed pathological radiotracer uptake in the prostate gland preceding both symptomatic presentation and laboratory findings. However, ^{68}Ga-PSMA PET/CT provided superior accuracy in determining the extent of disease spread, thereby enabling informed treatment planning. Therefore, it should always be considered that bilateral pleural effusion and PLC with ground-grass opacity may represent metastatic spread from PCa, even in patients without a prior history of malignancy.

Ethics

Informed Consent: Written informed consent was obtained from the patient.

Footnotes

Authorship Contributions

Surgical and Medical Practices: N.A.D., Concept: E.T., A.N.Ç., Ö.Ö., Data Collection or Processing: E.T., A.N.Ç., Analysis or Interpretation: N.A.D., Ö.Ö., Literature Search: A.N.Ç., B.B., Writing: N.A.D.

Conflict of Interest: No conflicts of interest were declared by the authors.

Financial Disclosure: The authors declare that this study has received no financial support.

References

1. Sachpekidis C, Alberts I, Rominger A, Afshar-Oromieh A. ^{68}Ga-prostate-specific membrane antigen uptake in a malignant pleural effusion from metastatic prostate cancer after pleurodesis. Clin Nucl Med. 2019;44:838-839.
2. Jadvar H. Imaging evaluation of prostate cancer with ^{18}F-fluorodeoxyglucose PET/CT: utility and limitations. Eur J Nucl Med Mol Imaging. 2013;40 (Suppl 1):S5-S10.
3. Makis W, Ciarallo A. Clinical significance of ^{18}F-fluorodeoxyglucose avid prostate gland incidentalomas on positron emission tomography/computed tomography. Mol Imaging Radionucl Ther. 2017;26:76-82.
4. Skrobisz K, Miszewski K, Miszewska L, Bieńkowski M, Matuszewski M, Studniarek M. Pleural metastasis as an initial presentation of prostate cancer: case report and literature review. Diagnostics. 2025;15:666.
5. Hibino M, Maeda K, Horiuchi S, Fukuda M, Kondo T. Pulmonary lymphangitic carcinomatosis with ground-glass opacities as presentation of prostate cancer. Respirol Case Rep. 2018;6:e00347.
6. Knight JC, Ray MA, Benzaquen S. Malignant pleural effusion from prostate adenocarcinoma. Respir Med Case Rep. 2014;13:24-25.
7. Srinivasan R, Cook GJR, Patel N, Subesinghe M. Prostate specific membrane antigen (PSMA) avid nonprostatic benign and malignant disease: a pictorial review. Clin Radiol. 2024;79:639-656.

Interesting Image

Mol Imaging Radionucl Ther 2026;35(1):70-72 ***DOI:****10.4274/mirt.galenos.2025.91069*

Intense FAPI Uptake of Pancreatic Tissue Can Mask the Tumor Activity of Pancreatic Cancer: The Importance of Dual-Tracer PET Imaging

Pankreatik Dokunun Yoğun FAPI Tutulumu Pankreas Kanserinin Tümör Aktivitesini Maskeleyebilir: Çift İzleyici PET Görüntülemenin Önemi

Elife Akgün[1], Ahmet Ertuğrul Öztürk[1], Göksel Alçın[1], Mert Mahsuni Sevinç[2], Esra Arslan[1]

[1]*University of Health Sciences Türkiye, İstanbul Training and Research Hospital, Clinic of Nuclear Medicine, İstanbul, Türkiye*
[2]*University of Health Sciences Türkiye, İstanbul Training and Research Hospital, Clinic of General Surgery, İstanbul, Türkiye*

Abstract

Fibroblast activation protein (FAPI), a type II transmembrane glycoprotein is a promising target to image epithelial originated cancers. Pancreatic cancer is characterized with [^{68}Ga]Ga-FAPI-04 and ^{18}F-fluorodeoxyglucose (^{18}F-FDG) uptake in varying degree. However physiologic uptake and uptake associated with acute/chronic pancreatitis makes interpretation challenging. We would like to present a case of pancreatic cancer whose tumor could not delineated from rest pancreatic tissue in [^{68}Ga]Ga-FAPI-04 positron emission tomography/computed tomography (PET/CT) images due to intense FAPI uptake in whole pancreas but more remarkable in ^{18}F-FDG PET/CT images.

Keywords: FAPI, Gallium-68, pancreatic cancer, FDG, PET/CT

Öz

Tip II transmembran glikoprotein olan fibroblast aktivasyon proteini (FAPI), epitel kökenli kanserlerin görüntülenmesinde umut vadeden bir hedeftir. Pankreas kanseri, değişen derecelerde [^{68}Ga]Ga-FAPI-04 ve ^{18}F-florodeoksiglukoz (^{18}F-FDG) tutulumu ile karakterizedir. Ancak fizyolojik tutulum ve akut/kronik pankreatit ile ilişkili tutulum, yorumlamayı zorlaştırır. Tümörünün tüm pankreasın tamamında yoğun FAPI tutulumu olmasına rağmen ^{18}F-FDG pozitron emisyon tomografisi/bilgisayarlı tomografi (PET/BT) görüntülerinde daha belirgin olması nedeniyle [^{68}Ga]Ga-FAPI-04 PET/BT görüntülerinde kalan pankreas dokusundan ayırt edilemediği bir pankreas kanseri vakasını sunmak istiyoruz.

Anahtar Kelimeler: FAPI, Galyum-68, pankreas kanseri, FDG, PET/BT

Address for Correspondence: Elife Akgün, University of Health Sciences Türkiye, İstanbul Training and Research Hospital, Clinic of Nuclear Medicine, İstanbul, Türkiye
E-mail: elifekaymak@hotmail.com **ORCID ID:** orcid.org/0000-0001-5625-9749

Received: 27.04.2025 **Accepted:** 12.10.2025 **Epub:** 15.01.2026 **Publication Date:** 03.02.2026

Cite this article as: Akgün E, Öztürk AE, Alçın G, Sevinç MM, Arslan E. Intense FAPI uptake of pancreatic tissue can mask the tumor activity of pancreatic cancer: the importance of dual-tracer PET imaging. Mol Imaging Radionucl Ther. 2026;35(1):70-72.

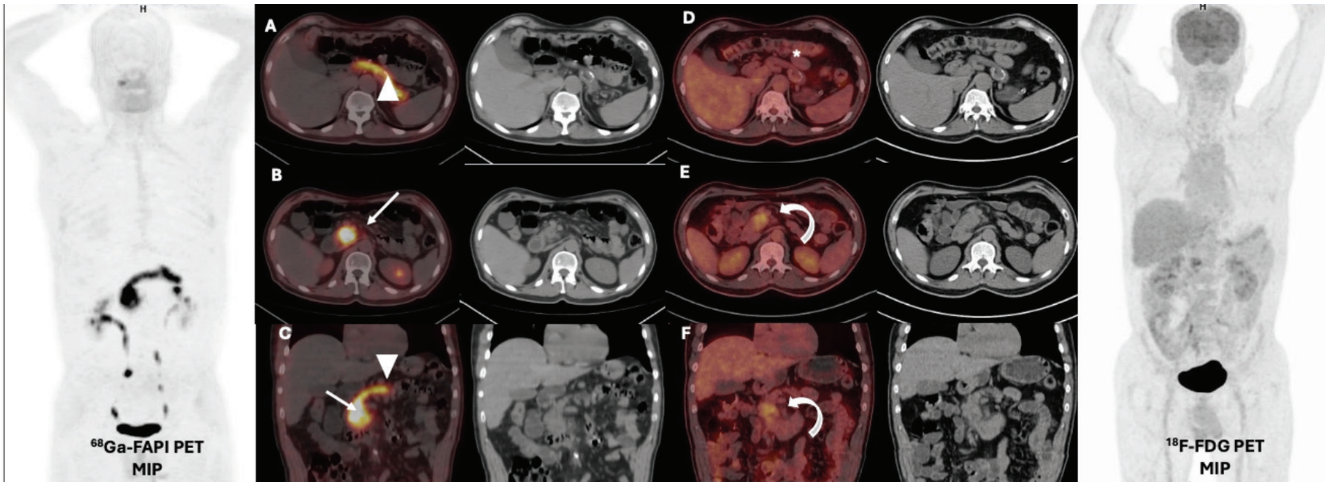

Figure 1. Fifty-eight-year-old man presented with abdominal pain. The clinician did not reveal any findings requiring urgent abdominal surgery with clinic examination. Abnormal laboratory test results were; carcinoembryonic antigen: 32.3 mg/L (normal mg/l <3), cancer antigen 125: 42.9 u/mL (normal <35 u/mL), carbohydrate antigen 19-9: 16065 U/mL (normal <35 U/mL). Abdominal magnetic resonance imaging confirmed the pancreatic head located tumoral lesion with malignancy suspicion. Upon this, the clinician planned ^{18}F-fluorodeoxyglucose positron emission tomography/computed tomography (^{18}F-FDG PET/CT) for initial staging. In order not to waste time, the patient with uncontrollable hyperglycemia (fasting blood glucose level was over 350 mg/dL), underwent [^{68}Ga]Ga-fibroblast activation protein (FAPI)-04 PET/CT imaging (line A, B, C). Whole pancreatic tissue showed diffuse intense [^{68}Ga]Ga-FAPI-04 uptake (line A and C; arrow-head). The tumor could not be discriminated from the rest of pancreas tissue on PET images (line B and C; arrow). After controlling of the fasting-blood glucose level ^{18}F-FDG PET/CT performed (line D, E, F). Pancreatic head located tumor showed mild ^{18}F-FDG uptake (line E and F; curved-arrow). However, rest of the pancreatic tissue did not show pathological activity uptake neither focal nor diffuse (line D; asterix). It is accepted as an important finding to exclude the tumor induced acute pancreatitis.

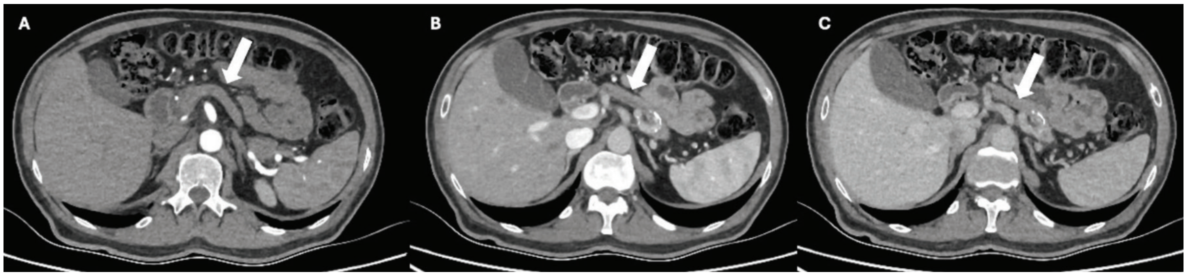

Figure 2. Clinic examination findings, laboratory test results did not point acute pancreatitis [amylase: 45.8 U/L (28-100), lipase: 13.3 U/L (0-67) aspartate aminotransferase: 18 U/L (0-50), alanine aminotransferase: 22 U/L (0-50) C-reactive protein: 0.4 mg/L (0-5), white blood cell: 7.02 10^9/L (4-10)]. No findings, such as swelling, peripancreatic fluid, abnormal enhancing, fat stranding, suggestive of acute pancreatitis were detected in contrast-enhanced abdominal computed tomography (CT) images (A: arterial phase, B: portal venous phase, C: delayed phase; arrows). Body and tail part of the pancreatic tissue was atrophic. Histopathologic examination of the pancreatic head located tumor was consistent with adenocarcinoma. Neoadjuvant chemotherapy was planned.

In this case due to high [^{68}Ga]Ga- fibroblast activation protein (FAPI)-04 uptake in the whole pancreatic tissue delineating the tumor from non-cancerous parenchyma was not possible. Although tumor showed low degree hypermetabolism, the tumor border was clearer in ^{18}F-fluorodeoxyglucose positron emission tomography (^{18}F-FDG PET) images compared with [^{68}Ga]Ga-FAPI-04 PET images.

[^{68}Ga]Ga-FAPI-04 has several advantages over ^{18}F-FDG PET in terms of patient preparation. [^{68}Ga]Ga-FAPI-04 PET is a promising alternative to ^{18}F-FDG PET in cases with uncontrolled hyperglycemia like ours'. Superiority of [^{68}Ga]Ga-FAPI-04 PET in most epithelial cancer originating from the gastrointestinal tract especially in identifying lymph nodes and peritoneal metastasis have shown in the literature (2-4). Similar to ^{18}F-FDG, both focal and diffuse [^{68}Ga]Ga-FAPI-04 uptakes are a pitfall in cases with pancreatic carcinoma suspicion. Non-cancerous pathology of the pancreas could show high [^{68}Ga]Ga-FAPI-04 uptake (5,6). Moreover, tumor induced acute pancreatitis made more complex the delineation of the tumor (7). Non-specific prominent [^{68}Ga]Ga-FAPI-04 uptake compared with ^{18}F-FDG could be detected probably due to fibrotic or chronic inflammatory changes of pancreas (8). In most cases, the physiologic [^{68}Ga]Ga-FAPI-04 uptake of pancreas is lower compared with ^{18}F-FDG (1). There is limited data in the literature suggesting that high-degree [^{68}Ga]Ga-FAPI-04 uptake in pancreatitis may mask the tumor (7). Our case was diagnosed with diabetes and pancreas appeared atrophic on CT images. Both findings could support chronic pancreatitis. In our case, diffuse intense [^{68}Ga]Ga-FAPI-04 uptake and low-grade ^{18}F-FDG uptake were thought to be secondary to chronic pancreatitis inducing fibrosis. [^{68}Ga]Ga-FAPI-04 uptake in the fibrotic tissue is well known in literature. In selected cases, dual-tracer PET imaging could increase our knowledge about the cancer and concomitant pathologies.

Ethics

Informed Consent: Informed consent was obtained from all subjects involved in the study.

Footnotes

Authorship Contributions

Surgical and Medical Practices: E.A., A.E.Ö., G.A., M.M.S., Es.A., Concept: E.A., Design: E.A., Es.A., Data Collection or Processing: E.A., M.M.S., Analysis or Interpretation: E.A., M.M.S., Literature Search: E.A., A.E.Ö., Writing: E.A.

Conflict of Interest: No conflicts of interest were declared by the authors.

Financial Disclosure: The authors declare that this study has received no financial support.

References

1. Giesel FL, Kratochwil C, Schlittenhardt J, Dendl K, Eiber M, Staudinger F, Kessler L, Fendler WP, Lindner T, Koerber SA, Cardinale J, Sennung D, Roehrich M, Debus J, Sathekge M, Haberkorn U, Calais J, Serfling S, Buck AL. Head-to-head intra-individual comparison of biodistribution and tumor uptake of ^{68}Ga-FAPI and ^{18}F-FDG PET/CT in cancer patients. Eur J Nucl Med Mol Imaging. 2021;48:4377-4385.
2. Pang Y, Zhao L, Shang Q, Meng T, Zhao L, Feng L, Wang S, Guo P, Wu X, Lin Q, Wu H, Huang W, Sun L, Chen H. Positron emission tomography and computed tomography with [^{68}Ga]Ga-fibroblast activation protein inhibitors improves tumor detection and staging in patients with pancreatic cancer. Eur J Nucl Med Mol Imaging. 2021;49:1322-1337.
3. Pang Y, Zhao L, Luo Z, Hao B, Wu H, Lin Q, Sun L, Chen H. Comparison of ^{68}Ga-FAPI and ^{18}F-FDG uptake in gastric, duodenal, and colorectal cancers. Radiology. 2021;298:393-402.
4. Gündoğan C, Kömek H, Can C, Yildirim ÖA, Kaplan İ, Erdur E, Poyraz K, Güzel Y, Oruç Z, Çakabay B. Comparison of ^{18}F-FDG PET/CT and ^{68}Ga-FAPI-04 PET/CT in the staging and restaging of gastric adenocarcinoma. Nucl Med Commun. 2022;43:64-72.
5. Veldhuijzen van Zanten SEM, Pieterman KJ, Wijnhoven BPL, Pruis IJ, Groot Koerkamp B, van Driel LMJW, Verburg FA, Thomeer MGJ. FAPI PET versus FDG PET, CT or MRI for staging pancreatic-, gastric- and cholangiocarcinoma: systematic review and head-to-head comparisons of diagnostic performances. Diagnostics (Basel). 2022;12:1958.
6. Shou Y, Xue Q, Yuan J, Zhao J. ^{68}Ga-FAPI-04 PET/MR is helpful in differential diagnosis of pancreatitis from pancreatic malignancy compared to ^{18}F-FDG PET/CT: a case report. Eur J Hybrid Imaging. 2021;5:12.
7. Luo Y, Pan Q, Zhang W, Li F. Intense FAPI uptake in ınflammation may mask the tumor activity of pancreatic cancer in ^{68}Ga-FAPI PET/CT. Clin Nucl Med. 2020;45:310-311.
8. Li Y, Gao J, Li Y, Duan X, Shen C. Non-specific uptake of ^{18}F-FAPI-04 in the pancreas and its related factors: a post-hoc analysis of an ongoing prospective clinical trial. Sci Rep. 2024;14:11141.

Case Report

Mol Imaging Radionucl Ther 2026;35(1):73-77 ***DOI:****10.4274/mirt.galenos.2025.58966*

The Complementary Roles of ^{18}F-Fluorocholine and ^{18}F-Fluorodeoxyglucose Positron Emission Tomography/ Computed Tomography in an Evaluation of A Patient With Parathyroid Carcinoma: A Case Report

Paratiroid Karsinomlu Bir Hastanın Değerlendirilmesinde ^{18}F-Florokolin ve ^{18}F-Florodeoksiglukoz Pozitron Emisyon Tomografi/Bilgisayarlı Tomografinin Tamamlayıcı Rolleri: Bir Olgu Sunumu

Nikola Pantic[1], Lenka Grujicic[1], Branislava Radovic[1,3], Dragana Sobic Saranovic[1,2], Vera Artiko[1,2], Strahinja Odalovic[1,2]

[1]*University Clinical Center of Serbia, Center for Nuclear Medicine with PET, Belgrade, Serbia*
[2]*University of Belgrade Faculty of Medicine, Department of Nuclear Medicine, Belgrade, Serbia*
[3]*University of Pristina Faculty of Medicine, Department of Internal Medicine, Kosovska Mitrovica, Serbia*

Abstract

^{18}Fluorine-fluorocholine (^{18}F-FCH) is a radiopharmaceutical used in primary hyperparathyroidism. The data about its utility in malignancies other than prostate and hepatocellular carcinoma is limited. We present the case of a patient who was referred for ^{18}F-FCH positron emission tomography/ computed tomography (PET/CT) due to the persistently elevated parathormone and calcium levels following total thyroidectomy with left lower parathyroidectomy for parathyroid carcinoma (PTC). Previously, the patient underwent ^{18}Fluorine-fluorodeoxyglucose (^{18}F-FDG) PET/CT. The latter method detected multiple mediastinal and hilar lymph nodes, as well as nodular lesions in lungs and osteolytic bone lesions with an increased tracer uptake, whereas ^{18}F-FCH PET/CT detected an increased tracer uptake not only in lesions at all of the abovementioned areas, but also in the nodular lesion in the neck corresponding to a local relapse as well, with bone lesions showing higher avidity for ^{18}F-FDG than for ^{18}F-FCH. The case we present shows that ^{18}F-FCH PET/CT has an additive value to ^{18}F-FDG PET/CT in an evaluation of patients with PTC.

Keywords: Parathyroid carcinoma, primary hyperparathyroidism, positron-emission tomography, ^{18}F-fluorocholine, ^{18}F-fluorodeoxyglucose

Öz

^{18}F- florokolin (^{18}F-FCH), primer hiperparatiroidizmde kullanılan bir radyofarmasötiktir. Prostat ve hepatosellüler karsinom dışındaki malignitelerdeki kullanımıyla ilgili veriler sınırlıdır. Bu yazıda, total tiroidektomi ve sol alt paratiroidektomi sonrası paratiroid karsinomu nedeniyle sürekli yüksek seyreden parathormon ve kalsiyum düzeyleri olan bir hastanın ^{18}F-FCH pozitron emisyon tomografi/bilgisayarlı tomografi (PET/BT) incelemesi için yönlendirilmesi üzerine bir vaka sunulmaktadır. Hastaya daha önce ^{18}F-florodeoksiglukoz (^{18}F-FDG) PET/BT yapılmıştı. Bu yöntem mediastinal ve

---

Address for Correspondence: Nikola Pantic, University Clinical Center of Serbia, Center for Nuclear Medicine with PET, Belgrade, Serbia
E-mail: nikolapantic944@gmail.com **ORCID ID:** orcid.org/0009-0006-6070-0828

Received: 26.12.2024 **Accepted:** 29.06.2025 **Epub:** 05.09.2025 **Publication Date:** 03.02.2026

Cite this article as: Pantic N, Grujicic L, Radovic B, Sobic Saranovic D, Artiko V, Odalovic S. The complementary roles of ^{18}F-fluorocholine and ^{18}F-fluorodeoxyglucose positron emission tomography/computed tomography in an evaluation of a patient with parathyroid carcinoma: a case report. Mol Imaging Radionucl Ther. 2026;35(1):73-77.

hiler lenf nodlarında, akciğerlerdeki nodüler lezyonlarda ve osteolitik kemik lezyonlarında artmış tutulum saptamışken, ^{18}F-FCH PET/BT hem bu bölgelerdeki lezyonlarda hem de boyunda lokal nüks ile uyumlu nodüler lezyonda artmış tutulum göstermiştir. Kemik lezyonlarında ise ^{18}F-FDG'ye göre daha düşük FCH tutulumları gözlenmiştir. Bu olguda, paratiroid karsinomu olan hastaların değerlendirilmesinde ^{18}F-FCH PET/BT'nin ^{18}F-FDG PET/BT'ye ek değer sağladığını göstermektedir.

Anahtar kelimeler: Paratiroid karsinomu, primer hiperparatiroidizm, pozitron-emisyon tomografisi, ^{18}F–florokolin, ^{18}F-florodeoksiglukoz

Introduction

Parathyroid carcinoma (PTC), as one of the rarest malignancies,accounts for less than 0.005% of all cancers and less than 1% of all parathyroid disorders (1,2). Therefore, it is a rare cause of hyperparathyroidism. ^{18}Fluorine-fluorocholine (^{18}F-FCH) is a choline analogue mimicking choline uptake and phosphorylation as a precursor in the biosynthesis of phosphatidylcholine a membrane phospholipid (3). ^{18}F-FCH positron emission tomography/computed tomography (PET/CT) is an established imaging modality for parathyroid localization in primary hyperparathyroidism (PHPT) patients. Studies show its' superior performance in comparison to conventional scintigraphic imaging, ultrasonography, or four-dimensional CT (4). The most recent study showed a sensitivity of 83%, a specificity of 97%, a positive predictive value of 90%, and a negative predictive value of 94% for ^{18}F-FCH PET/CT (5). While the utility of an ^{18}fluorine-fluorodeoxyglucose (^{18}F-FDG) PET/CT for the detection of PTC is well-known and its' sensitivity is high in all disease phases (6), data regarding the usage of ^{18}F-FCH PET/CT in the evaluation of PTC is limited. To the best of our knowledge, there are only a few case reports where ^{18}F-FCH PET/CT was used along with ^{18}F-FDG PET/CT in the evaluation of patients with PTC (7,8,9).

We present a case of a patient with PHPT who was evaluated with both ^{18}F-FCH and ^{18}F-FDG PET/CT during the diagnostic process.

Case Report

A 51-year-old male patient was referred for ^{18}F-FCH PET/CT at the Center for Nuclear Medicine with PET of the University Clinical Center of Serbia due to persistently elevated parathyroid hormone (PTH) and calcium levels following total thyroidectomy with left lower parathyroidectomy for PTC.

Eight months prior, he presented with a pathologic fracture of the left clavicle. Laboratory tests showed hypercalcemia (Ca 4.12 mmol/L, ionized Ca 2.05 mmol/L, PO_4 0.94 mmol/L, vitamin D3 21.9 nmol/L); with significantly elevated PTH levels (11561 pg/mL). The patient has a family history of parathyroid diseases, and a history of nephrolithiasis. After hospitalization, neck ultrasound identified two nodules in the left thyroid lobe. One of the nodules was occupying the majority of the lower pole of the left thyroid lobe and was 30x30 mm in size, while the other one, located caudally in relation to the first one and measuring 22x18 mm, was suspected to be an enlarged parathyroid gland. Thyroid scintigraphy with technetium-99m(Tc-99m)-pertechnetate showed non-functional nodules, while Tc-99m-sestamibi (MIBI) scintigraphy showed focal zone of an increased radiopharmaceutical uptake in the projection of the lower pole of the left thyroid lobe.

Histopathological analysis following total thyroidectomy with lower left parathyroidectomy confirmed PTC adjacent to the lower pole of the left thyroid lobe, which was 22 mm in diameter, with capsular defect, fields of hemorrhage, limited necrosis, and angioinvasion. Immunohistochemistry findings were as follows: GATA3+, CK19+ focal, HMBE1-, calcitonin-, TTF1-, thyroglobulin-, Ki67 index ~13%. A second tumor, containing remnants of the parathyroid gland with dimensions 36x25x15 mm, was identified as an atypical parathyroid adenoma.

Postoperative multi-slice CT (MSCT) of the chest revealed multiple micronodular and nodular lesions in both lungs, with the largest diameter up to 29 mm, which likely corresponded to secondary deposits, as well as multiple enlarged mediastinal lymph nodes, with the largest subcarinal node measuring 20x36 mm, and osteolytic lesions in the left scapula and left clavicle. Following chest MSCT, the patient was referred for an ^{18}F-FDG PET/CT scan for evaluation of lesions detected on MSCT and staging of the disease.

A three-dimensional PET scan (Figure 1a), associated with low-dose non-enhanced CT scan, was acquired from the base of the skull to the mid-thigh. ^{18}F-FDG-avid disease was identified in lymph nodes of the mediastinum and hila of the lungs bilaterally up to 16mm in diameter with the maximum standardized uptake value (SUV_{max}) of 8.3 (Figure 1b), multiple micronodular and nodular lesions in the lungs, which were up to 29 mm in diameter with the SUV_{max} of 14.1 (Figure 1c), as well as multiple zones of an increased metabolism of glucose in lytic lesions in femurs, pubic bones (Figures 1d, 1e), ilia, sacrum, and scapulae bilaterally, left humerus, left clavicle, sternum, and

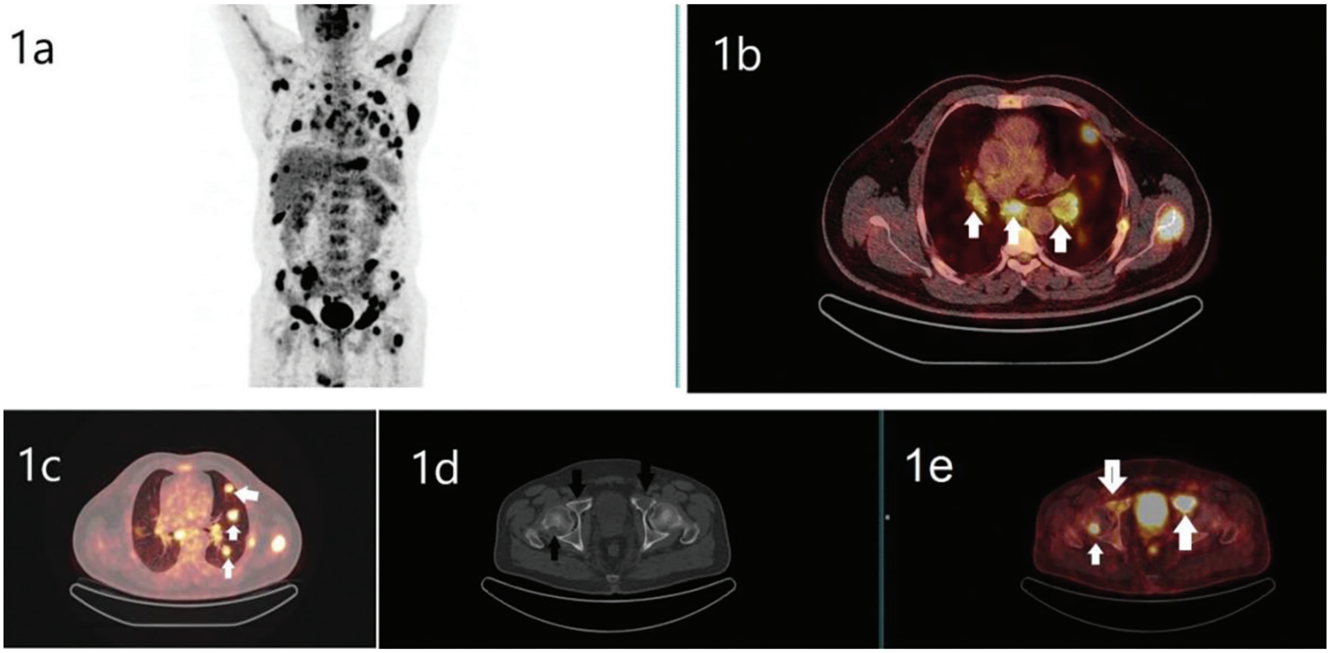

Figure 1. ^{18}Fluorine-fluorodeoxyglucose positron emission tomography/computed tomography (PET/CT): (a) - maximum intensity projection PET image depicts multiple areas of abnormal tracer uptake corresponding to metastatic disease in mediastinal and hilar lymph nodes, pulmonary, and bone lesions; (b) - axial fused image shows increased uptake in enlarged mediastinal and hilar lymph nodes (arrows); (c) - increased metabolism of glucose in pulmonary nodules (arrows); (d) - a low-dose, non-enhanced CT depicts lytic lesions in pubic bones bilaterally and the head of the right femur (black arrows); (e) - increased uptake of the radiopharmaceutical in lytic lesions on the fused image (white arrows)

multiple anterior and posterior rib ends, predominantly on the left side, with the SUV_{max} up to 14.5. All the sites of pathological uptake were interpreted as metastases, and the patient was treated with a chemotherapy regimen combining 5-fluorouracil and dacarbazine.

Due to the persistence of elevated PTH (493 pg/mL), hypercalcemia (Ca 4.05 mmol/L, ionized Ca 2.25 mmol/L), and hypophosphatemia (PO4 0.69 mmol/L), the patient underwent PET/CT with ^{18}F-FCH. A three-dimensional PET scan and a low-dose non-enhanced CT scan were acquired from the top of the head to the mid-thigh, 45 minutes following the injection of 189 MBq of ^{18}F-FCH. The examination revealed multiple sites of pathological radiopharmaceutical uptake in: pretracheal nodular lesion in proximity of the previous intervention in the neck, 22 mm in diameter with the SUV_{max} of 11.8 (Figures 2a, 2e), interpreted asa local relapse; mediastinal lymph nodes with the largest subcarinal node measuring 16x14 mm with the SUV_{max} of 4; multiple nodular lesions in the pulmonary parenchyma bilaterally, more pronounced on the left, up to 30 mm in diameter with the SUV_{max} of 7.3 (Figures 2b, 2f); osteolytic lesions, some with a soft tissue components which were up to 25mm in diameter, in right orbit, scapulae (Figures 2c, 2g) and clavicles bilaterally, ribs (Figures 2d, 2h), sternum, femurs, pelvic bones bilaterally, and sacrum. All the sites of pathological uptake were interpreted as metastases, and a chemotherapy regimen with carboplatin and etoposide was started.

Discussion

Compared with patients with benign parathyroid adenomas, patients with PTC are more symptomatic and present with significantly higher calcium and PTH levels. PTC is notably challenging to diagnose, with confirmation typically only being possible post-operatively on histopathology (10). A meta-analysis supports the use of ^{18}F-FCH over MIBI in patients with PHPT due to its higher sensitivity (11). PTC and its metastatic sites show significant avidity for ^{18}F-FDG (6), while data on the use of ^{18}F-FCH in the evaluation of patients with PTC are limited to a few cases in which ^{18}F-FCH-avid metastatic disease was detected (8,9,12,13). In the case we presented, lesions in the lungs and mediastinum were positive on both ^{18}F-FDG and ^{18}F-FCH PET/CT, while there was a nodular lesion in the neck that wasn't ^{18}F-FDG-avid but showed choline avidity. Osteolytic bone metastases have been reported in patients with PTC (14). In the case of our patient, the uptake of a radiopharmaceutical in bone lesions was higher on

^{18}F-FDG PET/CT, compared to that of ^{18}F-FCH PET/CT (Figure 3); however, they showed avidity on both examinations. It should be noted that the delay between the two PET/CT scans was four months. Meanwhile, the patient was subjected to chemotherapy, which the ^{18}F-FCH PET/CT showed to be ineffective. However, considering all of the above, this case, along with others mentioned, shows the complementary role of ^{18}F-FCH PET/CT with ^{18}F-FDG PET/CT in the staging and detection of recurrence of the disease in patients with PTC.

Conclusion

This case report demonstrates a potential additive value of ^{18}F-FCH PET/CT to ^{18}F-FDG PET/CT in an evaluation of patients with PTC.

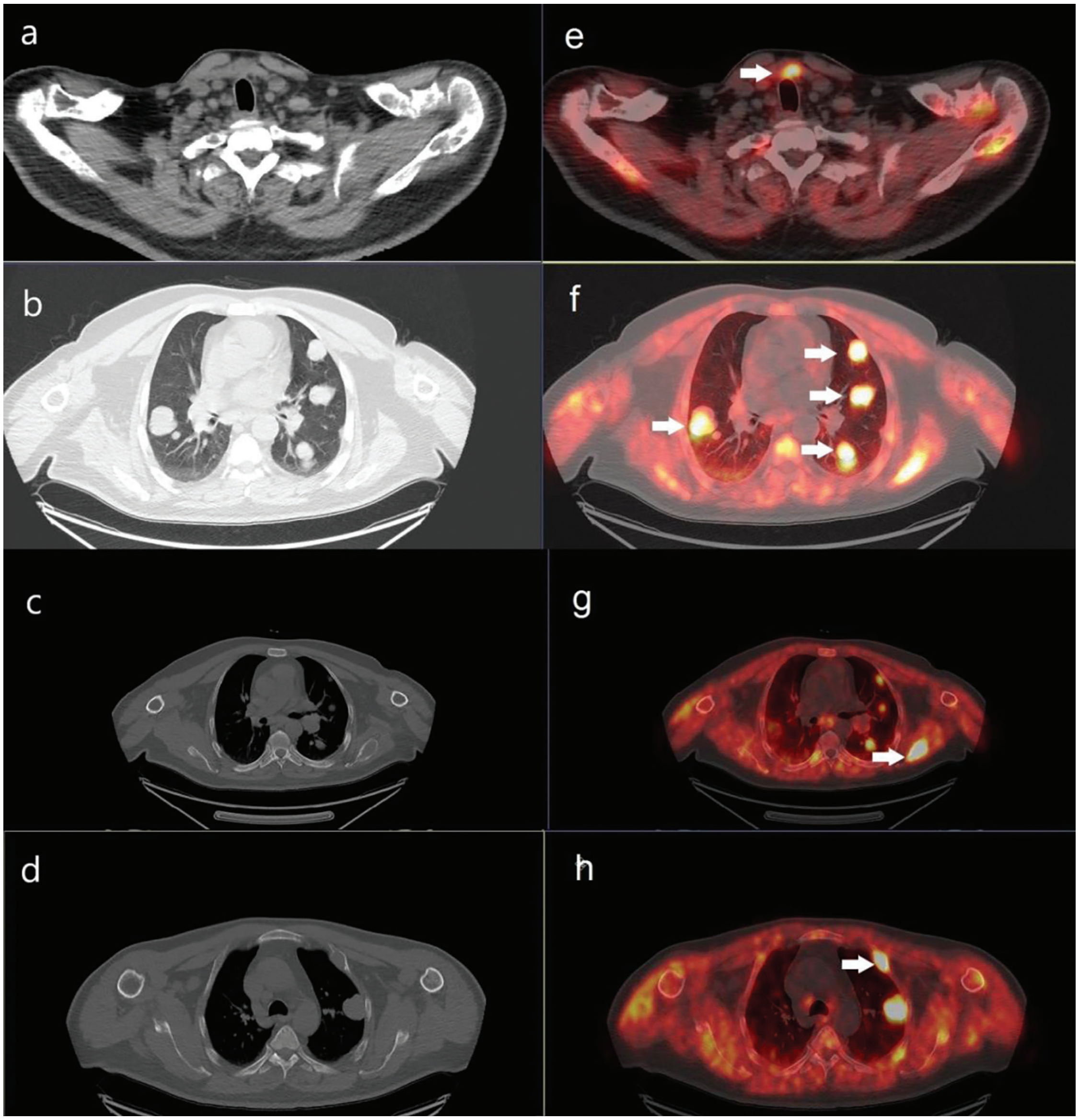

Figure 2. ^{18}Fluorine-fluorocholine positron emision tomoraphy/computed tomography: the axial images depict an increased uptake of the radiopharmaceutical in the pretracheal nodular lesion (a,e), coresponding to a local relapse; pulmonary nodules (b,f), corresponding to metastasis of the parathyroid carcinoma; osteolytic lesions in the left scapula (c,g) and the second rib on the left (d,h), coresponding to metastatic disease

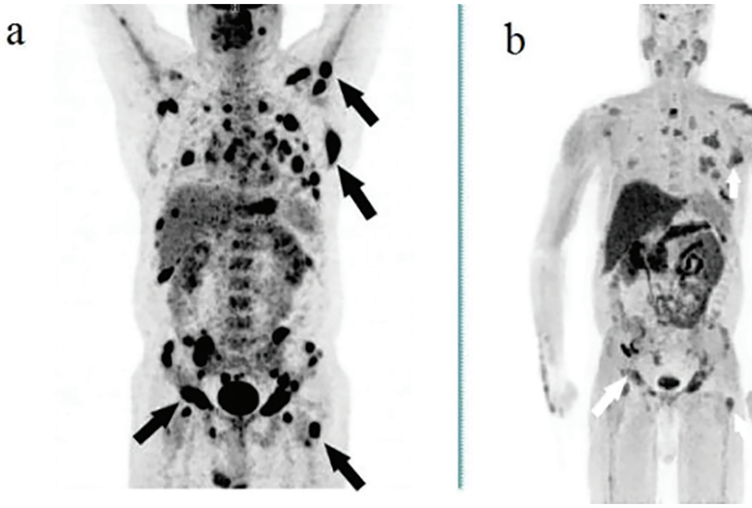

Figure 3. ^{18}Fluorine-fluorodeoxyglucose (^{18}F-FDG) and ^{18}Fluorine-fluorocholine (^{18}F-FCH) positron emission tomography (PET): maximum intensity projection PET images depict higher uptake of ^{18}F-FDG (black arrows) (a) compared to ^{18}F-FCH (white arrows) (b) in multiple bone lesions coresponding to metastatic disease

Ethics

Informed Consent: Informed consent was obtained from a patient.

Footnotes

Authorship Contributions

Surgical and Medical Practices: N.P., L.G., B.R., D.S.S., V.A., S.O., Concept: N.P., L.G., B.R., D.S.S., V.A., S.O., Design: N.P., L.G., B.R., D.S.S., V.A., S.O., Data Collection or Processing: N.P., L.G., B.R., D.S.S., V.A., S.O., Analysis or Interpretation: N.P., L.G., B.R., D.S.S., V.A., S.O., Literature Search: N.P., L.G., B.R., D.S.S., V.A., S.O., Writing: N.P., L.G., B.R., D.S.S., V.A., S.O.

Conflict of Interest: No conflicts of interest were declared by the authors.

Financial Disclosure: The authors declare that this study has received no financial support.

References

1. Fingeret AL. Contemporary evaluation and management of parathyroid carcinoma. JCO Oncol Pract. 2021;17:17-21.
2. Cappellacci F, Medas F, Canu GL, Lai ML, Conzo G, Erdas E, Calò PG. Parathyroid carcinoma in the setting of tertiary hyperparathyroidism: case report and review of the literature. Case Rep Endocrinol. 2020;2020:5710468.
3. Roland A, Drouet C, Boulahdour H, Cochet A, De Bari B. Unusual uptakes on ^{18}F-fluorocholine positron emission tomography/computed tomography (PET/CT): a retrospective study of 368 prostate cancer patients referred for a biochemical recurrence or an initial staging. Quant Imaging Med Surg. 2021;11:172-182.
4. Cuderman A, Senica K, Rep S, Hocevar M, Kocjan T, Sever MJ, Zaletel K, Lezaic L. ^{18}F-fluorocholine PET/CT in primary hyperparathyroidism: superior diagnostic performance to conventional scintigraphic imaging for localization of hyperfunctioning parathyroid glands. J Nucl Med. 2020;61:577-583.
5. Kaseb A, Benider H, Treglia G, Cusumano C, Bessac D, Trimboli P, Vix M, Piccardo A, Latgé A, Imperiale A. Refining the role of presurgical PET/4D-CT in a large series of patients with primary hyperparathyroidism undergoing [^{18}F]fluorocholine PET/CT. Eur J Clin Invest. 2024:e14336.
6. Evangelista L, Sorgato N, Torresan F, Boschin IM, Pennelli G, Saladini G, Piotto A, Rubello D, Pelizzo MR. FDG-PET/CT and parathyroid carcinoma: review of literature and illustrative case series. World J Clin Oncol. 2011;2:348-354.
7. Thanseer NTK, Parihar AS, Sood A, Bhadada SK, Dahiya D, Singh P, Mittal BR. Evaluation of recurrent parathyroid carcinoma: A new imaging tool in uncommon entity. World J Nucl Med. 2019;18:198-200.
8. Iacovitti CM, Cuzzocrea M, Gianola L, Paone G, Treglia G. Dual-tracer positron emission tomography/computed tomography with [^{18}F]FDG and [^{18}F]fluorocholine in a patient with metastatic parathyroid carcinoma. Diagnostics (Basel). 2024;14:1548.
9. Deandreis D, Terroir M, Al Ghuzlan A, Berdelou A, Lacroix L, Bidault F, Troalen F, Hartl D, Lumbroso J, Baudin E, Schlumberger M, Leboulleux S. ^{18}Fluorocholine PET/CT in parathyroid carcinoma: a new tool for disease staging? Eur J Nucl Med Mol Imaging. 2015;42:1941-1942.
10. Roser P, Leca BM, Coelho C, Schulte KM, Gilbert J, Drakou EE, Kosmas C, Ling Chuah L, Wassati H, Miras AD, Crane J, Aylwin SJB, Grossman AB, Dimitriadis GK. Diagnosis and management of parathyroid carcinoma: a state-of-the-art review. Endocr Relat Cancer. 2023;30:e220287.
11. Whitman J, Allen IE, Bergsland EK, Suh I, Hope TA. Assessment and comparison of ^{18}F-fluorocholine PET and ^{99m}Tc-sestamibi scans in identifying parathyroid adenomas: a metaanalysis. J Nucl Med. 2021;62:1285-1291.
12. Morand GB, Helmchen BM, Steinert HC, Schmid C, Broglie MA. ^{18}F-Choline-PET in parathyroid carcinoma. Oral Oncol. 2018;86:314-315.
13. Hatzl M, Röper-Kelmayr JC, Fellner FA, Gabriel M. ^{18}F-fluorocholine, ^{18}F-FDG, and ^{18}F-fluoroethyl tyrosine PET/CT in parathyroid cancer. Clin Nucl Med. 2017;42:448-450.
14. Machado NN, Wilhelm SM. Parathyroid cancer: a review. Cancers (Basel). 2019;11:1676.

Case Report

Mol Imaging Radionucl Ther 2026;35(1):78-83 ***DOI:****10.4274/mirt.galenos.2026.28863*

First Southeast Asian Experience of Terbium-161 PSMA Therapy for Metastatic Castration-Resistant Prostate Cancer (mCRPC): Quantitative Imaging and Dosimetric Approach

Metastatik Kastrasyona Dirençli Prostat Kanseri (mCRPC) için Terbiyum-161 PSMA Tedavisinin Güneydoğu Asya'daki İlk Deneyimi: Kantitatif Görüntüleme ve Dozimetrik Yaklaşım

Sasithorn Amnuaywattakorn[1], Putthiporn Charoenphun[1], Touch Ativitavas[2], Panya Pasawang[3], Kitiwat Khamwan[3], Thonnapong Thongpraparn[4], Benjapa Khiewvan[4], Ponkittiya Ruangma[5], Wichana Chamroonrat[1], Krisanat Chuamsaamarkkee[1]

[1]*Mahidol University Faculty of Medicine Ramathibodi Hospital, Department of Diagnostic and Therapeutic Radiology, Division of Nuclear Medicine, Thailand, Bangkok*
[2]*Mahidol University Faculty of Medicine Ramathibodi, Department of Medicine, Division of Medical Oncology, Thailand, Bangkok*
[3]*Chulalongkorn University Faculty of Medicine, Department of Radiology, Division of Nuclear Medicine, Thailand, Bangkok*
[4]*Mahidol University Faculty of Medicine Siriraj Hospital, Department of Radiology, Division of Nuclear Medicine, Thailand, Bangkok*
[5]*Bangkok Hospital, Clinic of Oncology Imaging, Thailand, Bangkok*

Abstract

Prostate-specific membrane antigen (PSMA)-targeted radionuclide therapy has become an established treatment option for metastatic castration-resistant prostate cancer. Although lutetium-177 (^{177}Lu) PSMA therapy has shown promising clinical benefits, terbium-161 (^{161}Tb) PSMA is an emerging theranostic agent offering potential advantages due to its combination of beta and Auger electron emissions. This work presents the first documented case in Thailand and Southeast Asia of a patient treated at Ramathibodi Hospital with ^{161}Tb-PSMA following progression on ^{177}Lu-PSMA therapy. This report describes the clinical application of this novel radiopharmaceutical, the implementation of quantitative imaging protocols, single photon emission computed tomography/computed tomography calibration processes, and absorbed dose estimations from voxel-based dosimetry that contributed to individualised treatment planning.

Keywords: Prostate cancer, terbium-161 PSMA, lutetium-177 PSMA, theranostics, SPECT calibration, dosimetry, auger electrons

---

Address for Correspondence: Krisanat Chuamsaamarkkee, Mahidol University Faculty of Medicine Ramathibodi Hospital, Department of Diagnostic and Therapeutic Radiology, Division of Nuclear Medicine, Thailand, Bangkok
E-mail: krisanat.chu@mahidol.ac.th **ORCID ID:** orcid.org/0000-0002-0362-9125

Received: 11.11.2025 **Accepted:** 03.01.2026 **Publication Date:** 03.02.2026

Cite this article as: Amnuaywattakorn S, Charoenphun P, Ativitavas T, Pasawang P, Khamwan K, Thongpraparn T, Khiewvan B, Ruangma P, Chamroonrat W, Chuamsaamarkkee K. First Southeast Asian experience of terbium-161 PSMA therapy for metastatic castration-resistant prostate cancer (mCRPC): quantitative imaging and dosimetric approach. Mol Imaging Radionucl Ther. 2026;35(1):78-83.

Öz

Prostat spesifik membran antijeni (PSMA) hedefli radyonüklid tedavisi, metastatik kastrasyona dirençli prostat kanseri için yerleşik bir tedavi seçeneği haline gelmiştir. Lutetyum-177 (^{177}Lu) PSMA tedavisi umut verici klinik faydalar göstermiş olsa da, beta ve Auger elektron emisyonlarının birleşimi sayesinde potansiyel avantajlar sunan terbiyum-161 (^{161}Tb) PSMA, gelişmekte olan bir teranostik ajandır. Bu çalışma, ^{177}Lu-PSMA tedavisi sonrasında progresyon gelişen ve Ramathibodi Hastanesi'nde ^{161}Tb-PSMA ile tedavi edilen bir hastaya ait, Tayland ve Güneydoğu Asya'daki ilk belgelenmiş olguyu sunmaktadır. Bu rapor, söz konusu yeni radyofarmasötiğin klinik uygulamasını, kantitatif görüntüleme protokollerinin hayata geçirilmesini, tek foton emisyon bilgisayarlı tomografi/bilgisayarlı tomografi kalibrasyon süreçlerini ve bireyselleştirilmiş tedavi planlamasına katkı sağlayan voksel tabanlı dozimetriye dayalı soğurulan doz hesaplamalarını tanımlamaktadır.

Anahtar kelimeler: Prostat kanseri, terbiyum-161 PSMA, lutetyum-177 PSMA, teranostik, SPECT kalibrasyonu, dozimetri, auger elektronları

Introduction

Metastatic castration-resistant prostate cancer (mCRPC) remains a major clinical challenge, characterised by progression despite androgen deprivation therapy (ADT) and the use of second-line systemic treatments (1,2). Theranostic approaches targeting the prostate-specific membrane antigen (PSMA) with radiolabelled compounds, such as lutetium-177 (^{177}Lu)-PSMA, have demonstrated significant therapeutic benefits. However, a subset of patients ultimately develops resistance or progresses despite multiple cycles of ^{177}Lu-PSMA therapy (3).

Terbium-161 (^{161}Tb)-PSMA is a novel radionuclide offering theoretical advantages over ^{177}Lu-PSMA, including higher linear energy transfer and the emission of conversion and Auger electrons, which may enhance therapeutic efficacy, particularly in small-volume or micro-metastatic disease. However, clinical data on ^{161}Tb-PSMA therapy remain extremely limited, especially in Southeast Asia (1,4,5).

This report presents the first clinical application of ^{161}Tb-PSMA therapy in Thailand and Southeast Asia, providing early insights into integrating quantitative single photon emission computed tomography (SPECT) imaging and the voxel-based absorbed dose estimation in the therapeutic process.

Case Report

A 68-year-old male was initially diagnosed with locally advanced prostate cancer in 2006 and received pelvic external beam radiation therapy combined with brachytherapy, followed by ADT. In 2017, a solitary PSMA-avid mediastinal nodal metastasis was detected and managed with stereotactic body radiation therapy (SBRT). However, disease recurrence was observed in 2019, prompting the initiation of ^{177}Lu-PSMA radioligand therapy. The patient subsequently underwent 13 cycles of ^{177}Lu-PSMA therapy (administered at 150-200 mCi per cycle), with treatment continuing until June 2024. During the first 10 cycles of ^{177}Lu-PSMA therapy, metastatic disease was confined to lymph node and pulmonary involvement, without evidence of skeletal metastases.

In parallel, systemic chemotherapy was introduced, docetaxel in 2022 and cabazitaxel in 2024, the latter completed in December 2024. Interval development of bone oligo-metastases at the lumbar, vertebra and left iliac bone was identified on 11th post-therapy ^{177}Lu-PSMA imaging in March 2024. These two skeletal lesions were treated with SBRT. However, subsequent imaging after the 12th and 13th cycles of ^{177}Lu-PSMA demonstrated progression of bone metastases, indicating treatment resistance. Consequently, second-line chemotherapy with cabazitaxel was initiated.

Despite these interventions, disease progression was noted under the mCRPC setting. Galium-68 PSMA positron emission tomography combined with computed tomography scan in January 2025 demonstrated further disease progression with multiple PSMA-avid bone metastases, in addition to widespread involvement of the supraclavicular and mediastinal lymph nodes, pulmonary parenchyma, and skeletal system, along with rising prostate-specific antigen (PSA) levels. The most symptomatic lesion was located in the right femur, where the patient reported nocturnal pain with a numeric rating scale score of 5 out of 10. Analgesic management included tramadol and non-steroidal anti-inflammatory drugs (NSAIDs).

Given the exhausted therapeutic options and persistent disease activity, the patient was selected for treatment with ^{161}Tb-PSMA, which commenced in February 2025. Pre-treatment imaging confirmed extensive PSMA-avid lesions without any contraindications to therapy. Baseline laboratory investigations, including renal and hematologic parameters, were within acceptable limits and monitored closely throughout the treatment process.

Written informed consent was obtained from the patient for the publication of this short communication and any accompanying images. All identifiable information has been anonymised to protect the patient's privacy.

Radiopharmaceutical Preparation and Administration

^{161}Tb was obtained from TerThera BV, Germany, and prepared at Bangkok Hospital. Radiolabelling with PSMA-I&T ligand was performed using a protocol adapted from ^{177}Lu-PSMA procedures, with modifications to minimise radiolysis (6). The process was carried out under good manufacturing practice quality-controlled conditions. Radiochemical purity assessed by instant thin layer chromatography was 99.7% (acceptance criterion ≥95%), with an R_f value of 0.8 confirming radiochemical identity. Quality control testing demonstrated acceptable pH 4.5 (normal range 4.5-5.5), low bacterial endotoxin levels (<5.0 EU/mL), and satisfactory filter integrity, indicating adequate product stability prior to administration. Following completion of quality control, the radiopharmaceutical was transported to Ramathibodi Hospital. A total activity of 6283 MBq (169.81 mCi) of ^{161}Tb-PSMA was administered intravenously to the patient.

SPECT Calibration

Since ^{161}Tb is not included in the standard isotope libraries of most commercially available SPECT/computed tomography (CT) systems, a customised calibration protocol was established to enable accurate quantitative imaging. All imaging procedures were conducted using a dual-head hybrid SPECT/CT scanner (GE Discovery 870 DR, GE Healthcare, MI, USA) equipped with a Low-Energy High-Resolution collimator at Ramathibodi Hospital. Energy window settings were optimised for ^{161}Tb detection. The primary photopeak was centred at 74.6 keV with a ±10% energy window, and the lower and upper scatter correction windows were set at 63 keV±6% and 88 keV±6%.

Intrinsic calibration of the SPECT system was performed using both a point source and a flood source of ^{161}Tb. A small-volume point source was prepared to assess energy peak alignment and system sensitivity, while a flood source of ^{161}Tb was used to evaluate detector uniformity across the field of view. These steps ensured that calibration conditions closely matched the specific emission characteristics of ^{161}Tb.

An extrinsic flood calibration was also conducted to correct potential system nonuniformities introduced by the collimator-detector assembly. For quantitative SPECT, planar system sensitivity was determined by imaging a petri dish filled with a known activity of ^{161}Tb solution, containing approximately 37 MBq (1 mCi), following the NEMA NU1-2012 protocol. Activity measurements were verified with a radionuclide activity calibrator to ensure precise sensitivity calculations.

Post-therapeutic Imaging Protocol

Post-therapeutic quantitative SPECT/CT imaging was performed following administration of ^{161}Tb-PSMA, using acquisition settings based on the calibration previously described. SPECT/CT imaging was conducted at 2 hours, 24 hours, and 96 hours post administration.

SPECT acquisition was performed with 10 seconds per frame across all imaging sessions using a matrix size of 128 × 128 pixels, and the view angle was set at 3 degrees, 60 projections per detector, for a total of 180 projections. For this patient, four overlapping bed positions were acquired per session, with each bed position requiring approximately 15 minutes of scan time. A low-dose CT scan was performed for attenuation correction and anatomical localisation.

Quantitative SPECT image reconstruction was performed with the assistance of the MIM Software technical team and the local GE Healthcare support staff. Reconstruction was performed using an Ordered Subset Expectation Maximisation algorithm with 4 iterations and 10 subsets and applying corrections for attenuation and scatter. No post-reconstruction filtering was applied to preserve the voxel-level quantitative accuracy required for dosimetric analysis. Voxel activity concentrations were calibrated based on the planar sensitivity measurements previously established during system calibration.

Absorbed Dose Calculation

Voxel-based absorbed dose calculations were performed using the Hermes Medical Solutions software, under a research collaboration agreement between the institution and Hermes Medical Solutions (Hermia, Sweden). The absorbed dose analysis utilised the Voxel Dosimetry module, version 3.1.

Organ and tumour segmentations were generated using the software's automatic AI-based segmentation tools to facilitate consistent and efficient volume delineation. Absorbed dose calculations were performed using a Monte Carlo simulation method integrated within the Voxel Dosimetry workflow.

Discussion

Post-therapeutic quantitative SPECT/CT imaging following ^{161}Tb-PSMA therapy (6283 MBq or 169.81 mCi) enabled voxel-based dosimetry using AI-assisted segmentation (Figure 1). The absorbed dose distribution effectively targeted PSMA-avid lesions while maintaining acceptable radiation exposure to normal organs. This favourable tumor-to-organ dose distribution is consistent with recently reported multicentre clinical experience with ^{161}Tb-PSMA, which demonstrated safe organ dosimetry and promising antitumor activity even in patients refractory to prior ^{177}Lu-PSMA therapy (7).

The mean absorbed dose to the kidneys was 1.83 Gy, with 1.97 Gy delivered to the left kidney and 1.69 Gy to the right kidney, both remaining well below established renal tolerance thresholds. Other organs received relatively low absorbed doses, including 0.48 Gy to the liver and 0.63 Gy to the spleen. Lung doses were asymmetrical, with 3.61 Gy to the left lung corresponding to metastatic involvement and 0.49 Gy to the right lung. Skeletal lesions exhibited the highest absorbed doses, with the lesion in the left femur receiving 6.51 Gy and the lumbar spine lesion 5.23 Gy, as summarised in Figure 2, which includes the AI-assisted organ segmentation. Comparable organ absorbed doses and higher lesion doses have been reported in multicentre studies, supporting the therapeutic selectivity of ^{161}Tb-PSMA while maintaining organ safety margins (7).

An intra-patient comparison of renal dosimetry was undertaken between the 12th treatment cycle with ^{177}Lu-PSMA in March 2024 and the 14th cycle with ^{161}Tb-PSMA in February 2025, as illustrated in Table 1. For the ^{177}Lu-PSMA cycle, dosimetry was performed using a single time-point (STP) based on the Hänscheid approach, with quantitative SPECT/CT imaging obtained approximately 48 hours post-administration. The mean kidney absorbed dose was 1.84 Gy, corresponding to a dose-per-activity ratio of 0.22 mGy/MBq. In contrast, the ^{161}Tb-PSMA therapy incorporated a multiple time-point imaging protocol, as STP models for ^{161}Tb-PSMA are not yet established. Despite methodological differences, the mean kidney absorbed dose during the ^{161}Tb-PSMA cycle remained comparable at 1.83 Gy. However, the mean absorbed dose per administered activity was slightly higher at 0.29 mGy/MBq.

This observation aligns with published dosimetric data showing that ^{161}Tb-PSMA may deliver similar macroscopic organ doses to ^{177}Lu-PSMA while potentially providing enhanced microscopic dose deposition due to the emission of short-range Auger electrons (7). The modest increase in dose-per-activity in the present case may also reflect differences in disease burden and radiopharmaceutical kinetics, as the patient demonstrated more advanced disease progression at the time of ^{161}Tb-PSMA therapy. Previous studies suggest that ^{161}Tb-PSMA may be particularly effective in heterogeneous or micrometastatic disease, although current macrodosimetry approaches may underestimate its true biologic impact (7). Given the evolving metastatic landscape between treatment cycles, lesion-specific absorbed doses were not directly compared.

From a clinical perspective, biochemical response after ^{161}Tb-PSMA therapy was limited. Serum PSA increased

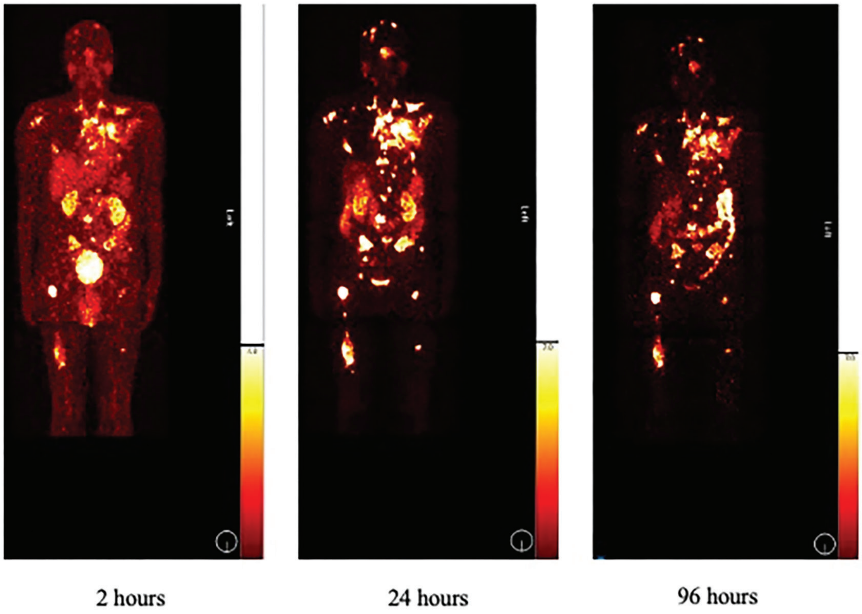

Figure 1. Quantitative SPECT/CT imaging maximum intensity projection at 2 hours (left), 24 hours (middle), and 96 hours (right) post-administration of ^{161}Tb-PSMA

^{161}Tb-PSMA: Terbium-161-prostate-specific membrane antigen, SPECT/CT: Single photon emission computed tomography/computed tomography

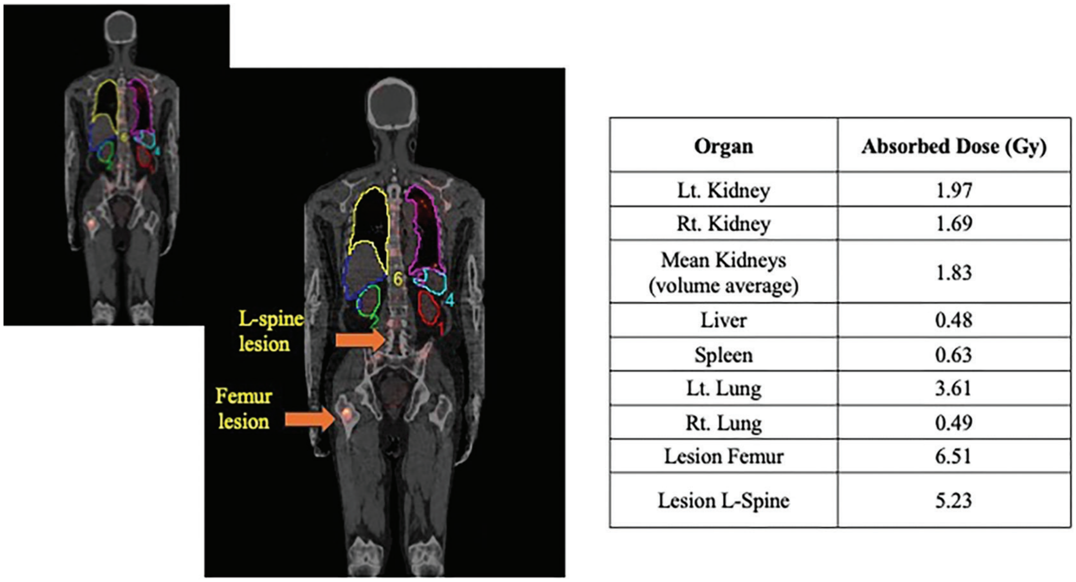

Organ	Absorbed Dose (Gy)
Lt. Kidney	1.97
Rt. Kidney	1.69
Mean Kidneys (volume average)	1.83
Liver	0.48
Spleen	0.63
Lt. Lung	3.61
Rt. Lung	0.49
Lesion Femur	6.51
Lesion L-Spine	5.23

Figure 2. (Left) Coronal fused SPECT/CT image at 24 hours post-treatment showing AI-assisted organ segmentation used for voxel-based dosimetry analysis. Organs segmented include the left lung (yellow), right lung (pink), left kidney (green), right kidney (cyan), spleen (red), and liver (blue). Selected skeletal metastases, including a lumbar spine lesion and a left femoral lesion, are annotated. (right) Absorbed dose to organs at risk and lesion from ^{161}Tb-PSMA

SPECT/CT: Single photon emission computed tomography/computed tomography, ^{161}Tb-PSMA: Terbium-161-prostate-specific membrane antigen

Table 1. Intra-patient of renal dosimetry between the 12th treatment cycle with ^{177}Lu-PSMA in March 2024 and the 14th cycle with ^{161}Tb-PSMA in February 2025

	^{177}Lu-PSMA	**^{161}Tb-PSMA**
Treatment cycle	12th	14th
Time	Mar 2024	Feb 2025
Treatment activity (MBq)	8103 (219 mCi)	6283 (170 mCi)
Dosimetry software and method	Hermes 3.1 singlet time-point dosimetry at 48 h (hanscheid method)	Hermes 3.1 multiple time-point dosimetry
Mean kidneys (Gy)	1.84	1.83
Mean kidneys per administered activity (mGy/MBq)	0.22	0.29

^{177}Lu-PSMA: Lutetium-177-prostate-specific membrane antigen, ^{161}Tb-PSMA: Terbium-161-prostate-specific membrane antigen

from 918 ng/mL prior to treatment to 978 ng/mL at early post-therapy assessment, consistent with advanced disease burden and possible delayed or absent biochemical response in this heavily pretreated setting. In contrast, a marked symptomatic improvement was observed. The patient's pain, previously rated as 5 out of 10 at the right thigh, improved substantially after ^{161}Tb-PSMA therapy, with a post-treatment pain score of 0-1 out of 10, allowing discontinuation of tramadol and NSAID analgesics.

Regarding treatment-related toxicity, ^{161}Tb-PSMA was generally well tolerated. The patient experienced transient fatigue and malaise during the first week after therapy, which resolved spontaneously. Xerostomia was not newly observed and was attributed to cumulative prior ^{177}Lu-PSMA treatments, for which the patient continued to use artificial saliva.

Laboratory monitoring demonstrated stable renal function and hematologic parameters following ^{161}Tb-PSMA administration. Serum creatinine showed a mild increase from 1.25 mg/dL before therapy to 1.31 mg/dL after therapy, without clinical evidence of nephrotoxicity. Hematologic indices remained stable, with haematocrit changing from 29.0% to 28.9% and platelet count decreasing from 185000/µL to 159000/µL, without clinically significant cytopenia. These findings are consistent with previously reported safety profiles of ^{161}Tb-PSMA therapy (7).

Conclusion

This case represents the first reported clinical application of ^{161}Tb-PSMA therapy in Thailand and Southeast Asia. Quantitative SPECT/CT-based voxel dosimetry demonstrated effective lesion targeting and favourable absorbed dose distribution, with acceptable radiation exposure to normal organs. A comparative intra-patient analysis revealed that the renal absorbed dose per administered activity was slightly higher for ^{161}Tb-PSMA than for ^{177}Lu-PSMA, likely reflecting differences in diseases burden and biodistribution. Although an early biochemical response was not observed, ^{161}Tb-PSMA therapy resulted in marked symptomatic improvement with substantial pain relief and reduced analgesic requirements, while maintaining a favourable safety profile without clinically significant renal or hematologic toxicity. These findings support the role of quantitative imaging, dosimetry and suggest that ^{161}Tb-PSMA may offer a safe and clinically meaningful palliative option in heavily pretreated patients with mCRPC after ^{177}Lu-PSMA therapy.

Ethics

Informed Consent: Written informed consent was obtained from the patient for the publication of this short communication and any accompanying images. All identifiable information has been anonymised to protect the patient's privacy.

Acknowledgement

The authors would like to thank GE Healthcare for their technical support in the single photon emission computed tomography calibration and system configuration process. We also acknowledge Hermes Medical Solutions for providing access to the dosimetry software used for voxel-based absorbed dose calculations.

Footnotes

Authorship Contributions

Surgical and Medical Practices: T.A., B.K., W.C., K.C., Concept: T.A., K.C., Design: K.C., Data Collection or Processing: S.A., P.C., P.P., T.T., B.K., W.C., Analysis or Interpretation: S.A., W.C., K.C., Literature Search: K.K., W.C., K.C., Writing: K.C.

Conflict of Interest: No conflicts of interest were declared by the authors.

Financial Disclosure: The authors declare that this study has received no financial support.

Availability of Data and Material

The datasets generated and analysed during the current study are available from the corresponding author upon reasonable request.

References

1. Schaefer-Schuler A, Burgard C, Blickle A, Maus S, Petrescu C, Petto S, Bartholomä M, Stemler T, Ezziddin S, Rosar F. [^{161}Tb]Tb-PSMA-617 radioligand therapy in patients with mCRPC: preliminary dosimetry results and intra-individual head-to-head comparison to [^{177}Lu]Lu-PSMA-617. Theranostics. 2024;14:1829-1840.
2. Buteau JP, Kostos L, Alipour R, Jackson P, McInstosh L, Emmerson B, Haskali MB, Xie J, Medhurst E, Ravi R, Gonzalez BD, Fettke H, Blyth B, Furic L, Owen K, Sandhu S, Murphy DG, Azad AA, Hofman MS. Clinical trial protocol for VIOLET: a single-center, phase I/II trial evaluation of radioligand treatment in patients with metastatic castration-resistant prostate cancer with [^{161}Tb]Tb-PSMA-I&T. J Nucl Med. 202;65:1231-1238.
3. Song H, Sgouros G. Alpha and beta radiation for theragnostics. PET Clin. 2024;19:307-323.
4. Al-Ibraheem A, Doudeen RM, Juaidi D, Abufara A, Maus S. ^{161}Tb-PSMA radioligand therapy: first-in-humans SPECT/CT Imaging. J Nucl Med. 2023;64:1322-1323.
5. Al-Ibraheem A, Abdlkadir AS, Sweedat DA, Maus S, Al-Rasheed U, Salah S, Khriesh F, Juaidi D, Abu Dayek D, Istatieh F, Anwar F, Asrawi A, Abufara A, Al-Rwashdeh M, Abu-Hijlih R, Sharaf B, Ghanem R, Abdel-Razeq H, Mansour A. From despair to hope: first Arabic experience of ^{177}Lu-PSMA and ^{161}Tb-PSMA therapy for metastatic castration-resistant prostate cancer. Cancers (Basel). 2024;16:1974.
6. Sezgin C, Uygur E, Parlak Y, Karatay B, Barutca S, Dirican A, et al. Terbium-161 PSMA therapy in mCRPC patient based on an optimized radiolabeling protocol. Journal of Radioanalytical and Nuclear Chemistry. 2025;334:5979.
7. Küçük NÖ, Coşkun N, Araz M, Alan Selcuk N, Berberoglu K, Ozdemir EC, Gümüşer FG, Kuyumcu S, Sezgin C, Sanli O, Sanli Y, Sendur MAN, Urun Y. Initial multicenter experience with [161Tb]Tb-PSMA in [^{177}Lu]Lu-PSMA-refractory metastatic castration-resistant prostate cancer: preliminary results. Nucl Med Semin. 2025;12:1921-1926.

Erratum

Mol Imaging Radionucl Ther 2026;35(1):84 **DOI:***10.4274/mirt.galenos.2026.e001*

DOI:10.4274/mirt.galenos.2025.78700

Karanjia R, Kumar Sarkar P, Bashir H, S Kommu SS. The PSMA-PET conundrum: a survey of UK prostate cancer surgeons and their use of PSMA-PET prior to radical prostatectomy. Mol Imaging Radionucl Ther. 2025;34:188-193.

The mistake was made inadvertently during the evaluation process.

In the Abstract section, under the heading Objectives, the country was incorrectly written as United States (UK).
This has been corrected to United Kingdom (UK).

In the Introduction section, United States (UK) was written incorrectly.
In the Introduction section correct country name is the United Kingdom (UK).